

PSFC/RR-11-11

**Ion Collection by a Conducting Sphere in a
Magnetized or Drifting Collisional Plasma**

Haakonsen, C.B.

October 2011

**Plasma Science and Fusion Center
Massachusetts Institute of Technology
Cambridge MA 02139 USA**

This research was supported in part by NSF/DOE Grant No. DE-FG02-06ER54512, and in part by an award from the Department of Energy (DOE) Office of Science Graduate Fellowship Program (DOE SCGF). The DOE SCGF Program was made possible in part by the American Recovery and Reinvestment Act of 2009, administered by ORISE-ORAU under contract no. DE-AC05-06OR23100. Reproduction, translation, publication, use and disposal, in whole or in part, by or for the United States government is permitted.

— this page left intentionally blank —

Ion Collection by a Conducting Sphere in a Magnetized or Drifting Collisional Plasma

by

Christian Bernt Haakonsen

B.Sc., McGill University (2007)

M.Sc., McGill University (2009)

Submitted to the Department of Nuclear Science and Engineering
in partial fulfillment of the requirements for the degree of

Master of Science in Nuclear Science and Engineering

at the

MASSACHUSETTS INSTITUTE OF TECHNOLOGY

September 2011

© 2011 Christian Bernt Haakonsen. All rights reserved.

The author hereby grants to MIT permission to reproduce and to distribute publicly paper and electronic copies of
this thesis document in whole or in part in any medium now known or hereafter created.

Signature of Author

Department of Nuclear Science and Engineering
August 25, 2011

Certified by

Ian H. Hutchinson
Professor of Nuclear Science and Engineering
Thesis Supervisor

Certified by

Jeffrey P. Freidberg
Emeritus Professor of Nuclear Science and Engineering
Thesis Reader

Accepted by

Mujid S. Kazimi
TEPCO Professor of Nuclear Engineering
Chair, Department Committee on Graduate Students

Ion Collection by a Conducting Sphere in a Magnetized or Drifting Collisional Plasma

by

Christian Bernt Haakonsen

Submitted to the Department of Nuclear Science and Engineering
on August 25, 2011, in partial fulfillment of the
requirements for the degree of
Master of Science in Nuclear Science and Engineering

Abstract

Ion collection by dust grains and probes in plasmas with a neutral background is of interest in the study of both space and terrestrial plasmas, where charge-exchange collisions can play an important role in ion collection. Further, background drifts or magnetic fields can significantly affect the ion collection by and the potential structure near such objects, and should therefore also be included. These effects, however, are difficult to include in a theoretical treatment, and thus this problem lends itself to a computational approach.

To be able to tackle problems with a neutral background, the 3D3v hybrid particle-in-cell code SCEPTIC3D has been upgraded to include charge-exchange collisions. This required the development of a new Monte Carlo based reinjection scheme. The new reinjection scheme and other upgrades are described in detail, and the collisionless operation of the reinjection scheme is validated against the old SCEPTIC3D reinjection scheme, while its collisional operation is validated through comparisons with the reinjection scheme in SCEPTIC (2D). The new reinjection scheme can easily be modified to allow the injection of an almost arbitrary distribution function at the domain boundary, enabling future studies of the sensitivity of ion collection to the injected velocity distribution.

Studies of ion collection in magnetized or drifting plasmas using the upgraded code extend earlier stationary, unmagnetized results, which showed an enhancement of ion current at intermediate collisionality. It is found that this enhancement is gradually suppressed with increasing background neutral drift speed, and is entirely absent for speeds above the ion sound speed. Adding a magnetic field rather than a neutral drift appears to in fact increase the collisional ion current enhancement.

Thesis Supervisor: Ian H. Hutchinson
Title: Professor of Nuclear Science and Engineering

Thesis Reader: Jeffrey P. Freidberg
Title: Emeritus Professor of Nuclear Science and Engineering

Acknowledgments

First and foremost, I would like to acknowledge and thank my advisor Pr. Ian Hutchinson for his guidance and support through my first two years at MIT. He is always welcoming and available for an impromptu meeting, and his keen physical insight has made for countless interesting scientific discussions over the past two years. His comments and input on this thesis have been greatly appreciated, as has his patience and understanding when external circumstances slowed its progress. Working with Ian I have benefited from a large degree of freedom in choosing research directions and how to spend my time, which has allowed me to pursue numerous other projects and classes not directly related to my thesis research, but that are to the benefit of my education and development as a scientist. I look forward to continuing work towards my PhD with Ian over the next few years.

I would also like to thank Pr. Jeffrey Freidberg, who agreed to be my thesis reader on quite short notice and despite his recent retirement from academic duties. Jeff's textbook and classes have played an important role in my plasma physics education, and his comments contributed to improving this thesis. I am grateful for his time and effort, and for the interesting discussions we have had over the past two years.

The computer simulations using SCEPTIC3D were carried out on the MIT PSFC parallel AMD Opteron/Infiniband cluster Loki. I am grateful to Dr. John Wright and Dr. Darin Ernst for granting me access to Loki, and for providing valuable assistance in troubleshooting issues on Loki when they arose.

This research was supported in part by NSF/DOE Grant No. DE-FG02-06ER54512, in part by tuition support from the Norwegian State Educational Loan Fund, and in part by an award from the Department of Energy (DOE) Office of Science Graduate Fellowship Program (DOE SCGF). The DOE SCGF Program was made possible in part by the American Recovery and Reinvestment Act of 2009, administered by ORISE-ORAU under contract no. DE-AC05-06OR23100.

Contents

1	Introduction	13
1.1	Basic Problem	14
1.1.1	Orbital Motion Limited Theory	15
1.1.2	Allen–Boyd–Reynolds Theory	16
1.2	Applications	16
1.2.1	Dust Grains	17
1.2.2	Langmuir Probes	17
1.2.3	Moon and Spacecraft	18
1.3	SCEPTIC3D	18
1.3.1	Particle-In-Cell Method	18
1.3.2	Unit System	19
1.3.3	Coordinates	19
1.4	Outline	19
2	Charge-Exchange Collisions in SCEPTIC3D	23
2.1	Unperturbed Plasma Model	23
2.1.1	Charge-Exchange Collisions	24
2.1.2	External Fields	26
2.1.3	Neutral Drift	28
2.1.4	Overall Ion Drift	29
2.2	Monte Carlo Rejection Scheme	32
2.2.1	Generating the Unperturbed Distribution Function	32
2.2.2	Determining the Rejection Location	35

2.3	Validating the New Rejection Scheme	36
2.3.1	Collisionless Validation Against SCEPTIC3D	37
2.3.2	Collisional Validation Against SCEPTIC	52
3	Upgrades to SCEPTIC3D	59
3.1	Distribution Function Diagnostic	59
3.1.1	VINETA-Relevant Velocity Distributions	60
3.1.2	VINETA-Relevant Distribution Moments	61
3.2	Modifications to the Poisson Solver	65
3.2.1	Finite Volume Matrix	68
3.2.2	Asymmetry of the Finite Volume Matrix	71
3.2.3	Biconjugate Gradient Method	73
3.2.4	Parallel Version of the Poisson Solver	75
3.2.5	Verification of the Upgraded Solver	76
3.2.6	Nonlinear Solution to the Poisson Equation	82
3.3	HDF5 Output	83
4	Collisional Ion Collection by a Conducting Sphere	87
4.1	Perturbation by a Collecting Object	87
4.1.1	Collecting Object	87
4.1.2	Boltzmann Relation	89
4.1.3	External Electric Field	90
4.2	Ion Collection with a Background Neutral Drift	94
4.3	Ion Collection with a Background Magnetic Field	98
5	Discussion and Conclusions	103
5.1	New Capabilities of SCEPTIC3D	103
5.2	Collisional Ion Collection	104
5.3	Future Work	105

List of Figures

1-1	SCEPTIC3D coordinate system	20
1-2	SCEPTIC3D mesh	21
2-1	Collisionless injection: 3D velocities	40
2-2	Collisionless injection: distribution in v_x	41
2-3	Collisionless injection: distribution in v_y	42
2-4	Collisionless injection: distribution in v_z	43
2-5	Collisionless injection: distribution in v_r	45
2-6	Collisionless injection: 3D locations	47
2-7	Collisionless injection: distribution in x	48
2-8	Collisionless injection: distribution in y	49
2-9	Collisionless injection: distribution in z	50
2-10	Collisional injection: distribution in v_z for parallel ion drift	54
2-11	Collisional injection: distribution in v_z for parallel neutral drift	55
2-12	Collisional injection: distribution in v_z for parallel ion and neutral drift	56
3-1	v_y distribution at locations offset along y -axis	62
3-2	v_y distribution at locations offset along z -axis	63
3-3	v_y distribution at locations offset along x -axis	64
3-4	Temperature and average drift in \mathbf{e}_y direction	66
3-5	Temperature and average drift	67
3-6	Structure of the matrix \mathbf{A}	78
3-7	Solution to $\mathbf{A}\phi = \mathbf{y}$ from upgraded solver	80
3-8	Solution to $\mathbf{A}\phi = \mathbf{y}$ from old solver	81

4-1	Ion density near object for background neutral drifts	95
4-2	Ion collection against collisionality and neutral drift	96
4-3	Ion density for background magnetic fields	99
4-4	Ion collection against collisionality and magnetic field strength	100

List of Tables

2.1	Summary of collisionless injection validation	38
2.2	Summary of collisional injection validation	53

Chapter 1

Introduction

There are countless settings in which objects interact with a plasma, ranging from dust grains in space and laboratory or industrial plasmas, Langmuir and Mach probes used to diagnose plasma experiments, and spacecraft, to objects like the moon. In many of these cases the plasma is flowing, and there may be a background magnetic field. Further, there may be a significant neutral population with which the ions undergo charge-exchange collisions, so there is a wide range of conditions under which one may need to understand the interaction of objects with a plasma.

If an isolated object is introduced into a plasma, it will charge until it reaches some equilibrium potential (typically negative) for which the electron and ion currents to the object balance. The equilibrium potential and electron and ion currents affect the dynamics of dust-grains, for instance in tokamak edge plasmas, and one can also use the floating potential of probes to infer some properties of a plasma. This can be extended to flux-sensing (electric) probes, which measure the dependence of the collected current on the bias voltage (Langmuir probes). However, relating the current–voltage curves to plasma properties is a difficult problem because the conducting surface acts as a boundary to the plasma, thereby strongly perturbing it locally. More sophisticated flux-sensing probes aimed at measuring plasma flow (Mach probes) can be even more challenging to interpret, so advancing the understanding of current collection by electric probes is important in verifying and improving the interpretation of such probes (which are ubiquitous in plasma experiments).

A background plasma drift, magnetic field, and/or collisions with background neutrals greatly complicates any theoretical model of ion collection, so models are typically restricted to specific limits. Experiments can investigate the ion collection in specific settings, but to explore the parameter space to develop a quantitative understanding of the impact of collisions, flow, and magnetic fields, simulations are needed. The focus of this thesis is on extending the capabilities of the SCEPTIC3D¹ code [1, 2, 3], such that it in the future can be used to run simulations aimed at developing such a quantitative understanding, and at bridging the gaps between the various limits that can be studied theoretically.

1.1 Basic Problem

The basic problem considered is that of a spherical absorbing object perturbing a plasma. In particular, the ion collection by the object and potential structure near it is of interest, as well as the forces on the object for some applications. The large range of physical systems in which an object interacts with a plasma introduces dependencies on a number of parameters characterizing the system, all of which can have wildly different values for different problems.

Of paramount importance in determining the perturbation to the plasma by the object is the ratio of the electron Debye length to the object radius: λ_{De}/r_p . If this ratio is large, the object will introduce a Coulomb-like potential perturbation; if it is small, the plasma will shield the perturbation, and thus limit the size of the perturbed region. Note that the actual size of the object is of little importance, so the same simulation could in principle apply to problems on vastly different physical scales.

The details of ion collection are mostly of interest for strongly electron-repelling objects, i.e. ones with object potentials $V_p < -T_e/e$, where the electron temperature T_e is in units of energy. Thus, another important parameter is the ion to electron temperature ratio: T_i/T_e , since the random velocities of the ions will greatly affect their orbits around the object, and thus their probability of collection and the ion

¹Specialized Coordinate Electrostatic Particle and Thermals in Cell 3D (SCEPTIC3D)

density near the object.

A number of other parameters can affect ion collection, like charge-exchange collisionality, background ion drift, and magnetic field strength, but discussion of the effects of those parameters is deferred to chapters 2 and 4.

1.1.1 Orbital Motion Limited Theory

Orbital motion limited (OML) theory treats ion collection for spherically (and cylindrically) symmetric problems where $\lambda_{De} > r_p$, and traces back to work by Mott-Smith and Langmuir [4]. The discussion in this section also draws on later work by Allen, Boyd, and Reynolds [5] and Allen [6].

The basis of OML theory is conservation of the energy and angular momentum of ions along their orbits. This allows one to relate the impact parameter h of an ion to the corresponding distance of closest approach r_h , through the potential V_h at r_h and the initial ion energy $q_i V_0$ (for ion charge q_i):

$$h = r_h \left(1 - \frac{V_h}{V_0}\right)^{\frac{1}{2}}. \quad (1.1)$$

For ions of a fixed energy, those with an impact parameter corresponding to a distance of closest approach that is smaller than the object radius r_p will be collected. The collected ion current is thus

$$I_i = 4\pi r_p^2 I_{iR} \left(1 - \frac{V_p}{V_0}\right), \quad (1.2)$$

where I_{iR} is the positive ion current per unit area in the unperturbed plasma, and V_p is the object potential. Averaging over a Maxwellian distribution of initial ion velocities gives the same result, but using a drifting Maxwellian gives a more complicated expression [7].

A requirement for the OML method to apply is that

$$\frac{V}{V_p} > \left(\frac{r_p}{r}\right)^2 \quad (1.3)$$

for all r , which is the condition for there not to be an absorption radius outside the object. This condition is satisfied for a Coulomb potential, so as mentioned OML tends to be valid for cases where $\lambda_{De} > r_p$.

If there is an absorption radius outside the object, that distance would have to be used in the calculation of the current, and its location and potential would need to be known to apply OML. That problem was tackled by Bohm, Burhop, and Massey [8], relying on a method by Tonks and Langmuir [9] for calculating the potential distribution in the plasma.

1.1.2 Allen–Boyd–Reynolds Theory

In sharp contrast to OML, Allen–Boyd–Reynolds (ABR) theory [5] considers ions with purely radial velocities, which are dominated by the change in potential from the unperturbed plasma. This effectively neglects the initial random ion velocity, i.e. assumes cold ions. Further, the electrons are assumed to be Maxwellian, such that they satisfy a Boltzmann relation (see sec. 4.1.2) in the perturbed potential. The resulting expression for the ion current to the object is

$$I_i = 4\pi r_s^2 n_{i\infty} q_i \sqrt{\frac{T_e}{m_i}} \exp\left(-\frac{1}{2}\right), \quad (1.4)$$

where r_s is the sheath radius ($= r_p$ if the sheath thickness is neglected), m_i is the ion mass, and $n_{i\infty}$ is the ion density at infinity. Note that the ion current in this case depends on the electron temperature, not the ion temperature as in OML.

1.2 Applications

There are many situations where objects interact with plasmas, and this section gives some examples of where calculations of ion collection may be relevant.

1.2.1 Dust Grains

Dust grains are found in a variety of plasmas, ranging from industrial plasmas and dedicated dusty plasma experiments [10] to tokamak edge plasmas [11] and planetary disks [12]. The grains have a floating potential, may or may not be conducting, and are typically smaller than the electron Debye length.

Dusty plasma experiments tend to have have much higher neutral density than ion density, making charge-exchange collisions important in setting the floating potential of and forces on the dust grains. In earth-based experiments, gravity drives the dust particles to the sheath entrance, where the gravitational force is balanced by the electric field in the sheath. Thus, to tackle problems relating to dusty plasma experiments SCEPTIC3D needs to include charge exchange collisions and an electric field, and in some cases also a magnetic field.

In tokamak edge plasmas charge-exchange collisions are unlikely to be important for dust grains, but there could be regions of very tenuous plasma behind divertor plates etc. where charge-exchange collisions cannot be neglected. There, the magnetic field must also likely be included, offering another possible application for studies of dust grains in magnetized collisional plasmas.

1.2.2 Langmuir Probes

Interpreting Langmuir and other electric probes has been a driving force behind studies of ion collection by objects for almost a century, but new computational and experimental capabilities are still opening up new interesting areas of study. For example, laser-induced-fluorescence measurements at the VINETA experiment [13] will allow measurement of the ion distribution function near a spherical object. This enables detailed code–experiment comparisons, which may further advance the understanding of Langmuir probes and the interactions of objects with plasmas in general.

1.2.3 Moon and Spacecraft

The solar wind provides a plasma environment for objects in space, including spacecraft and even the moon. Recently there have been both observations and accompanying simulations of the solar wind in the vicinity of the moon [14, 15], highlighting the interest in the magnetized plasma wake formed by the moon in the solar wind.

1.3 SCEPTIC3D

The SCEPTIC3D code is a 3D upgrade to the 2D code SCEPTIC [16, 17, 18]. It calculates self-consistent steady-state solutions to the Poisson–Vlasov equations, under the assumption of Boltzmann electrons. The code has been described in detail by Patacchini [19], but a brief description is given here for convenience.

1.3.1 Particle-In-Cell Method

The canonical works on the particle-in-cell (PIC) method are by Birdsall and Langdon [20] and Hockney and Eastwood [21], but there is also a nice review by Verboncoeur [22]. The basic principle of the method is to statistically represent the ion and electron distribution functions with computational particles, while storing the electric and magnetic fields on a grid, and then to alternate between updating the particle positions and the solution for the fields while taking time-steps to evolve the distribution functions from some initial guess at the solution. In the electrostatic approximation the currents due to the particles are ignored, so only the Poisson equation needs to be solved to update the fields on the grid.

PIC simulations make few physical assumptions, but are computationally demanding. In particular, the small mass of electrons compared to ions means that very fine time steps must be taken to accurately capture the motion of electrons. Therefore, many time-steps are required to achieve convergence of the ion distribution to a steady-state solution, which is the aim for the problems tackled with SCEPTIC3D. One way to reduce the computational cost is to not treat electrons using the PIC

method, but to rather assume that they satisfy a Boltzmann relation. This allows a time-step appropriate to the ion motion to be used, thereby greatly reducing the computation time required. A discussion of the validity of the Boltzmann electron assumption is given in sec. 4.1.2.

1.3.2 Unit System

The units used for quantities in SCEPTIC3D carried over from SCEPTIC, and are described by Patacchini [7]. Four fundamental units are used: Mass is in units of $M = m_i/Z$, where m_i is the ion mass and Z its charge state; charge is in units of e , the elementary charge; distance is in units of the radius r_p of the spherical object; and energy is in units of T_e , the electron temperature (which includes the Boltzmann constant k_B).

From these fundamental units, the other relevant units can be derived. In particular, speed is measured in units of ion sound speed $c_s = \sqrt{T_e/M}$, time in sound-crossing times r_p/c_s , potential in units of T_e/e , and magnetic fields as cyclotron frequency in units of inverse time.

1.3.3 Coordinates

SCEPTIC3D is a 3D3v PIC code, so each computational particle has a three-dimensional position and a three-dimensional velocity. The three spatial dimensions hold a spherical mesh, which has grid-points spaced evenly in r between r_p and the outer domain size r_b , spaced evenly in $\cos(\theta)$ for the inclination angle, and spaced evenly in the azimuthal angle ψ . The coordinates are illustrated in fig. 1-1, and the grid in fig. 1-2.

1.4 Outline

In addition to this introductory chapter, the thesis has four other chapters:

- Chapter 2 describes the model background plasma and the implementation of charge-exchange collisions in SCEPTIC3D, and covers the new Monte Carlo

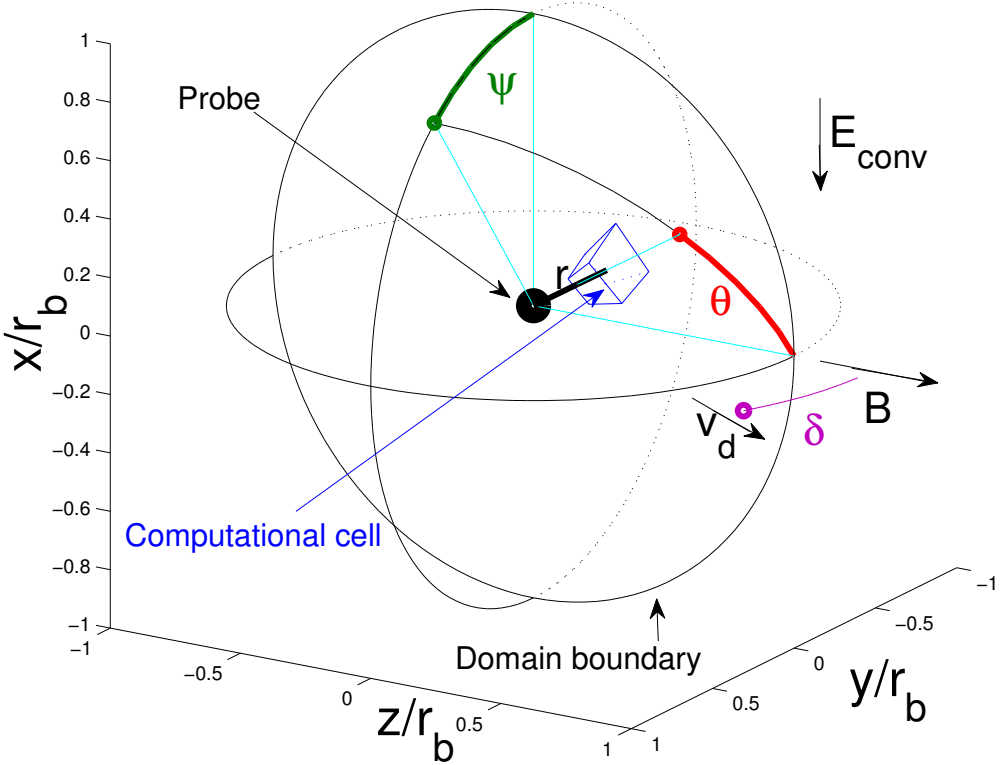


Figure 1-1: SCEPTIC3D coordinate system, reproduced from [19]. The spherical object is labeled ‘probe’, and the convective electric field \mathbf{E}_{conv} , ion drift \mathbf{v}_d , and magnetic field \mathbf{B} are illustrative only, since the upgraded SCEPTIC3D also allows for neutral drift and a parallel electric field. Further, the magnetic field can be set in any direction in the $y-z$ plane.

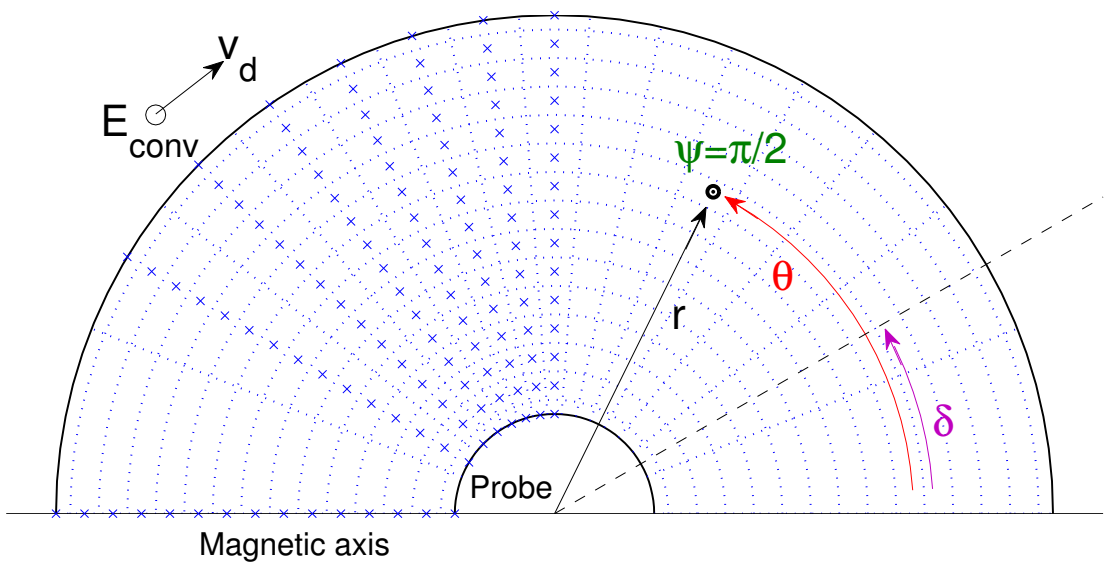


Figure 1-2: SCEPTIC3D mesh in the $\psi = \pi/2$ half-plane, reproduced from [19]. Again the ‘magnetic axis’, convective electric field, and ion drifts are illustrative only, since this specific setup is only one possibility in the upgraded SCEPTIC3D.

based reinjection scheme and its validation in some detail.

- Chapter 3 describes various other upgrades made to SCEPTIC3D in the past two years, which include a new binary output system based on HDF5, a new distribution function diagnostic, and an upgraded Poisson solver.
- Chapter 4 introduces the first results obtained using the newly upgraded SCEPTIC3D, examining the ion density near and ion collection by conducting spherical objects at floating potential in the presence of a background magnetic field or neutral drift.
- Chapter 5 offers some concluding remarks and thoughts on future work, marking the end of the thesis.

Chapter 2

Charge-Exchange Collisions in SCEPTIC3D

2.1 Unperturbed Plasma Model

The unperturbed system is taken to be a single-element monatomic gas of neutral atoms, and a neutral plasma consisting of electrons and singly ionized ions of that element. The gas and plasma occupy the same space, and both are homogeneous (translation invariant).

There are six types of binary collisions possible between the three particle species: Neutral–neutral, neutral–ion, neutral–electron, ion–ion, ion–electron, and electron–electron collisions. Each collision type has associated time scales for momentum and energy transfer between and among species, as well as characteristic length scales (i.e. mean free paths). Thus, a system that is started away from equilibrium will go through a series of equilibration stages, starting with the quantity associated with the shortest time-scale. While in any of these equilibration stages (or if driven in a way that emulates one of them), the system can be considered quasi-steady on time scales much shorter than the relevant equilibration time-scale.

The neutral gas is taken to have a (drifting) Maxwellian distribution function, assumed to be unaffected by the ions and electrons. Thus, either the time-scale considered is much shorter than that required for collisions with ions and electrons

to perturb the distribution function, or neutral–neutral collisions are fast enough to thermalize the neutrals before their distribution can be significantly perturbed.

The dominant type of neutral–ion collisions is typically charge-exchange collisions, which will be discussed in greater detail in sec. 2.1.1. Though the effect of these collisions on the neutral distribution function is considered to be negligible, the same is not necessarily true for the ions. If there is a non-negligible probability that any given ion undergoes a charge-exchange collision on the time-scale considered, the ion distribution function will be perturbed by the neutral distribution, unless Coulomb collisions are fast enough to thermalize the ions. However, ion–ion and ion–electron collisions are neglected in the PIC treatment, so only problems where they are unimportant for the ions can be considered.

The electrons are lighter and faster than the ions and neutrals, so drifts that are significant for the other species can typically be neglected for the electrons (with the exception of parallel electric field driven drifts, as discussed in sec. 2.1.4). The electron distribution function can thus remain approximately Maxwellian despite having its drift coupled to the ions or neutrals through (momentum transfer) collisions, and even if electron–electron collisions are not especially effective at thermalizing the distribution. However, to maintain a different electron temperature the time-scale for energy transfer to and from electrons must be long. An approximately Maxwellian distribution function is required for the Boltzmann treatment of the electrons, and the applicability of this assumption is discussed further in sec. 4.1.2.

2.1.1 Charge-Exchange Collisions

The details of collision cross-sections for ions with neutrals are complicated, and depend on the atomic element, relative velocity, type of collision, and the relevant quantity of interest (e.g. momentum). An overview for the case of argon is given in ref. [23], but covers a much larger energy-range than is typically relevant for SCEP-TIC3D.

At low energies ($< 0.01 \text{ eV}$), the largest contribution to the collision cross-section of an ion with a neutral is typically that due to the polarization interaction [23, 24],

where the ion polarizes the neutral to give an attractive force between them. Such an interaction amounts to an elastic collision of the ion with the neutral, and if the distance of closest approach is small enough an electron can be transferred from the neutral to the ion. The cross-section for the polarization interaction scales inversely with the relative velocity [25], giving a velocity-independent collision frequency for the ions.

For ions and neutrals of the same element, quantum-mechanical resonances greatly enhance the range over which an electron can be transferred from the neutral to the ion. The cross-section for these resonant charge-exchange collisions decreases weakly with energy (slower than $1/v$) [23, 24], and they are the dominant contribution to the momentum cross-section in the range 0.1 eV–100 eV. In that energy range, a charge-exchange collision effectively swaps the identity (velocity) of the atom and the ion, and the charge-exchange cross-section of argon (e.g.) is $\sim 5 \times 10^{-19} \text{ m}^2$.

At high energies, charge-exchange cross-sections can be measured accurately with beam experiments, but at low energies this is not feasible. Rather, one relies on models of the underlying physical processes, and then infers what the low-energy cross-sections are from ion diffusion and mobility experiments [24]. The cross-sections depend on the specific element considered, and their energy dependence is only as good as the underlying model used.

As an approximation to the full charge-exchange cross-section, charge-exchange collisions in SCEPTIC3D are taken to occur with constant frequency for ions of any velocity, and a new ion velocity is drawn randomly from the neutral population after each collision. This approach has also been used previously [26, 27, 28, 29, 30], and is intended to capture the main effects of charge-exchange collisions without using accurate cross-sections specific to a particular application. The collision cross-sections used in SCEPTIC3D thus don't quite have the right energy-dependence, but since typically a relatively narrow range of ion energies are important in a given application, the variation of the cross-section over that range may not be very important.

One reason for using a constant collision frequency is the relative ease with which such collisions can be implemented in SCEPTIC3D, since the time until the next

collision for each ion can be calculated according to Poisson statistics, without regard to the ion velocity. Further, drawing a random velocity from the neutral distribution is easier computationally than making a biased draw based on the velocity of each ion.

The constant collision frequency assumption for ions corresponds to a collision cross-section that scales inversely with the magnitude of the relative velocity between the ion and the atom. For this velocity dependence the change in cross-section is balanced by an increased number of encounters, resulting in a constant collision frequency and unbiased draw from the neutral population. The treatment of collisions in SCEPTIC3D is thus self-consistent, though it may not accurately model a specific physical system.

2.1.2 External Fields

An externally imposed electric or magnetic field (\mathbf{E} or \mathbf{B} , respectively) breaks the isotropy of the system, and introduces a Lorentz force

$$\mathbf{F}_L = q(\mathbf{E} + \mathbf{v} \times \mathbf{B}) \quad (2.1)$$

on the electrons and ions (for charge q and velocity \mathbf{v}). In the case of a uniform magnetic field the motion of the electrons and ions perpendicular to the field is restricted, giving rise to gyro-motion in the unperturbed system.

Perpendicular Electric Field

In the absence of collisions, a uniform background electric field perpendicular to the magnetic field leads to $\mathbf{E} \times \mathbf{B}$ drift of the electron and ion guiding centers. The drift velocity is

$$\mathbf{v}_{E\perp} = \frac{\mathbf{E} \times \mathbf{B}}{B^2}, \quad (2.2)$$

which is perpendicular to both the electric and magnetic fields. The perpendicular electric field can be absorbed by a transformation to the drifting frame, where the

electrons and ions can be treated as if there was only a magnetic field. However, in this frame the neutrals have an additional drift compared to in the stationary frame (equal and opposite to \mathbf{v}_E), which must be considered if charge-exchange collisions cannot be neglected.

In the presence of charge-exchange collisions, a perpendicular electric field will drive a net current due to the different drag on the ions and electrons. However, since the $\mathbf{E} \times \mathbf{B}$ drift speeds considered typically are much smaller than the electron thermal speed, it is expected that the modification to the electron distribution function due to a perpendicular electric field will be negligible, and that the resulting current will be small enough to be consistent with the electrostatic approximation.

Parallel Electric Field

A uniform electric field parallel to (or in the absence of) a magnetic field will effect a constant acceleration of the ions and electrons. In a steady-state system without net particle acceleration, the electric force on each species must on average be balanced by the various drags on the particles, and there will be a current flowing in the direction of the parallel electric field.

Since ion–ion collisions and ion–electron collisions are neglected in SCEPTIC3D, the charge-exchange collisions with neutrals alone provide the drag to balance the parallel electric field in the case of ions. Further, because the post-collision ion velocity is uncorrelated with the pre-collision velocity (as a result of the constant collision frequency assumption), there is no transfer of momentum from the parallel to the perpendicular direction. Thus, the acceleration in the parallel direction does not affect the perpendicular ion velocities.

For electrons, which of the collision types contribute significantly to the drag will depend on the application. The electrons are much lighter than the ions, so electron–ion collisions may be important, and both they and electron–neutral collisions may allow the parallel acceleration to affect the perpendicular electron velocity distribution. The balance between the electric field and the collisional drags will determine the overall drift, but the actual modification to the distribution function (long tail or

small bulk shift) will depend on the specifics of the two mentioned collision types, as well as the electron–electron collisions.

Since the drag on the electrons is not known in general, the form of the electron distribution function could vary greatly from problem to problem. In particular, there could be a large electron current due to a parallel electric field, possibly with a large fraction of super-thermal (or even run-away) electrons. Such super-thermal electrons do not necessarily preclude a uniform density solution for the model unperturbed plasma, but (as will be discussed sec. 4.1.2) may have ramifications for the validity of the assumption of Boltzmann electrons in perturbed systems with a parallel electric field. It should also be noted that for large electron currents the self magnetic field could be important, and there would likely be overall electron heating unless a mechanism for electron cooling and/or inelastic scattering is included. Thus, there may be some issues with applying SCEPTIC3D to problems with a strong parallel electric field, and this is elaborated upon in sec. 4.1.2.

A final point is that parallel electric fields in plasmas may not typically be uniform, and even if they are, the electron and ion densities may not be uniform. That said, provided the gradient scale-length of the field is long compared to the region of plasma considered, a constant field may be an appropriate approximation. Further, situations with uniform electric field and charged particle densities can be conceived, for instance relying on induction, or possibly by means of an external resistive cylinder with a current flowing through it. Thus, calculations with a uniform electric field may be directly applicable to some problems, and may capture the basic physics in others, without necessarily getting the electric field drive for the ion drift quite right.

2.1.3 Neutral Drift

In the absence of a magnetic field, or parallel to one, a background neutral drift should ultimately lead to the ions and electrons drifting with the same (parallel) velocity as the neutrals. The drift velocity will be negligible compared to the electron thermal velocity, so this drift is mainly important for the ions.

If there is a neutral drift perpendicular to a magnetic field, charge-exchange colli-

sions introduce an effective drag on the ions. In the limit where the charge-exchange collision frequency is much smaller than the cyclotron frequency of the ions, the probability of a collision is uniform with respect to the angle to the neutral drift. Thus, the probability of a collision occurring while the ion is above or below the guiding center (with respect to the neutral drift direction) is approximately equal, so there will be no average motion of the ion guiding centers in the direction of the neutral drift. However, since the velocities after a collision are larger in and preferentially drawn in the direction of the neutral drift, there will be average motion of the guiding centers perpendicular to the neutral drift and magnetic field directions. This limit is thus analogous to a constant drag force acting on each ion, which gives rise to a perpendicular drift much like the $\mathbf{E} \times \mathbf{B}$ drift.

In the opposite limit, where the collision frequency is much greater than the cyclotron frequency, the gyro-motion is disrupted, and the ions simply drift with the neutrals. Thus, there must be a transition between these two limits, where the resulting ion drift shifts from perpendicular to parallel to the neutral drift. This transition should occur where the collision and cyclotron frequencies are comparable, since this is where the angular dependence of the collision probability is drastically altered.

2.1.4 Overall Ion Drift

As has previously been discussed, perpendicular and parallel electric fields, as well as neutral drift, can give rise to ion drift. In an average sense, there must be momentum balance for the ions:

$$-\nu_c m_i n_i (\bar{\mathbf{v}}_i - \bar{\mathbf{v}}_n) + e n_i (\mathbf{E} + \bar{\mathbf{v}}_i \times \mathbf{B}) = 0, \quad (2.3)$$

where ν_c is the charge-exchange collision frequency, $\bar{\mathbf{v}}_{i/n}$ the average ion/neutral velocity, n_i the ion density, and e the electron charge. This section treats the components of eq. 2.3 parallel and perpendicular to the magnetic field separately, and then combines them in an expression for the overall ion drift in eq. 2.9.

The parallel component of eq. 2.3 requires that in the presence of charge-exchange collisions, any differential parallel drift between the ions and neutrals must be driven by an electric field. The average parallel drift is thus

$$\bar{\mathbf{v}}_{i\parallel} = \bar{\mathbf{v}}_{n\parallel} + \bar{\mathbf{v}}_{E\parallel}, \quad (2.4)$$

where the average parallel electric field driven drift is

$$\bar{\mathbf{v}}_{E\parallel} = \frac{e \mathbf{E}_\parallel}{\nu_c m_i}. \quad (2.5)$$

For the case of constant collision frequency considered here, an analytic solution is available for the parallel part of the ion distribution function [31]. That solution can be rewritten as

$$f_{i\parallel}(v_{i\parallel}) = \frac{v_{ti}}{2\bar{v}_{E\parallel}} \exp\left(-\frac{(v_{i\parallel} - \bar{v}_{n\parallel})^2}{v_{ti}^2}\right) \text{erfcx}\left(\frac{v_{ti}}{2\bar{v}_{E\parallel}} - \frac{v_{i\parallel} - \bar{v}_{n\parallel}}{v_{ti}}\right), \quad (2.6)$$

where $v_{i\parallel}$ is the component of the ion velocity parallel to the magnetic field (or in the direction of the electric field in the unmagnetized case), $v_{ti} = \sqrt{2T_i/m_i}$ is the ion (i.e. neutral) thermal velocity, and $\text{erfcx}(x) = \exp(x^2) \text{erfc}(x)$ is the scaled complementary error function.

The perpendicular component of eq. 2.3 reduces to the familiar $\mathbf{E} \times \mathbf{B}$ drift in the collisionless case. However, in the presence of charge-exchange collisions the differential motion with the neutrals becomes important. As mentioned previously, the $\mathbf{E} \times \mathbf{B}$ drift can be removed by a transformation to the drifting frame, in which the problem is essentially that of drifting neutrals discussed in sec. 2.1.3. In that frame, the equation for the perpendicular drift becomes

$$-\nu_c m_i n_i (\bar{\mathbf{v}}'_{i\perp} - \bar{\mathbf{v}}'_{n\perp}) + e n_i \bar{\mathbf{v}}'_{i\perp} \times \mathbf{B} = 0, \quad (2.7)$$

where primed quantities are in the moving frame. By separating the components of

$\bar{\mathbf{v}}'_{i\perp}$ perpendicular and parallel to $\bar{\mathbf{v}}'_{n\perp}$ the solution to this equation is found to be

$$\bar{\mathbf{v}}'_{i\perp} = \frac{\bar{\mathbf{v}}'_{n\perp} + \frac{\omega_{ci}}{\nu_c} \bar{\mathbf{v}}'_{n\perp} \times \mathbf{b}}{1 + \frac{\omega_{ci}^2}{\nu_c^2}}, \quad (2.8)$$

where $\omega_{ci} = eB/m_i$ is the ion cyclotron frequency, and $\mathbf{b} = \mathbf{B}/B$ is the unit vector in the direction of the magnetic field.

Transforming back to the stationary frame and adding the parallel drift gives the total average ion drift:

$$\bar{\mathbf{v}}_i = \bar{\mathbf{v}}_{n\parallel} + \mathbf{v}_{E\parallel} + \frac{\bar{\mathbf{v}}_{n\perp} + \frac{\omega_{ci}^2}{\nu_c^2} \mathbf{v}_{E\perp} + \frac{\omega_{ci}}{\nu_c} (\bar{\mathbf{v}}_{n\perp} - \mathbf{v}_{E\perp}) \times \mathbf{b}}{1 + \frac{\omega_{ci}^2}{\nu_c^2}}. \quad (2.9)$$

This average drift satisfies eq. 2.3, and reproduces the expected behavior for the perpendicular drift in the collisionless and collision dominated limits (pure $\mathbf{E} \times \mathbf{B}$ drift and tight coupling to the neutral drift, respectively). At intermediate collisionalities a difference $\bar{\mathbf{v}}_{n\perp} - \mathbf{v}_{E\perp}$ between the perpendicular neutral drift and the $\mathbf{E} \times \mathbf{B}$ drift gives a contribution to the total ion drift that is perpendicular to both that difference and the magnetic field. Since $-\mathbf{v}_{E\perp} \times \mathbf{b} = \mathbf{E}_\perp/B$, this shows that collisions can enable a perpendicular electric field to drive a component of the ion drift along it.

For collisionless plasmas one can simply specify $\bar{\mathbf{v}}_i$ when running SCEPTIC3D, setting its magnitude with the `-v` input and its direction with the `-cd` input (cosine of the angle to the z -axis). However, when including charge-exchange collisions, the ion drift depends on the collision frequency, background electric field, and background neutral drift, so specifying the ion drift directly is not necessarily the best choice. The approach presently taken in SCEPTIC3D is to specify the charge-exchange collision frequency through the `-k` input, the neutral drift through the `-vn`, `-cnd`, and `-psind` (ψ coordinate of the neutral drift) inputs, and the background electric field by setting $\bar{\mathbf{v}}_E$ through the `-v` and `-cd` inputs. The total ion drift is then given by eq. 2.9, though that expression is not used in SCEPTIC3D since the kinetic treatment there automatically produces a distribution function with the right drift.

If the charge-exchange collision frequency is taken to tend to zero in the colli-

sional drift specification scheme, the limit only reproduces the collisionless operation of SCEPTIC3D if no parallel electric field is included. This is because the parallel distribution function given in eq. 2.6 is independent of the collision frequency (E_{\parallel} decreases with ν_c at constant \bar{v}_E_{\parallel}), while that used in the collisionless operation of SCEPTIC3D is a drifting Maxwellian. What the correct ion distribution function is will depend on the specifics of the problem (cause of the drift, how ion–ion collisionality compares to ion–neutral collisionality, etc.), so if a drifting Maxwellian is not thought to be the correct unperturbed distribution in a collisionless case, SCEPTIC3D can be run with negligible collision frequency and an appropriate combination of \bar{v}_E and \bar{v}_n to approximate the correct distribution function.

2.2 Monte Carlo Rejection Scheme

When an ion leaves the SCEPTIC3D computational domain, either through crossing the outer boundary or being collected by the central object, it is reinjected at the outer boundary to keep the (computational) particle number constant. Previously ions to be reinjected could only be drawn from a drifting Maxwellian distribution, so to allow for the more general distribution functions resulting from charge-exchange collisions in combination with external electric and magnetic fields, a new Monte Carlo based reinjection scheme has been developed.

2.2.1 Generating the Unperturbed Distribution Function

The unperturbed system described in Section 2.1 is taken to describe the plasma at the outer edge of the domain. However, though that discussion gave an expression for the average ion drift, it did not give a general form for the ion distribution function. Writing down the ion distribution function analytically is complicated by the fact that it is in general not separable into parallel and perpendicular parts (see the example below). Thus, rather than pursue such a form, the approach taken here is to represent the distribution function statistically by making random velocity draws from the neutral distribution function, and then evolving each ion velocity for the

time since the last collision. Further details of this process are given below.

To illustrate the fact that the ion distribution function is in general not separable, consider the following example: Monoenergetic background neutrals are flowing perpendicular to a magnetic field, and there is a parallel background electric field. The charge-exchange collision frequency is twice the cyclotron frequency of ions with the same perpendicular energy as the neutrals, so on average an ion undergoes one half gyro-orbit before colliding with a neutral. Since the ions have no initial parallel velocity when drawn from the neutral population, their parallel velocity is directly proportional to the time since the last collision. However, so is the absolute phase of the gyro-orbit since all initial velocities are in the same direction. Thus, the parallel and perpendicular components of the ion velocity cannot be treated separately, and the distribution function is not separable.

Calculating the unperturbed ion distribution function is part of the initialization phase of the Monte Carlo reinjection scheme, which is completed before SCEPTIC3D starts the PIC time-stepping process. Since the initialization is only done once for each run of SCEPTIC3D its computational cost is of little consequence, so the main focus has been on making it clear and versatile rather than computationally efficient.

The first step is to generate some number N_{ir} (specified as an input) of post-collision ion velocities, drawn randomly from the neutral distribution function. The neutral distribution is a drifting Maxwellian corresponding to a neutral temperature T_n and drift velocity $\bar{\mathbf{v}}_n$, both specified as inputs to SCEPTIC3D.

Next, the time since the last collision must be calculated for each ion. Since the probability that an ion undergoes a collision is constant per unit time, the collisions are Poisson distributed. Thus, for a collision frequency ν_c specified as an input, the probability that an ion undergoes k collisions in a time Δt is given by

$$p(k, \nu_c \Delta t) = \frac{(\nu_c \Delta t)^k e^{-\nu_c \Delta t}}{k!}. \quad (2.10)$$

Taking $k = 0$ (i.e. allowing no collisions in the time interval to find the time between

collisions) the expression can be solved for Δt to give

$$\Delta t = -\frac{\ln p}{\nu_c}, \quad (2.11)$$

which for p a uniformly distributed random number in $(0, 1]$ gives appropriately distributed times since the last collision.

One point about the Poisson distribution may be worth mentioning here: Since the flight times are Poisson distributed, choosing a point in time and considering all intervals that include that time amounts to sampling the distribution weighted by the interval length, since longer intervals are more likely to contain the specific time considered. The resulting sample is precisely that which one would get from adding two Poisson distributed intervals, which is what is done in SCEPTIC3D when the Monte Carlo reinjection scheme first evolves the injectable velocities for a Poisson-drawn amount of time, and the PIC mover then essentially evolves them for another Poisson-drawn amount of time until their next collision. In fact, the lack of dependence of the time to the next collision on the time since the last collision is used heavily in the PIC mover, where a new time until the next collision is drawn at the beginning of each time step and after each collision, throwing away any knowledge of the time since the last collision at the end of each time-step.

After drawing the initial ion velocities, they must then be evolved for the time since their last collision. In the unmagnetized case this simply involves adding the acceleration due to an external electric field:

$$\Delta \mathbf{v}_E = \frac{e \mathbf{E}}{m} \Delta t, \quad (2.12)$$

where the external electric field is specified through the input $\bar{\mathbf{v}}_E = e \mathbf{E}/(\nu_c m)$.

In the presence of a magnetic field, evolving the ion velocities takes a few more steps. First, the perpendicular component of the velocity in the frame moving at the $\mathbf{E} \times \mathbf{B}$ velocity is rotated by an angle $\phi = \omega_{ci} \Delta t$ around the magnetic axis, corresponding to gyro-motion of the ion. Then, the parallel velocity component is treated as in the unmagnetized case, using the parallel component of the input $\bar{\mathbf{v}}_E$

to set the parallel electric field. Finally, the perpendicular component of $\bar{\mathbf{v}}_E$ (i.e. the $\mathbf{E} \times \mathbf{B}$ drift) is added to the velocity to give the ion velocity in the frame at rest with respect to the object.

The resulting N_{ir} ion velocities statistically represent the unperturbed ion distribution function, and can in principle be replaced by any statistically represented distribution function if future problems call for it. For example, if a more complicated collision cross-section is used, the particle mover of the PIC part of the code can be used to evolve the velocities from an initial guess until a steady-state solution is found for the background distribution.

2.2.2 Determining the Rejection Location

The next step of the initialization process for the re-injection scheme is to determine the probability of injection from each location on the outer boundary. Further, the probability of injecting at each of the N_{ir} ion velocities is calculated for each location. The resulting discrete cumulative probability distributions can then be used to determine where from and with which velocity to reinject an ion during the PIC time-stepping.

To calculate the positional dependence of the injection probability, the outer surface is divided into $N_{\theta,r} \times N_{\psi,r}$ injection faces (both numbers specified as inputs to the code). The faces are uniformly sized in $\cos(\theta)$ and in ψ , similarly to (but independent of) the SCEPTIC3D computational mesh, and the center of the face is used when defining normals etc. Only particles with an inward velocity component are injectable by a given face, and the product of the face area (or solid angle subtended in the spherical case) with the sum of the inward normal velocity of all the particles injectable by a given face is proportional to the probability of injection through that face. Thus, a discrete cumulative probability distribution can be generated (by appropriate summation and normalization) for the probability that an injection occurs from a given face.

For each face a list of references to injectable particles is generated, as well as a cumulative probability function calculated by summing and normalizing the normal

components of their velocities. This will allow an injection velocity to be chosen once a face has been identified, and concludes the initialization process for the reinjection scheme.

During the PIC time-stepping, a particle is reinjected if it leaves the computational domain through the outer boundary or through being absorbed by the central object. To reinject a particle, first an injection face is chosen by drawing a uniformly distributed random number and finding the corresponding face of the (discrete) cumulative probability distribution by means of bisection. Then, one of the particles injectable by that face is chosen by another random number draw and the (binned) cumulative probability distribution for those particles. Finally, a random $\cos(\theta)$ and ψ position is chosen on the given face, which is taken to be the injection position on the outer boundary. It is possible at this point that the velocity is actually slightly outwards at the injection position, since the normal direction there is slightly different than that at the face center. However, such particles will simply leave the domain again and be reinjected, so this is not expected to cause any problems for reasonably sized injection faces.

2.3 Validating the New Rejection Scheme

With the new Monte Carlo reinjection scheme implemented in SCEPTIC3D, it is useful to validate it by inspecting the distributions of injected particles, and to compare the distributions injected by the new scheme to those injected by SCEPTIC (2D) and the original SCEPTIC3D reinjection scheme. This section covers such validation in some detail, and includes examples that elucidate the discussion of ion drift in sec. 2.1.4.

To examine the distributions of the injected particles, the injection locations and velocities of the first 400 000 particles injected by SCEPTIC and SCEPTIC3D were stored in an array in the output file. Only particles injected by the master node were stored, since the values of its arrays are the ones which are written to the output file at the end of the run. However, there is no parallel computation aspect

to the reinjection scheme at present, so the only differences expected for the particles injected by another computational node are those due to a different seed being used for its pseudo-random number-generator.

Since only the injected particles are of interest, and since the Monte Carlo reinjection scheme does not have a dependence on the potential at the boundary, the runs used for the validation comparisons do not need a fine potential grid or to be run to convergence; only to be run for long enough that 400 000 particles are injected by the master node. Further, since the size of the PIC time-step is of no importance to the injected particles, a large time-step can be used to ensure that many particles are reinjected per step, thus making the comparison runs quite quick.

Because of the way SCEPTIC3D is parallelized, each node needs to be able to inject a particle from any of the discrete faces that make up the outer boundary in the Monte Carlo reinjection scheme. Thus, each node needs to store a list of, and cumulative probability distribution for, the particles injectable by each of those faces, which comes at a storage cost that scales like $N_{\theta r} \times N_{\psi r} \times N_{ir}$. The parameters used for each of the comparison runs are $N_{\theta r} = 30$, $N_{\psi r} = 30$, and $N_{ir} = 100 000$, which for one real and one integer array give a total memory cost per node of 687MB. That is already undesirably large, so the present parameters likely represent an upper limit for the number of faces used to represent the outer surface on the current architecture. To move beyond this limit, nodes with more memory would be needed, or a shift towards a parallelization scheme where each node only needs to be able to reinject particles from part of the outer surface.

2.3.1 Collisionless Validation Against SCEPTIC3D

The original SCEPTIC3D reinjection scheme could handle reinjection in the collisionless case, allowing for magnetic fields and perpendicular and parallel ion drifts. The newly implemented Monte Carlo reinjection scheme should thus be able to reproduce the behavior of the old reinjection scheme for collisionless runs, and as this section shows that is indeed the case.

Table 2.1 summarizes the results of the comparisons of the Monte Carlo reinjection

scheme with the the old SCEPTIC3D reinjection scheme. The two schemes are in agreement for all the cases considered, which range from the simplest possible run with no drift or magnetic field, to a run with a magnetic field and ion drift, both of which are misaligned with each other and the z -axis.

Input parameters				
<code>bz</code>	<code>cB</code>	<code>v</code>	<code>cd</code>	Reinjection schemes agree?
0	0	0	0	Yes
0	0	2	0.2	Yes
1	0.2	0	0	Yes
1	0.2	2	0.2	Yes
1	0.2	2	0.4	Yes; see figures 2-1–2-9

Table 2.1: Summary of the comparisons performed between the Monte Carlo reinjection scheme and the old SCEPTIC3D reinjection scheme. The input parameters are named and given as when calling SCEPTIC3D, with `bz` being the strength of the magnetic field, `cB` being the cosine of the angle between the magnetic field and the z -axis, `v` being the ion drift, and `cd` being the cosine of the angle between the ion drift direction and the z -axis. All quantities are in the units used by SCEPTIC3D (see sec. 1.3.2), so the ion drift is in units of c_s , while the magnetic field is specified through the ion cyclotron frequency in units of c_s/r_p . Even the most complex collisionless case possible in SCEPTIC3D, with a magnetic field and ion drift misaligned with each other and with the z -axis, shows agreement between the Monte Carlo scheme and the old reinjection scheme. This case is examined in more detail in the text and listed figures.

The locations and velocities of the injected particles span a 5D subspace of their 6D coordinates. A rigorous comparison between two injected distributions is thus difficult, but much confidence can be gained in the agreement of the two schemes by considering projections of the distributions onto smaller subspaces. In particular, the two 3D subspaces for velocities and positions can easily be compared qualitatively, while a more quantitative comparison can be made in each of the six 1D subspaces simply by inspecting the binned histograms of the projected distributions.

In all cases considered in the comparison between the Monte Carlo reinjection scheme and the old SCEPTIC3D reinjection scheme, the two appear to be in agreement. Therefore, only the most complex of those cases is considered in detail here, with the intention of illustrating the comparison procedure and offer insight into the

workings of the the reinjection scheme. The case considered corresponds to the last row of tab. 2.1, and has a magnetic field lying in the y - z plane such that the cosine of it's angle to the z -axis is 0.2, as well as an ion drift in that same plane with a cosine of the angle to the z -axis equal to 0.4. The ion drift thus has components both parallel to and perpendicular to the magnetic field, and neither the magnetic field nor the drift are aligned with the z -axis.

Injected Velocities

Figure 2-1 shows the 3D velocity of the first 5 000 injected particles for the above-mentioned case. The samples from each of the two distributions appear to be in qualitative agreement, with both distributions showing a clustering around a net drift in the \mathbf{e}_y and \mathbf{e}_z directions, and similar tapering off with distance from the average drift in all directions. The 1D projections of the two distributions onto each velocity axis are examined in figures 2-2–2-4.

As is seen in figures 2-2–2-4, the agreement between the Monte Carlo reinjection scheme and the old SCEPTIC3D reinjection scheme also holds in a quantitative sense. The projections of the distribution of velocities injected by the Monte Carlo scheme do exhibit larger fluctuations than those of the distribution injected by the old reinjection scheme, especially near the peaks of the distributions, and this is seen in all three figures. The fluctuations in the Monte Carlo scheme are thus larger than what one would expect from standard Gaussian counting fluctuations, since those are also present for the old SCEPTIC3D reinjection scheme.

That the Monte Carlo scheme exhibits larger fluctuations in the injected distribution is not surprising, since there are several ways in which the discretization of the outer surface and the statistical representation of the injectable particle distribution can contribute to such fluctuations. Ultimately, every injected particle on a given computational node can be traced back to one of the N_{ir} velocities evolved under the Monte Carlo scheme on that node. Those velocities statistically represent a 3D velocity distribution, and a single node typically does not have a large enough N_{ir} to keep the noise in that distribution low. However, since the nodes each use a

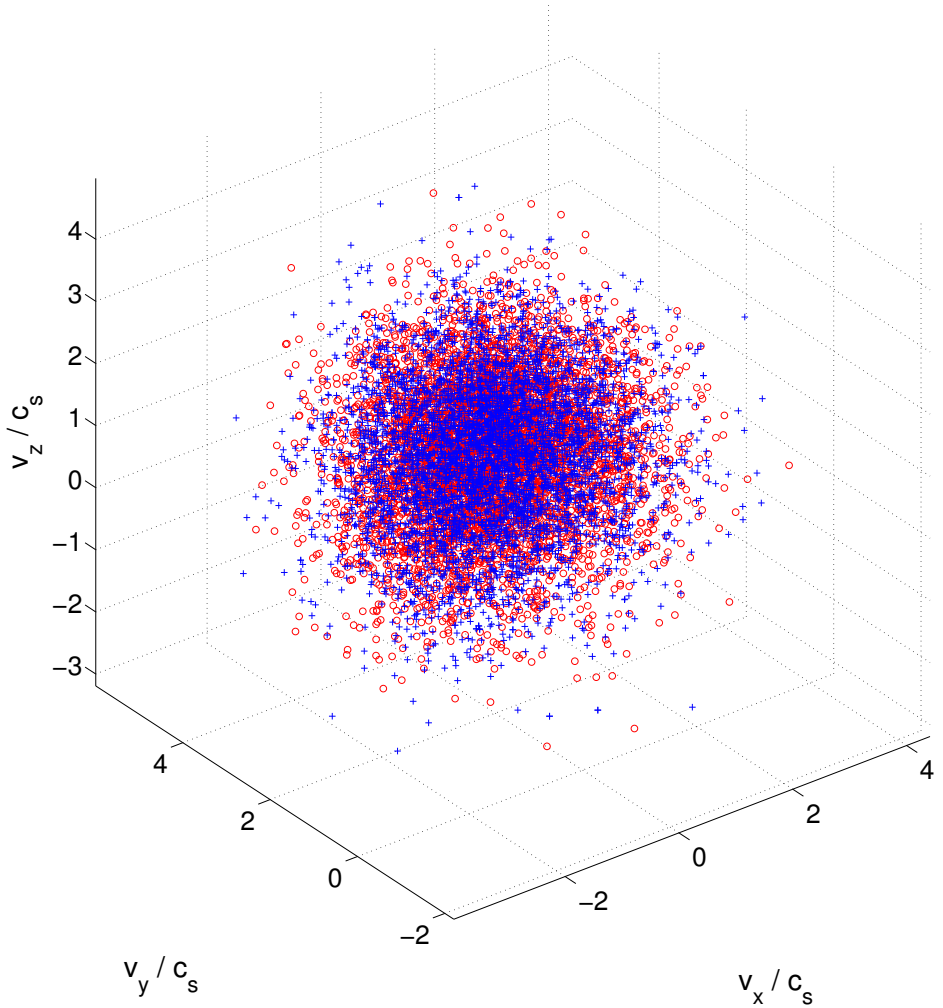


Figure 2-1: Velocity of the 5 000 first particles injected by the Monte Carlo reinjection scheme (blue crosses) and the old SCEPTIC3D reinjection scheme (red circles). The two samples of the respective distributions appear to be in good agreement, both being centered at a net drift in the e_y and e_z directions, and with similar tapering off with distance from the average drift in all directions.

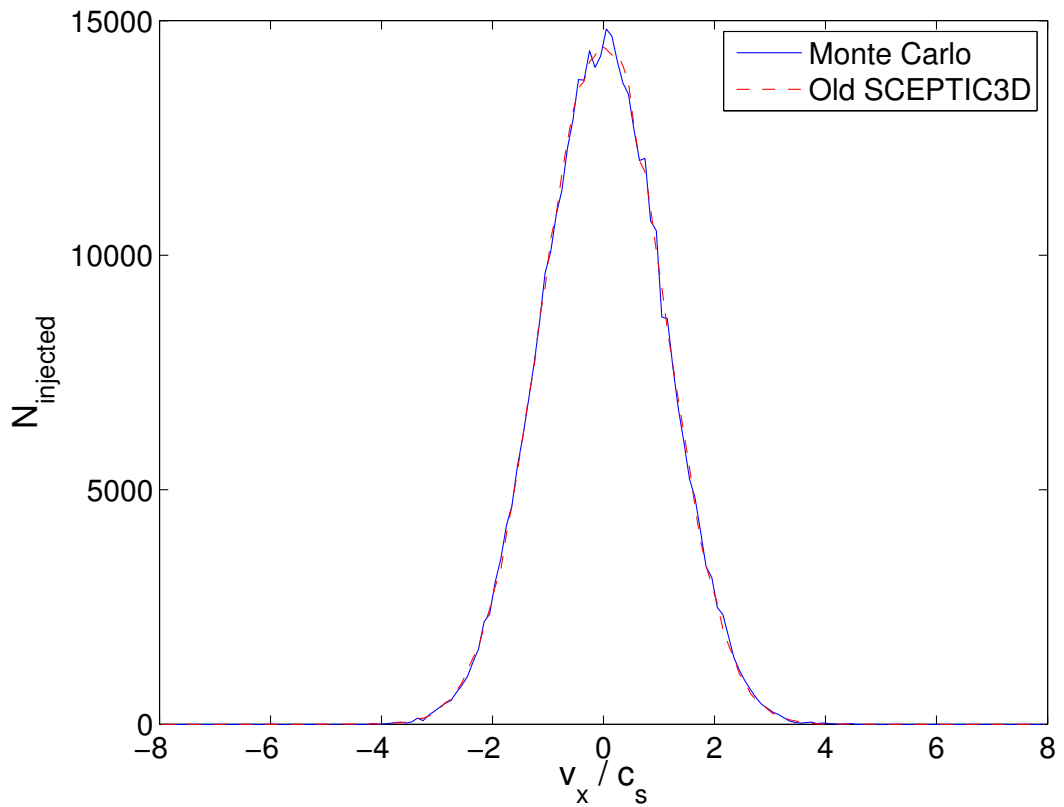


Figure 2-2: Projection onto the v_x -axis of the distributions of injected velocities, binned with bin-size 0.1. The two distributions are in good agreement, with slightly larger fluctuations seen for that corresponding to the Monte Carlo reinjection scheme, especially near the peak. As expected, no average drift is seen in the e_x direction.

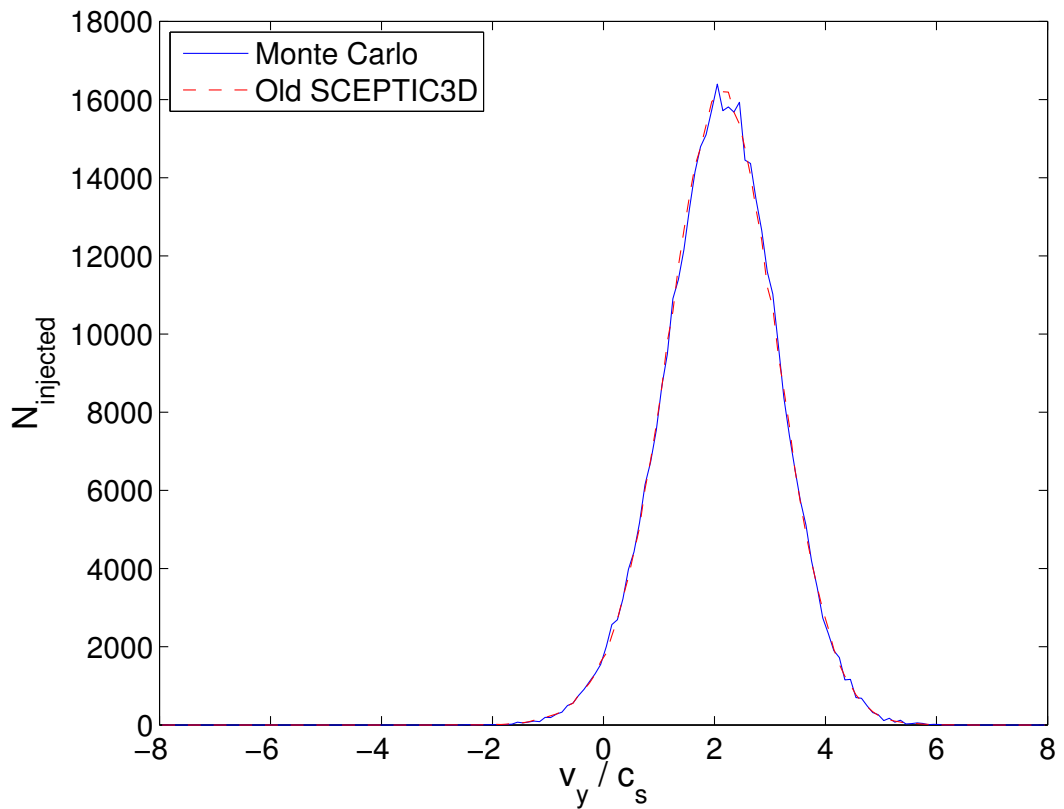


Figure 2-3: Projection onto the v_y -axis of the distributions of injected velocities, binned with bin-size 0.1. Also here the most noticeable fluctuations are near the peak of the distribution injected by the Monte Carlo scheme, but the two distributions are in generally good agreement. The distributions peak just above $v_y = 2c_s$.

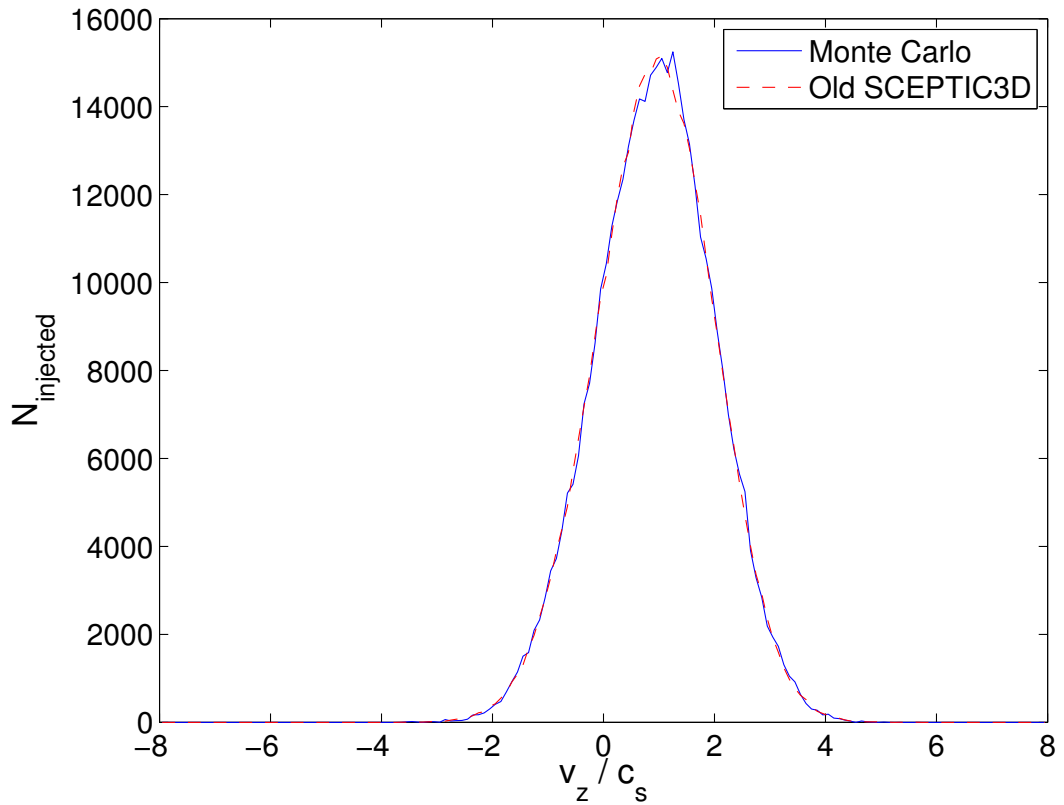


Figure 2-4: Projection onto the v_z -axis of the distributions of injected velocities, binned with bin-size 0.1. Also here the most noticeable fluctuations are near the peak of the distribution injected by the Monte Carlo scheme, but the two distributions are in generally good agreement. The distributions peak around $v_z = c_s$.

different seed for their pseudo-random number-generator, fluctuations that arise in the injected particle distribution due to inadequate statistical representation of the injectable velocity distribution should average out when many nodes are used.

Distortions of the injected velocity distribution due to the discretization of the outer surface is another issue. The fact that the injection probability is computed for a discrete set of points, rather than in a continuous fashion, means that even in the limit of perfect sampling the distribution of velocities injected by the Monte Carlo scheme would differ from that injected by the old SCEPTIC3D reinjection scheme. This is because each computational node discretizes the outer surface in the same way, so the resulting distortions to the distribution are systematic rather than random, and thus do not average out. However, given the good general agreement between the distributions injected by the two reinjection schemes, it would appear that the level of discretization used for the outer surface is adequate. Combined with the averaging over the random fluctuation between computational nodes, it is thus expected that using the Monte Carlo reinjection scheme should yield equivalent results from SCEPTIC3D as if using the old reinjection scheme.

The average drift of the underlying distribution of injectable velocities is $2c_s$, directed such that the cosine of the angle to the z axis is 0.4 in the y - z plane (with positive average v_y). Thus, the average drift of the underlying distribution is $1.8c_s$ in the \mathbf{e}_y direction and $0.8c_s$ in the \mathbf{e}_z direction. However, since velocities with larger inward radial velocity components are more likely to be selected, the distribution resulting from the biased draw actually tends to have a larger average drift than the underlying distribution. This is seen in figures 2-3-2-4, where the peak of the projections of the distribution are at larger velocity than expected from the average drift of the underlying distribution.

The projection of the injected velocity distribution onto the v_x -axis shown in fig. 2-2 displays no average drift, and represents a symmetric distribution around $v_x = 0$. The shape is not Gaussian, though that is the shape of the projection of the underlying distribution of injectable velocities. The reason for this is that the injection probability is weighted by the inward radial component of the velocity at

the reinjection point, which leads to a non-uniform sampling of the distribution of injectable velocities. Thus, another interesting thing to look at is the distribution of injected radial velocity components, which is shown in fig. 2-5.

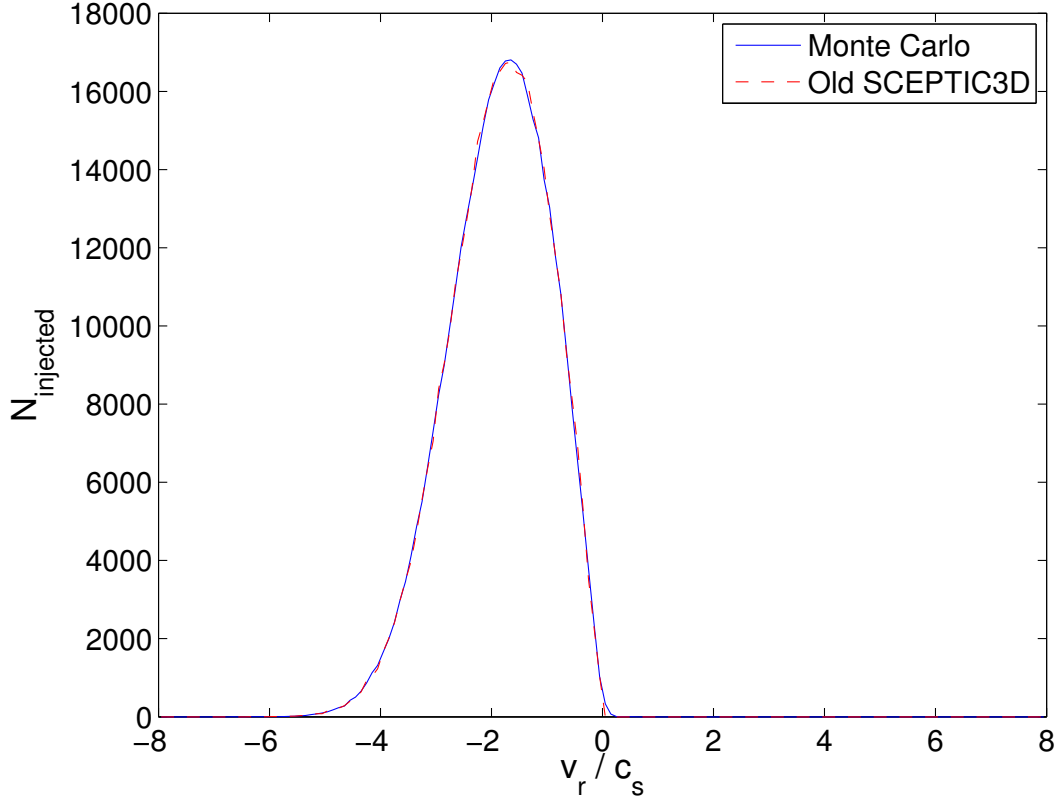


Figure 2-5: Distribution of radial components of the injected velocities, binned with bin-size 0.1. There is good agreement between the Monte Carlo reinjection scheme and the old SCEPTIC3D reinjection scheme, though one notable deviation is the presence of some velocities with an outward radial component for the Monte Carlo scheme.

One notable point about the distributions of radial injected velocity components shown in fig. 2-5 is the presence of ‘injected’ particles with an outgoing radial velocity component for the Monte Carlo scheme. These are the result of the discretization of the outer boundary into faces for the purposes of calculating the reinjection probability. Since the reinjection probability is calculated at a point, and the reinjection location then chosen at random in the solid angle subtended by that face, particles with small inwards radial velocity components at the point where the injection prob-

ability is calculated can end up with small outwards radial velocity components at the reinjection location. However, since velocities with small inward radial components are unlikely to be drawn, this problem is less significant than one might expect, and even at the level of discretization of the outer surface presently used the effect appears negligible. Further, as is pointed out in sec. 2.2.2, particles with an outward radial velocity component just leave the domain at the next time-step, and are then reinjected. Thus, provided the discretization of the outer surface doesn't significantly perturb the injected velocity distribution, the effect of that discretization is unimportant, as evidenced by fig. 2-5.

Injection Locations

Having examined the injected velocities, it is also useful to look at the locations selected for particle reinjection. The locations selected by the Monte Carlo reinjection scheme should be consistent in an average sense with those selected by the old SCEPTIC3D reinjection scheme, which it turns out they are.

Figure 2-6 shows the 3D injection locations of the 5 000 first particles injected by each of the two reinjection schemes. All the injection locations lie on a sphere of radius $5r_p$, which was the size of the outer domain chosen for the comparison runs of SCEPTIC3D. Since there is an average drift with positive components in the \mathbf{e}_y and \mathbf{e}_z directions, particles are more likely to be reinjected on the side where that corresponds to an inward radial direction. This is seen in the figure, where there is a higher density of reinjection locations for negative y and z than for positive values. The 1D projections of the two distributions onto each coordinate axis are examined in figures 2-7–2-9.

For an isotropic distribution of injectable velocities, each of the curves shown in figures 2-7–2-9 would be flat since the probability of injection would be uniform across the outer boundary. However, for the case considered in these figures there is an average drift, and so the weighting of the injection probabilities by the inward radial velocity components skews the distributions of injection locations.

Projected onto the x -axis the distributions of injection locations are seen in fig. 2-7

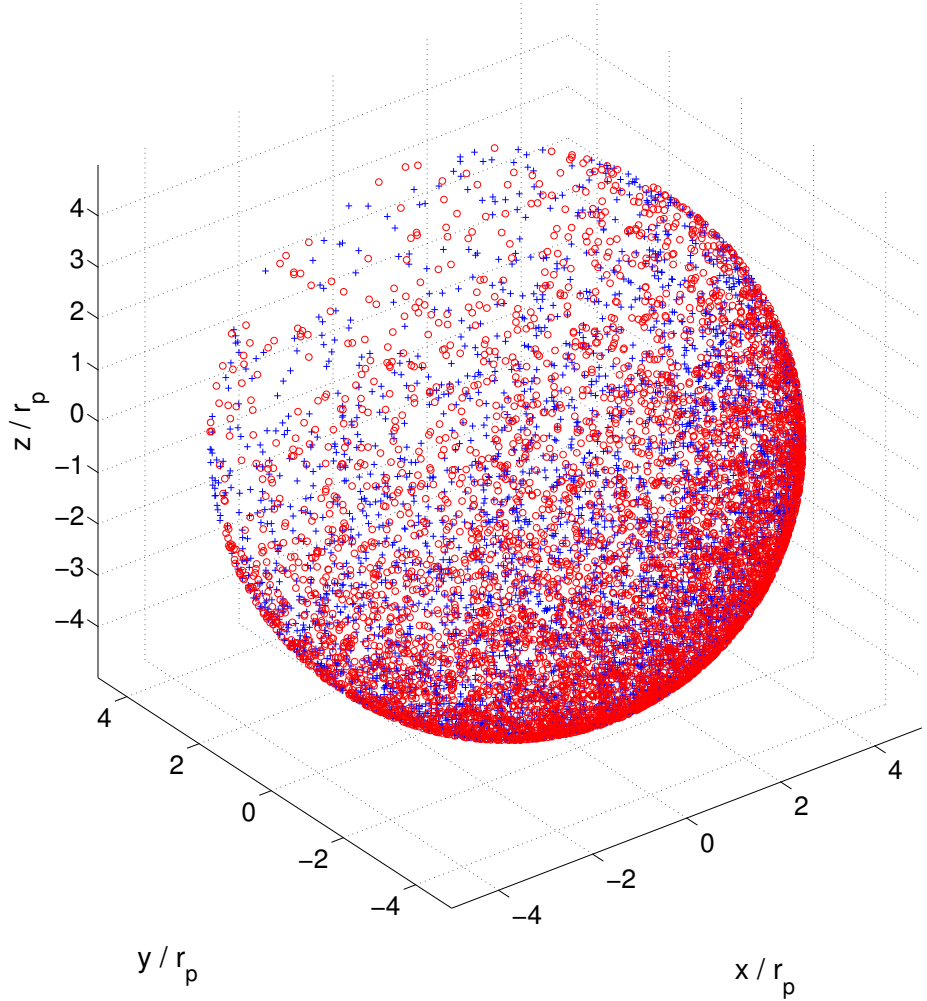


Figure 2-6: Injection location for the first 5 000 particles injected by the Monte Carlo reinjection scheme (blue crosses) and the old SCEPTIC3D reinjection scheme (red circles). The two samples of the respective distributions appear to be in good qualitative agreement, with a higher density of reinjection locations on the side with negative y and z coordinates than on the opposite side.

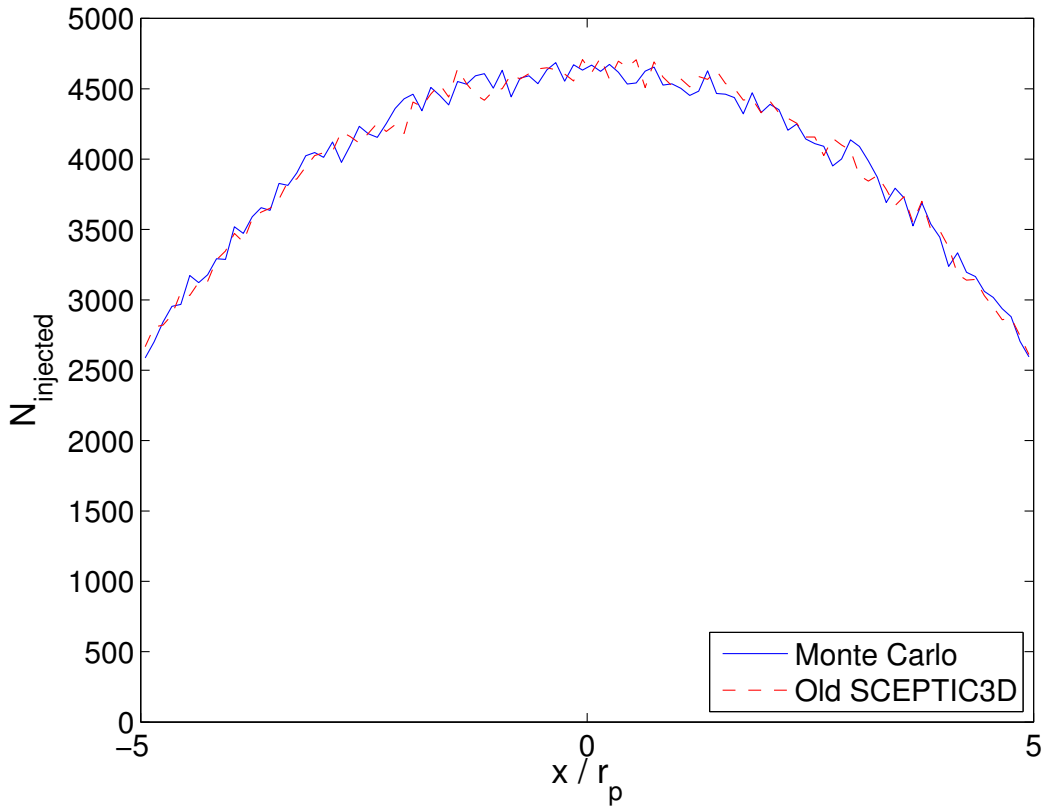


Figure 2-7: Projection of the distributions of injection locations onto the x -axis, binned with bin-size 0.1. The Monte Carlo and old SCEPTIC3D reinjections schemes are in good agreement, and both display similar levels of fluctuations. A larger number of particles are reinjected near $x = 0$ than towards $x = \pm 5r_p$, and the projected distribution appears symmetric about $x = 0$.

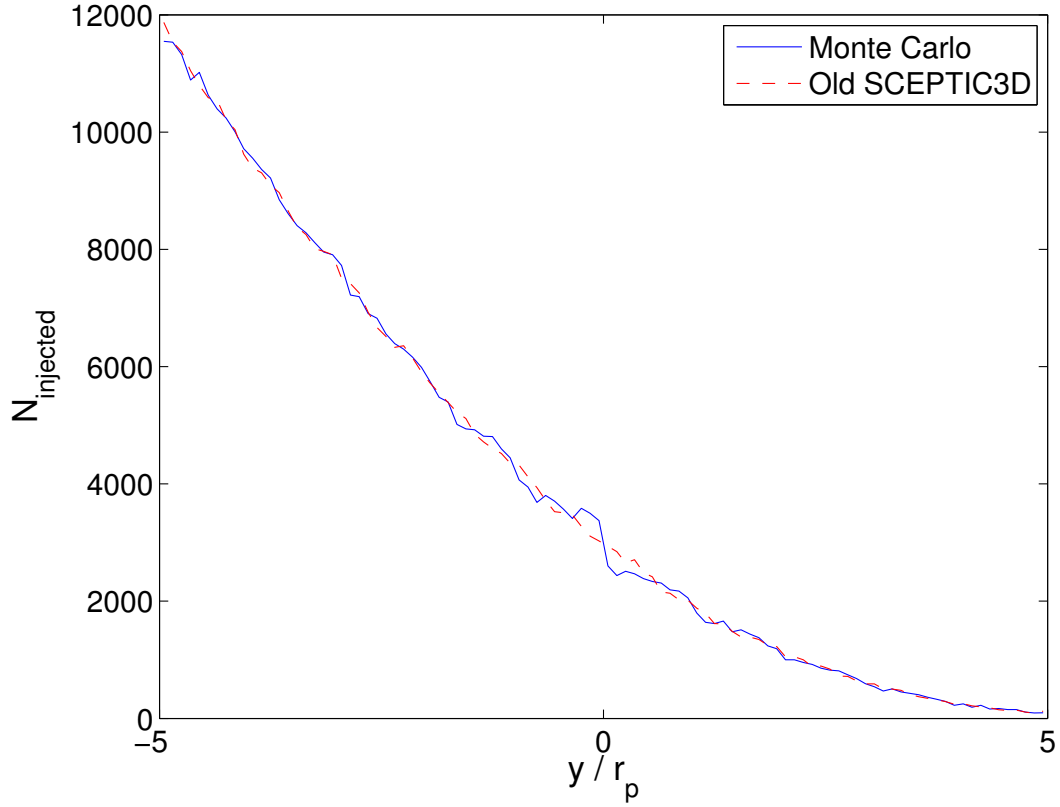


Figure 2-8: Projection of the distributions of injection locations onto the y -axis, binned with bin-size 0.1. The Monte Carlo and old SCEPTIC3D reinjections schemes are in good agreement, and both display similar levels of fluctuations except for a possible artifact in the curve due to the Monte Carlo scheme near $y = 0$. Very few particles are injected near $y = 5r_p$, and the projected distributions increase monotonically towards $y = 5r_p$.

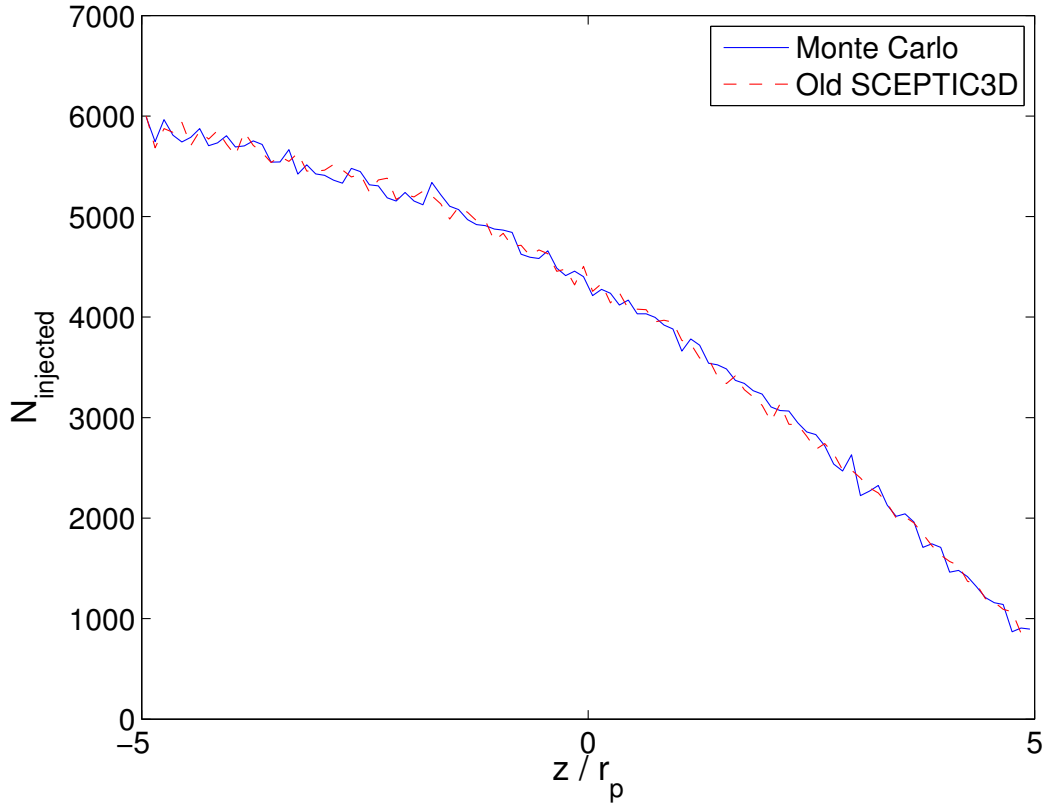


Figure 2-9: Projection of the distributions of injection locations onto the z -axis, binned with bin-size 0.1. The Monte Carlo and old SCEPTIC3D reinjections schemes are in good agreement, and both display similar levels of fluctuations. There are six times as many particles injected near $z = -5r_p$ as near $z = 5r_p$, and the change between those two extremes is monotonic.

to be symmetric about $x = 0$, and to be peaked there. The symmetry arises from the fact that there is no drift in the \mathbf{e}_x direction, so there is nothing to differentiate the \mathbf{e}_x and $-\mathbf{e}_x$ directions. The preferential injection near $x = 0$ is related to the dependence of the inward radial direction on x : Near $x = \pm 5r_p$ the inward radial direction is almost entirely in the $\mp \mathbf{e}_x$ direction, while at $x = 0$ it has no component in the \mathbf{e}_x direction. The average drift in the $y-z$ plane thus affects the injection probability near $x = 0$ by altering the inward radial velocity component, balancing this by an opposite change near $x = \pm 5r_p$, where the drift is perpendicular to the radial direction and thus does not matter. One might think that the increase in injection probability on the side of the sphere facing the drift would be canceled by the decrease in injection probability on the side trailing the drift, which would be the case for an unbiased draw of injection velocities, but since the probabilities are weighted by the inward radial velocity component the increase in injection probability of velocities with a large inward radial component is larger than the decrease in those with a small such component on the opposite side of the outer boundary. Thus, the injection probability near $x = \pm 5r_p$ is reduced to balance the net increase near $x = 0$, since the integral of the probability density distribution must equal one.

Figure 2-8 shows the projection of the distribution of injection locations onto the y -axis. The injection probability is largest near $y = -5r_p$, and drops monotonically to almost zero near $y = 5r_p$. As mentioned, this is because the average drift in the \mathbf{e}_y direction increases the injection probability on the side of the outer boundary facing the drift, and decreases it on the side trailing the drift, as one would expect.

There is a noticeable feature near $y = 0$ in the curve corresponding to the Monte Carlo reinjection scheme in fig. 2-8, which stands out as larger than the typical fluctuations seen elsewhere on the two curves. This feature can likely be traced back to the discretization of the outer boundary in the Monte Carlo reinjection scheme, which prevents a smooth transition of the inward radial component of the average drift from positive to negative as y passes through zero. Since the injection probabilities are calculated at points offset from $y = 0$, particles injected at slightly negative y will have an enhanced injection probability, while particles injected at slightly pos-

itive y will have a suppressed injection probability. The feature seen in the figure is consistent with this idea, and it is worth noting that this is unlikely to be important in SCEPTIC3D runs since particles injected near $y = 0$ are likely to leave the domain shortly thereafter, since they have a large average drift in the \mathbf{e}_y direction.

Figure 2-9 shows the projection of the distribution of injection locations onto the z -axis. The injection probability is largest near $z = -5r_p$, and drops monotonically by about a factor of six towards $z = 5r_p$. The behavior seen in this figure is a mix between that seen for the projections onto the x and y axes, since there is a drift in the \mathbf{e}_z direction, but the drift in the \mathbf{e}_y direction is large enough to affect the projection onto the z -axis in a similar way to the projection onto the x -axis.

2.3.2 Collisional Validation Against SCEPTIC

The new Monte Carlo reinjection scheme can be validated against that in SCEPTIC (2D) in the collisional regime. SCEPTIC allows one to specify both neutral and ion parallel drifts with or without a magnetic field, and in all cases considered good agreement is seen between SCEPTIC3D and SCEPTIC¹.

Table 2.2 summarizes the comparisons of the new Monte Carlo reinjection scheme in SCEPTIC3D with the reinjection scheme in SCEPTIC. In SCEPTIC the total ion drift is specified through the input `-v`, while in SCEPTIC3D only the electric field driven drift is specified through `-v`. Thus, specifying the same problem in the two codes requires different `-v` inputs when a neutral drift is included, and this is reflected in the table.

The projections of the distributions of injected velocities onto the v_z -axis are examined for three of the cases in figures 2-10–2-12. The three cases are chosen to illustrate the effect of electric field and/or neutral driven drifts on the distribution of injected particles.

The first of the three cases has no neutral drift, but an ion drift parallel to a magnetic field. It is shown in fig. 2-10, and the two injection schemes are seen to be

¹An initial comparison revealed that neutral drifts had not been fully implemented in the SCEPTIC reinjection scheme, but this was swiftly remedied by Ian Hutchinson.

Input parameters					
kt	bz	v		vn	Reinjection schemes agree?
		(2D)	(3D)		
0.01	0	0	0	0	Yes
0.01	1	0	0	0	Yes
0.01	0	2	2	0	Yes
0.01	1	2	2	0	Yes; see fig. 2-10
0.01	0	2	0	2	Yes
0.01	1	2	0	2	Yes; see fig. 2-11
0.01	0	2	-1	3	Yes
0.01	1	2	-1	3	Yes; see fig. 2-12

Table 2.2: Summary of the comparisons performed between the new Monte Carlo reinjection scheme in SCEPTIC3D and the reinjection scheme in SCEPTIC. The input parameters are named and given as when calling SCEPTIC(3D), with **kt** being the charge-exchange collision frequency, **bz** being the strength of the magnetic field, **v** being the ion drift specified for SCEPTIC (2D) and SCEPTIC3D (3D), and **vn** being the neutral drift velocity. All quantities are in the units used by SCEPTIC/SCEPTIC3D (see sec. 1.3.2), so the ion and neutral drifts are in units of c_s , and the magnetic field is specified through the ion cyclotron frequency, which together with the charge-exchange collision frequency is given in units of c_s/r_p . The **-v** input differs for the two codes in some cases because they specify the ion drift differently, but the two reinjection schemes are seen to agree for all cases considered.

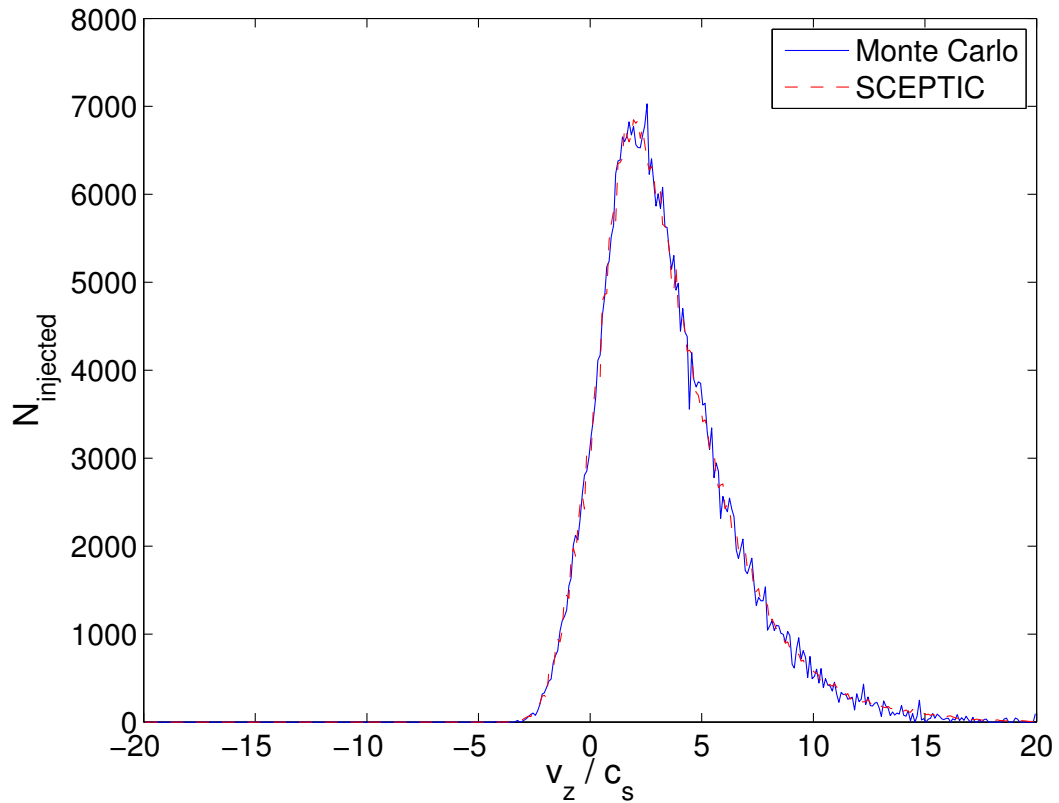


Figure 2-10: Projection onto the v_z -axis of the distributions of injected velocities, binned with bin-size 0.1, for a case with ion drift aligned with a magnetic field. The Monte Carlo and SCEPTIC reinjection schemes are in good agreement, though there are significantly larger fluctuations on the distribution injected by the Monte Carlo scheme, especially at large v_z .

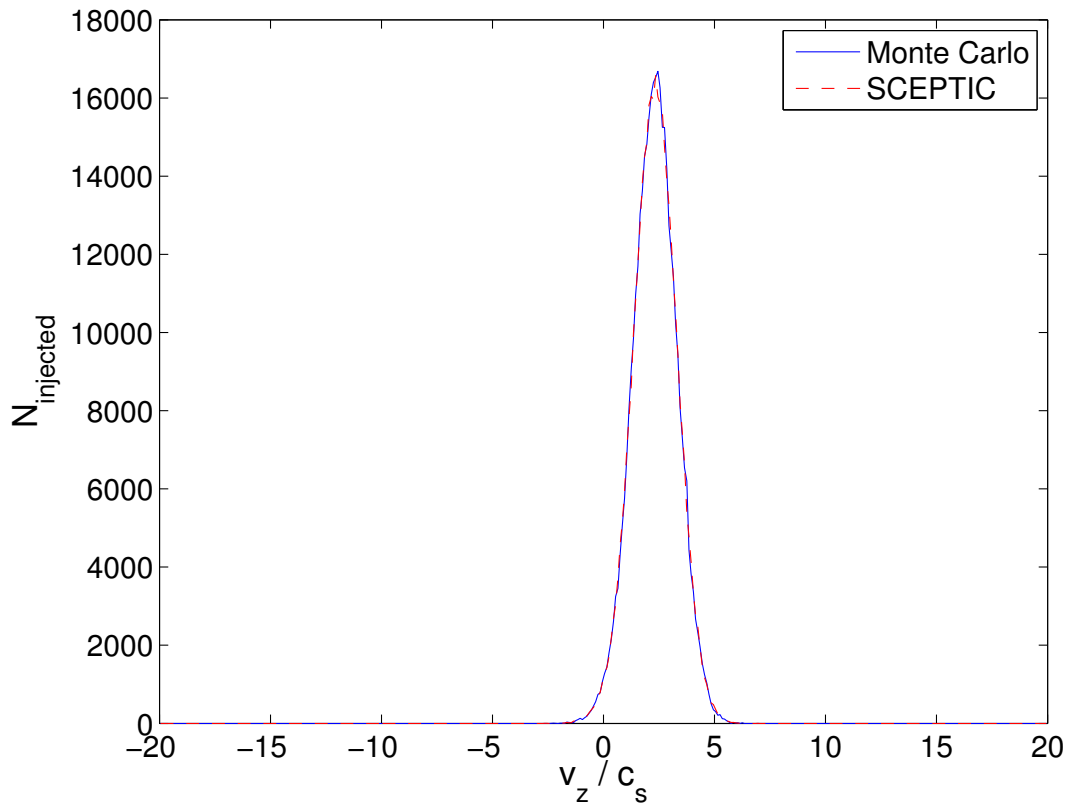


Figure 2-11: Projection onto the v_z -axis of the distributions of injected velocities, binned with bin-size 0.1, for a case with neutral drift aligned with a magnetic field. Both injected distributions peak at a drift slightly above $2c_s$, and are in good agreement.

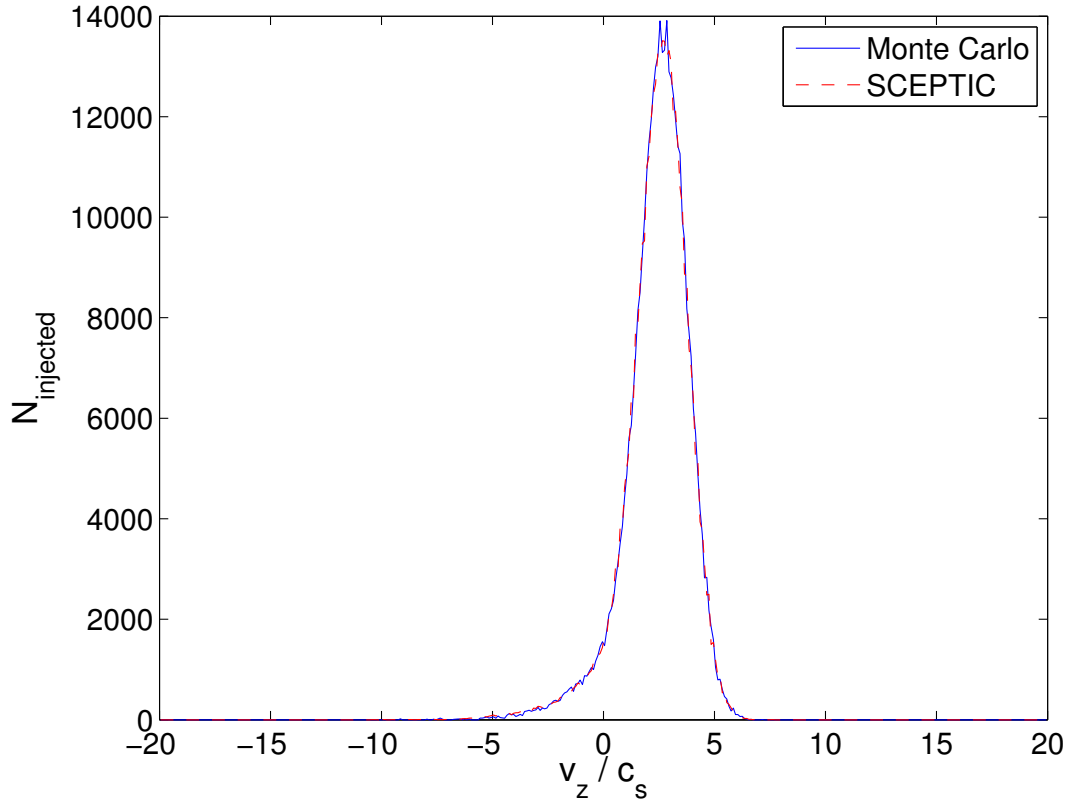


Figure 2-12: Projection onto the v_z -axis of the distributions of injected velocities, binned with bin-size 0.1, for a case with neutral and relative ion drift aligned with a magnetic field. The injected distributions show similarities to those injected for only a neutral drift, but with a tail drawn out towards negative v_z . Again the two injected distributions are in good agreement, though that of the Monte Carlo scheme appears to have two sharp features near its peak.

in good agreement. The parallel ion drift is driven by an electric field, and balanced by the drag from charge-exchange collisions. This pulls out a tail of ions with large v_z , as is seen in the figure. The underlying distribution of velocities is characterized by eq. 2.6, from which a biased draw gives that shown in fig. 2-10.

One thing to note in fig. 2-10 is that there are significant fluctuations in the curve corresponding to the Monte Carlo reinjection scheme, especially at large v_z . This is due to the previously discussed fact that distribution of injectable velocities is not statistically represented all that well on any individual computational node. The fluctuations due to this are exacerbated by the fact that the poorly sampled large velocities of the underlying distribution are preferentially selected, such that the relative fluctuations get larger at higher v_z . Again though, these fluctuations should average out when using many computational nodes, which one typically does for SCEPTIC3D.

The second of the three cases has no electric field driven drift, but has a neutral drift aligned with a magnetic field. It is shown in fig. 2-11, where both SCEPTIC and SCEPTIC3D adds a drift in the \mathbf{e}_z direction as expected.

The final of the three cases examined is shown in fig. 2-12. It has neutral and relative ion drifts specified in opposite directions, but both parallel to the magnetic field (as they must for comparison with the 2D code SCEPTIC). The main feature is the neutral drift in the \mathbf{e}_z direction, but it is also seen that the relative ion drift in the opposite direction is present through a tail drawn out as for the cases with only ion drift. The projections of the distributions of velocities injected by the Monte Carlo scheme and by SCEPTIC are in good agreement, though there appear to be two sharp features near the peak of the Monte Carlo injected distribution, which have not been investigated further at present.

Chapter 3

Upgrades to SCEPTIC3D

In addition to the new reinjection scheme described in sec. 2.2, several other upgrades and modifications have been made to SCEPTIC3D. The following sections detail that work, which includes a new distribution function diagnostic, improvements to the Poisson solver, and a new output system based on HDF5.

3.1 Distribution Function Diagnostic

Motivated by possible comparisons of SCEPTIC3D results with laser-induced fluorescence (LIF) measurements of the ion distribution function near spherical probes at the VINETA experiment [13], a new distribution function diagnostic has been added to SCEPTIC3D. The LIF measurements can capture the 1D (velocity) distribution function along each of two axes at any point in a plane, and so matching (or better) capabilities are required for the new diagnostic.

At each time-step the computational ions in a PIC code statistically represent the ion distribution function. However, though the number of computational ions is large enough to ensure a reasonably low noise level in the charge density used for solving the Poisson equation, a distribution function generated from the velocities at a single time-step would be quite noisy unless a far greater number of computational ions were used. Thus, a better approach for the steady-state problems tackled with SCEPTIC3D is to use the computational ions at many different time-steps to generate

a binned distribution function. This approach is used for several other diagnostics in SCEPTIC3D, which compute specific moments of the distribution function, and is also adopted for the new diagnostic. To ensure that only the final converged solution is sampled, only the last 20% of the time-steps are considered, and to decrease the statistical dependence due to counting the same ion multiple times in one bin, only every fourth time-step is sampled.

Storing the full 3D3v (three spatial, and three velocity dimensions) distribution function quickly becomes prohibitive for fine spatial and/or velocity resolutions, and a very large number of computational ions is required to populate it. Further, comparisons with LIF measurements only require two 2D1v distribution functions, so a full 3D3v distribution is not required. Thus, to allow comparisons with LIF measurements in any plane on the basis of a single SCEPTIC3D run, the new diagnostic is designed to store all three 3D1v distribution functions on a Cartesian grid.

For a full 3D3v distribution function $f_i(\mathbf{x}, \mathbf{v})$, the 3D1v distribution in the \mathbf{e}_y direction is

$$\langle f_i \rangle_{v_x, v_z}(\mathbf{x}, v_y) = \int_{-\infty}^{\infty} \int_{-\infty}^{\infty} f_i(\mathbf{x}, \mathbf{v}) dv_x dv_z, \quad (3.1)$$

with the 3D1v distributions in the two other directions defined similarly. Though much information is lost in this averaging, the remaining 3D1v distributions still capture most of the aspects of interest, especially if the drifts and fields are chosen to be aligned with the Cartesian axes.

3.1.1 VINETA-Relevant Velocity Distributions

As an example to illustrate the capabilities of the new diagnostic, SCEPTIC3D has been run for parameters relevant to what are considered strongly magnetized runs on the VINETA experiment: Probe potential $\phi_p = -T_e/e$, ion to electron temperature ratio $T_i/T_e = 0.05$, ion cyclotron frequency $\omega_{ci} = 0.03 c_s/r_p$ (with $\mathbf{B} \parallel \mathbf{e}_z$), and electron Debye length $\lambda_{De} = 0$. The velocity distribution in the \mathbf{e}_y direction has been examined in the cells of the Cartesian grid closest to but not intersecting the probe in each of the three directions, and are presented in Figures 3-1, 3-2, and 3-3. Because

of the symmetries of the problem considered, the distributions at the two points for a given direction should be consistent with each other provided one is plotted against $-v_y$.

Figure 3-1 shows that the ions have a strong inward radial drift close to the probe, which is of magnitude $\sim 0.5 c_s$. The velocities of the injected ions have standard deviation $\sqrt{0.05} c_s \approx 0.22 c_s$, so the distributions shown in the figure appear to be consistent with the injected distribution being accelerated towards an attracting probe biased to $\phi_p = -T_e/e$. The slight asymmetry about the mean drift is not surprising, since particles from the initial distribution that have large inward radial velocities also are likely to have significant angular momentum, which may prevent them from reaching the locations considered. The velocity distribution near the probe is thus partially suppressed for the largest inward radial velocities, as is seen in the figure.

The distributions shown in fig. 3-2 show significant broadening of the distribution of tangential velocity compared to the injected distribution. This is because angular momentum conservation requires that the tangential velocity increase as the radial distance is decreased, broadening the distribution near the probe.

The distributions shown in fig. 3-3 are broadened similarly to those in fig. 3-2, but have an additional asymmetry corresponding to a drift in the $\mp \mathbf{e}_y$ direction. This is essentially $\mathbf{E} \times \mathbf{B}$ drift from the component of the radial electric field due to the probe perpendicular to the background magnetic field. However, the Larmor radius is not small compared to the gradient scale-length of the electric field, so the impact on the distribution function is more complicated than the pure shift one would expect from the guiding center picture.

3.1.2 VINETA-Relevant Distribution Moments

Often what is actually presented from LIF measurements are the first two moments of the distribution function: The drift

$$\bar{\mathbf{v}}_y(\mathbf{x}) = \int_{-\infty}^{\infty} v_y \mathbf{e}_y \langle f_i \rangle_{v_x, v_z} dv_y \quad (3.2)$$

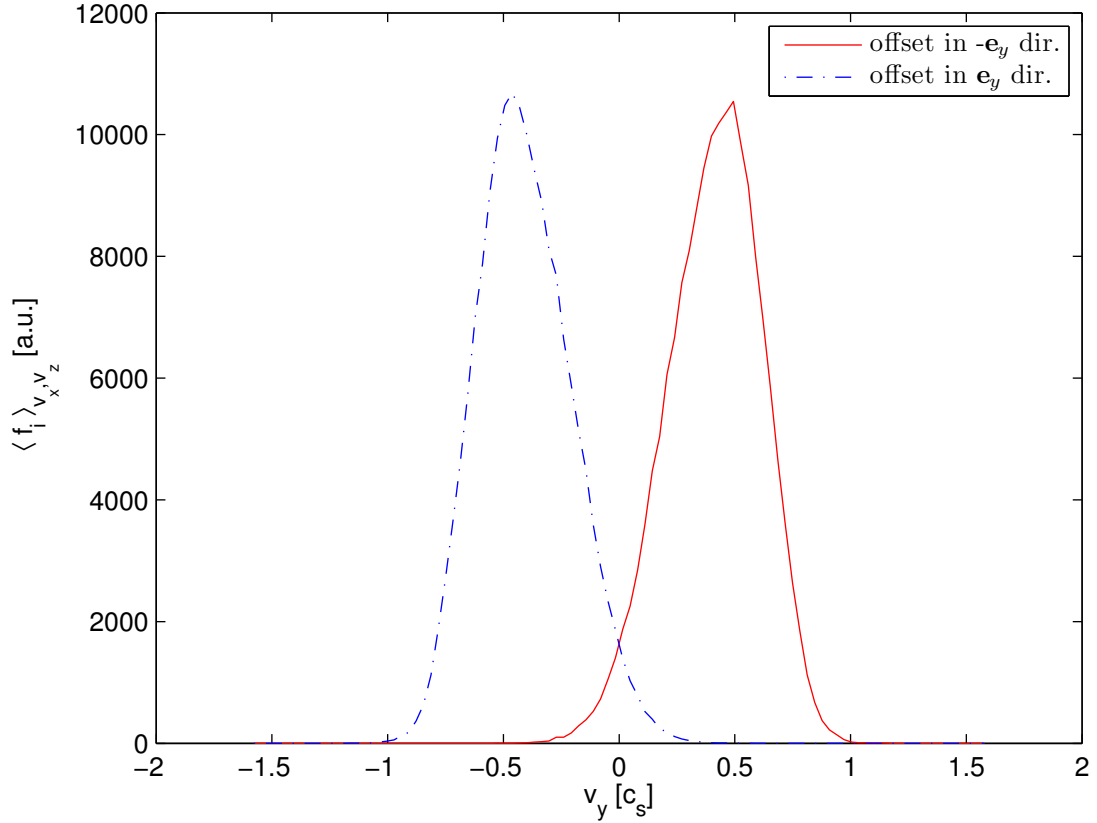


Figure 3-1: Distribution of v_y velocity components in the cells of the Cartesian grid closest to but not intersecting the sphere, offset from the center along the y -axis. There is a strong inward radial drift of $\sim 0.5 c_s$, and the distributions at the two points are in good agreement (should match if one is plotted against $-v_y$).

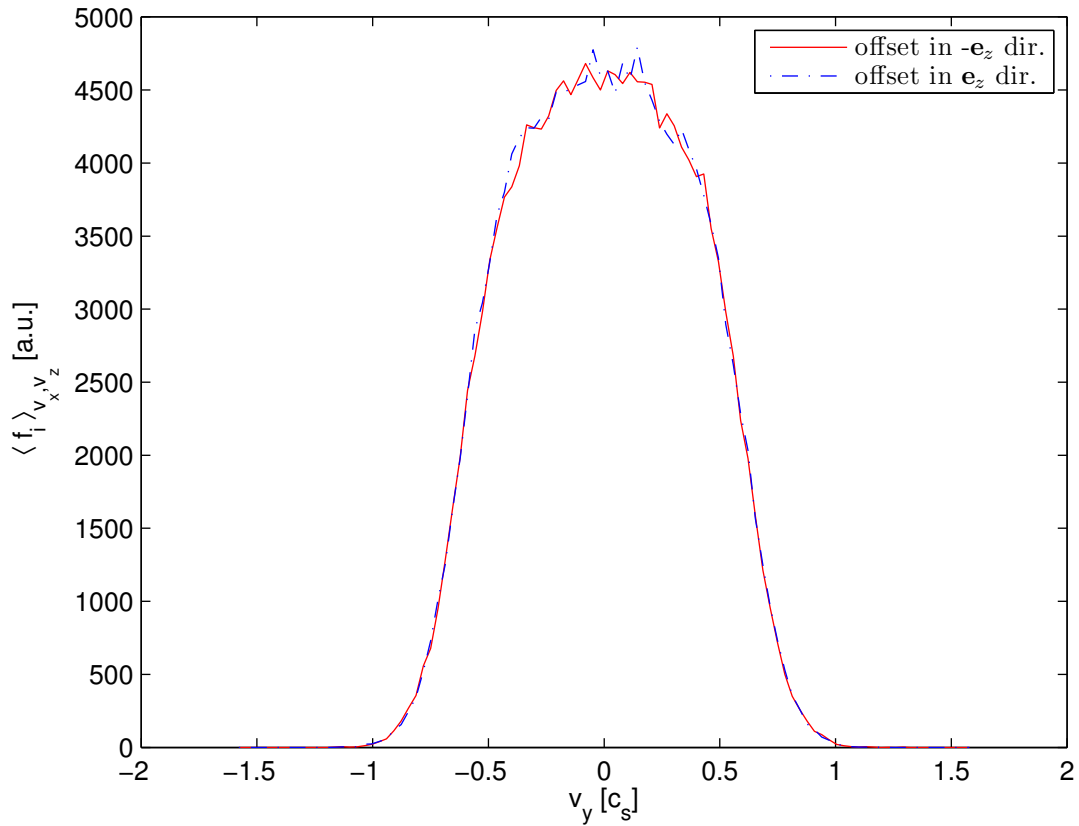


Figure 3-2: Distribution of v_y velocity components in the cells of the Cartesian grid closest to but not intersecting the sphere, offset from the center along the z -axis. The distributions have been significantly broadened from their initial Maxwellian forms, and now have a FWHM of $\sim c_s$. As they should be, the two distributions are in good agreement.

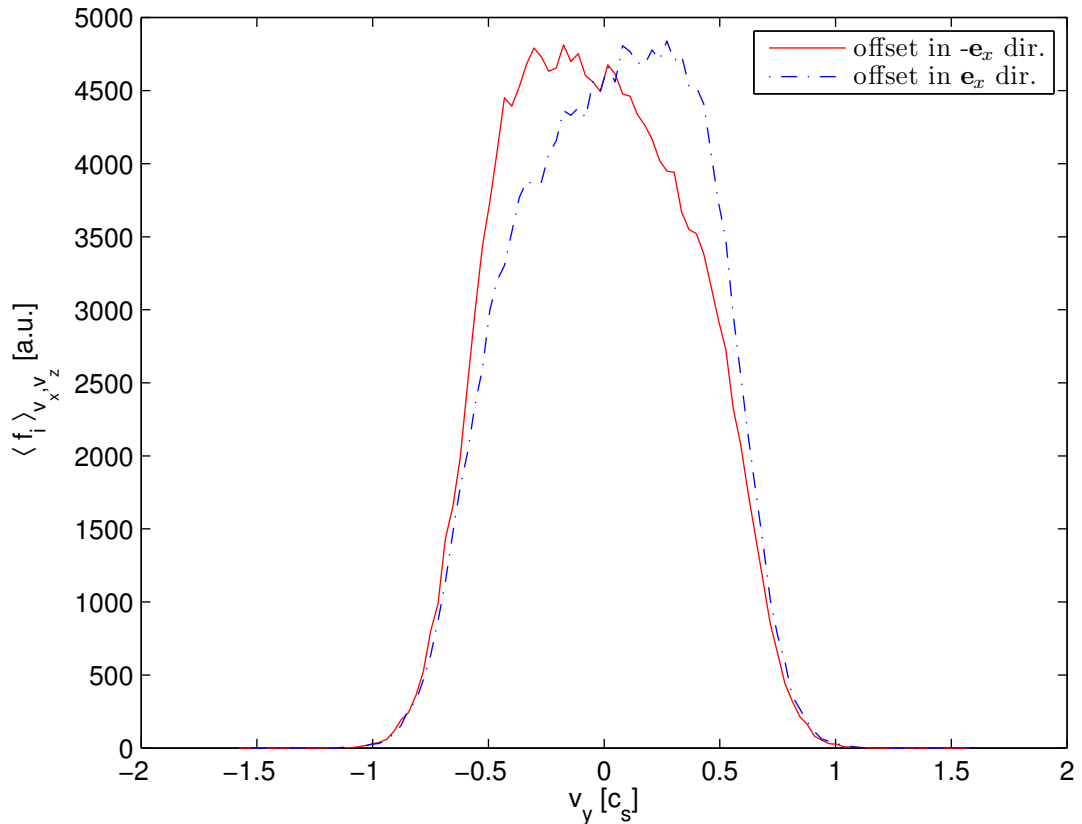


Figure 3-3: Distribution of v_y velocity components in the cells of the Cartesian grid closest to but not intersecting the sphere, offset from the center along the x -axis. The distributions at these locations are broadened similarly to those in fig. 3-2, but have an additional asymmetry giving a drift in the $\mp\mathbf{e}_y$ direction. Again the distributions are in good agreement if one is plotted against $-v_y$.

and the temperature

$$T_{iy} = \int_{-\infty}^{\infty} v_y^2 \langle f_i \rangle_{v_x, v_z} dv_y \quad (3.3)$$

in a given direction (\mathbf{e}_y here). Their spatial dependence can then easily be examined, and the noise on these quantities is significantly less than on the measured distribution functions. It is thus interesting to see what sort of features show up when examining the moments of the SCEPTIC3D computed distributions, so that these can be compared qualitatively and quantitatively to experimental results.

Figure 3-4 shows the two moments for an $x-y$ planar cut of cells of the Cartesian grid as close to but not intersecting the probe as possible (offset in the \mathbf{e}_z direction). Since the problem considered is symmetric about the z -axis the distributions in the \mathbf{e}_x directions are identical to those in the \mathbf{e}_y direction. Adding the two drift moments and averaging the temperatures recovers this symmetry, as shown in fig. 3-5. The dominant drift in the two figures is the projection onto the plane of the inward radial drift. Moving in from the edge of the figures the radial drift increases (as does its projection) because the distance to the probe is decreasing. However, as the point $(x, y) = (0, 0)$ is approached the projection of the radial drift vanishes because the radial direction becomes perpendicular to the plane, even though the radial drift is largest there. The counter-clockwise drift is due to the previously discussed $\mathbf{E} \times \mathbf{B}$ -like drift, and displays a similar behavior when moving from the edge towards $(0, 0)$ since the projection of the radial electric field behaves similarly to the projection of the radial drift. The increase in the temperature towards the point $(0, 0)$ seen in the figures is capturing the broadening of the distribution function due to angular momentum conservation.

3.2 Modifications to the Poisson Solver

When applying SCEPTIC3D to problems with large domains and low ion temperature, it was discovered that the original Poisson solver occasionally failed and corrupted the potential solution. The original solver was based on the minimum residual method, which assumes that the sparse matrix is symmetric. However, the matrix

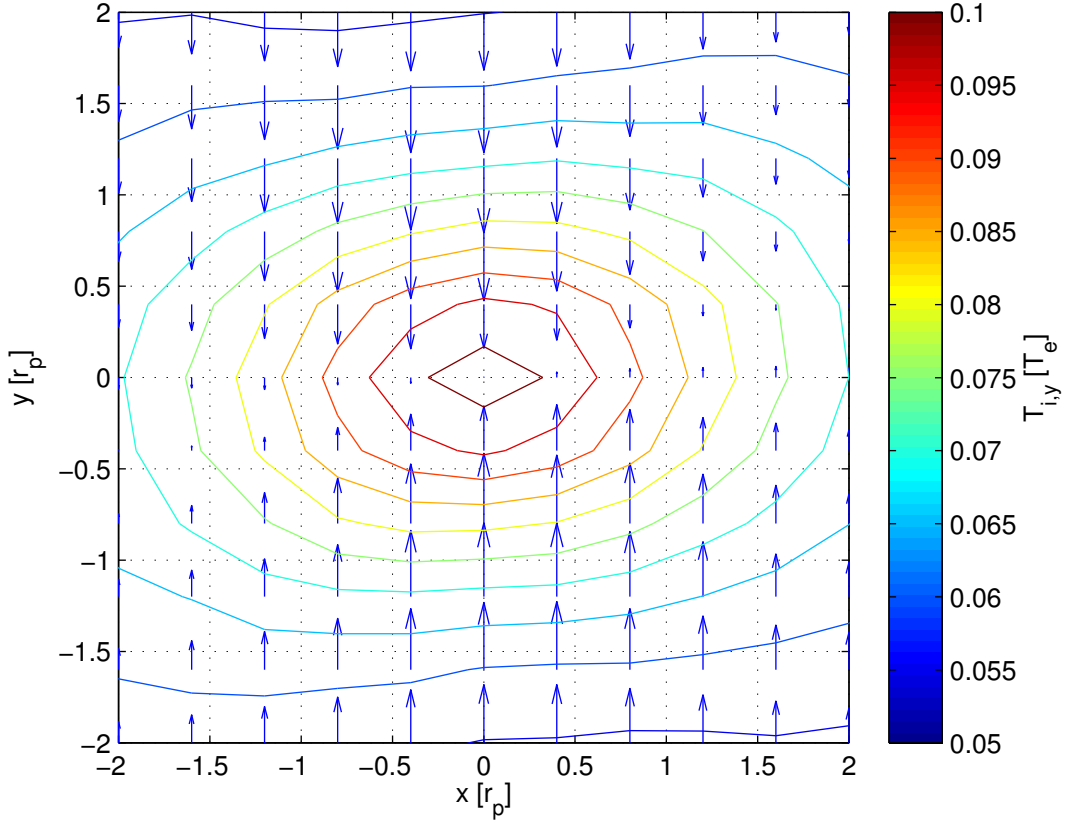


Figure 3-4: Average drift $\bar{v}_y \mathbf{e}_y$ (blue arrows in a.u.) and temperature $T_{i,y}$ (contours) of $\langle f_i \rangle_{v_x, v_z}$, shown for an $x-y$ planar cut of cells of the Cartesian grid as close to but not intersecting the probe as possible (offset in the \mathbf{e}_z direction). The projection of the radial velocity onto the plane can be seen to increase towards $x = 0$, while it first increases and then decreases when moving from the edge towards towards $y = 0$. The temperature increases from the unperturbed value at the top and bottom to twice that value near $(x, y) = (0, 0)$. Along $y = 0$ a slight counter-clockwise drift can be seen.

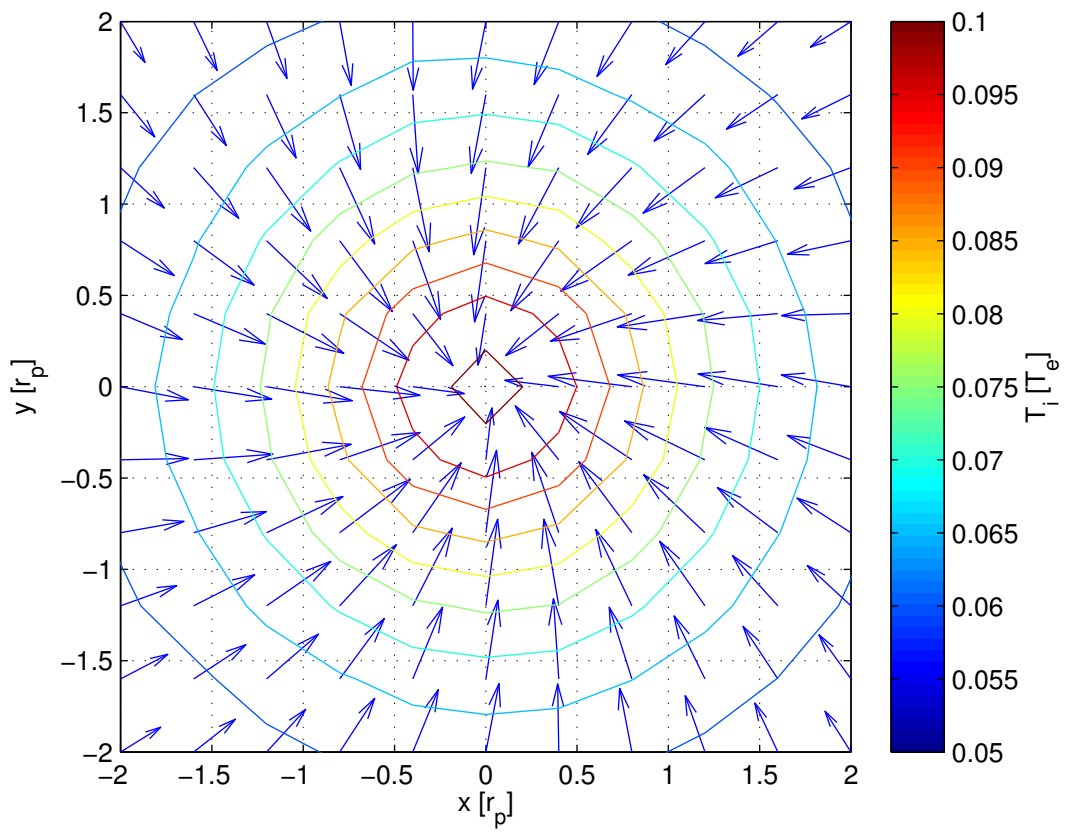


Figure 3-5: Total average drift $\bar{v}_y \mathbf{e}_y + \bar{v}_x \mathbf{e}_x$ (blue arrows in a.u.) and temperature $T_i = (T_{iy} + T_{ix})/2$ (contours), shown for the same locations as in fig. 3-4. The slight counter-clockwise drift is now clear, and the temperature contours are circular.

set up in ref. [19] is not quite symmetric, and so this was identified as the likely cause of the solver failing. Thus, the solver was modified to use the biconjugate gradient method, which allows for asymmetric matrices, but requires the ability to multiply by the transpose matrix.

3.2.1 Finite Volume Matrix

The finite volume discretization of the Poisson equation for SCEPTIC3D is described in section III.3.1 of ref. [19]. For completeness, and to correct a few sign errors, parts of that development are repeated and expanded upon here.

The unknown potential ϕ is assumed to be close to the potential ϕ^* at the previous time-step, allowing the exponential in the source term due to the Boltzmann electrons to be linearized. The Poisson equation thus becomes

$$\nabla^2 \phi = \frac{\exp(\phi^*) [1 + (\phi - \phi^*)] - n}{\lambda_{De}^2}, \quad (3.4)$$

where n is the ion density and λ_{De} is the electron Debye length.

Treating eq. 3.4 as a conservation relation for $-\nabla\phi$ allows the application of finite volume methods to discretize it. The equation is volume-integrated over each cell to give

$$\int_{Cell\ boundary} \nabla\phi \cdot d\mathbf{S} = \frac{1}{\lambda_{De}^2} \int_{Cell} \{\exp(\phi^*) [1 + (\phi - \phi^*)] - n\} d\Omega, \quad (3.5)$$

where $d\mathbf{S}$ is an infinitesimal surface area element taken with outward normal, $d\Omega$ is an infinitesimal volume element, and the divergence theorem has been applied to the left hand side.

Labeling the cell center coordinates r_i , $\cos\theta_j$, and ψ_k , for $i \in [2 : n_r - 1]$, $j \in [2 : n_\theta - 1]$, and $k \in [1 : n_\psi]$, the integral on the right hand side of eq. 3.5 can be approximated as

$$Q_{i,j,k} = - \left\{ \exp(\phi_{i,j,k}^*) [1 + (\phi_{i,j,k} - \phi_{i,j,k}^*)] - n_{i,j,k} \right\} r_{i,j,k}^2 \Delta r \Delta \cos\theta \Delta\psi \quad (3.6)$$

where $\Delta \cos\theta$ is taken to be negative, i.e. $\cos\theta_{j+1} < \cos\theta_j$ since $\theta_{j+1} > \theta_j$.

The left hand side of eq. 3.5 can also be discretized under the assumption that $\nabla\phi$ is constant on the six cell boundaries:

$$\begin{aligned} \int_{i,j,k} \nabla\phi \cdot d\mathbf{S} = & - \left(\frac{\partial\phi}{\partial r} \Big|_{i+1/2,j,k} r_{i+1/2}^2 - \frac{\partial\phi}{\partial r} \Big|_{i-1/2,j,k} r_{i-1/2}^2 \right) \Delta \cos\theta \Delta\psi \\ & + \frac{1}{r_i} \left(\frac{\partial\phi}{\partial\theta} \Big|_{i,j+1/2,k} \sin\theta_{j+1/2} - \frac{\partial\phi}{\partial\theta} \Big|_{i,j-1/2,k} \sin\theta_{j-1/2} \right) r_i \Delta r \Delta\psi \\ & + \frac{1}{r_i \sin\theta_j} \left(\frac{\partial\phi}{\partial\psi} \Big|_{i,j,k+1/2} - \frac{\partial\phi}{\partial\psi} \Big|_{i,j,k-1/2} \right) r_i \Delta r \Delta\theta_j. \end{aligned} \quad (3.7)$$

The derivatives can be approximated with finite differences, so together with the approximation $\Delta \cos\theta = -\sin\theta \Delta\theta$ the expression can be rewritten as

$$\begin{aligned} \int_{i,j,k} \nabla\phi \cdot d\mathbf{S} = & - \left(\frac{\phi_{i+1,j,k} - \phi_{i,j,k}}{\Delta r} r_{i+1/2}^2 - \frac{\phi_{i,j,k} - \phi_{i-1,j,k}}{\Delta r} r_{i-1/2}^2 \right) \Delta \cos\theta \Delta\psi \\ & - \left(\frac{\phi_{i,j+1,k} - \phi_{i,j,k}}{\Delta \cos\theta} \sin^2\theta_{j+1/2} - \frac{\phi_{i,j,k} - \phi_{i,j-1,k}}{\Delta \cos\theta} \sin^2\theta_{j-1/2} \right) \Delta r \Delta\psi \\ & - \frac{1}{\sin^2\theta_j} \left(\frac{\phi_{i,j,k+1} - \phi_{i,j,k}}{\Delta\psi} - \frac{\phi_{i,j,k} - \phi_{i,j,k-1}}{\Delta\psi} \right) \Delta r \Delta\cos\theta. \end{aligned} \quad (3.8)$$

Combining the derived discrete forms of the integrals with eq. 3.5, and dividing by $-r_i^2 \Delta r \Delta \cos\theta \Delta\psi / \lambda_{De}$, allows the equation to be written in the matrix form $\mathbf{A}\phi + \omega = \sigma$, where \mathbf{A} has contributions from the differential operator, the linearized implicit electron response, and the Neumann part of the outer boundary condition, ω carries the Dirichlet part of the boundary conditions, and

$$\sigma_{i,j,k} = \exp(\phi_{i,j,k}^*) [1 - \phi_{i,j,k}^*] - n_{i,j,k} \quad (3.9)$$

is the source term. Gathering terms according to the indices i , j , and k , the product $\mathbf{A}\phi$ can be written as

$$\begin{aligned} (A\phi)_{i,j,k} = & a_i \phi_{i+1,j,k} + b_i \phi_{i-1,j,k} + c_{i,j} \phi_{i,j+1,k} + d_{i,j} \phi_{i,j-1,k} \\ & + e_{i,j} (\phi_{i,j,k+1} + \phi_{i,j,k-1}) - [f_{i,j} + \exp(\phi_{i,j,k}^*)] \phi_{i,j,k}, \end{aligned} \quad (3.10)$$

where

$$\begin{aligned} a_i &= \lambda_{De}^2 \frac{r_{i+1/2}^2}{r_i^2 \Delta r^2}, & b_i &= \lambda_{De}^2 \frac{r_{i-1/2}^2}{r_i^2 \Delta r^2}, \\ c_{i,j} &= \lambda_{De}^2 \frac{\sin^2 \theta_{j+1/2}}{r_i^2 (\Delta \cos \theta)^2}, & d_{i,j} &= \lambda_{De}^2 \frac{\sin^2 \theta_{j-1/2}}{r_i^2 (\Delta \cos \theta)^2}, \\ e_{i,j} &= \lambda_{De}^2 \frac{1}{r_i^2 \sin^2 \theta_j \Delta \psi^2}, & f_{i,j} &= a_i + b_i + c_{i,j} + d_{i,j} + 2e_{i,j}, \end{aligned} \quad (3.11)$$

and the index k is taken to be periodic (i.e. $\phi_{i,j,0} = \phi_{i,j,n_\psi}$ and $\phi_{i,j,n_\psi+1} = \phi_{i,j,1}$). The cells on axis (i.e. with $j = 1$ or $j = n_\theta$) have half the volume, and are treated with the following modifications to the coefficients given in eq. 3.11:

$$\begin{aligned} c_{i,1} &= 2\lambda_{De}^2 \frac{\sin^2 \theta_{1+1/2}}{r_i^2 (\Delta \cos \theta)^2}, & c_{i,n_\theta} &= 0, \\ d_{i,1} &= 0, & d_{i,n_\theta} &= 2\lambda_{De}^2 \frac{\sin^2 \theta_{n_\theta-1/2}}{r_i^2 (\Delta \cos \theta)^2}, \\ e_{i,1} &= \lambda_{De}^2 \frac{1}{r_i^2 \sin^2 \theta_{1+1/4} \Delta \psi^2}, & e_{i,n_\theta} &= \lambda_{De}^2 \frac{1}{r_i^2 \sin^2 \theta_{n_\theta-1/4} \Delta \psi^2}. \end{aligned} \quad (3.12)$$

The inner boundary condition is Dirichlet, with a specified potential at each point (j, k) for $i = 1$. This is implemented by excluding $\phi_{1,j,k}$ from the solution vector (setting it to zero there, and not considering the index $i = 1$), and rather including its contribution to $(A\phi)_{2,j,k}$ through the vector ω :

$$\omega_{2,j,k} = b_2 \phi_{1,j,k}. \quad (3.13)$$

For the outer boundary condition, ghost cells

$$\phi_{n_r+1,j,k} = g_{j,k,1} \phi_{n_r-1,j,k} + g_{j,k,2} \phi_{n_r,j-1,k} + g_{j,k,3} \phi_{n_r,j+1,k} + g_{j,k,5} \phi_{n_r,j,k} \quad (3.14)$$

are used, along with the element

$$\omega_{n_r,j,k} = a_{n_r} g_{j,k,4}, \quad (3.15)$$

such that $(A\phi)_{n_r,j,k}$ can be treated like the remaining elements of $\mathbf{A}\phi$. The coefficients $g_{j,k,o}$ ($o \in [1 : 5]$) depend on the chosen outer boundary condition, which can in general

be Robin. Note however that the present implementation does not allow the outer boundary condition to depend on $\phi_{n_r,j,k\pm 1}$.

3.2.2 Asymmetry of the Finite Volume Matrix

The matrix \mathbf{A} as defined by eq. 3.10 can be expressed (for $i < n_r$) as

$$\begin{aligned} A_{i,j,k;l,m,n} = & a_i \delta_{l,i+1} \delta_{m,j} \delta_{n,k} + b_i \delta_{l,i-1} \delta_{m,j} \delta_{n,k} \\ & + c_{i,j} \delta_{l,i} \delta_{m,j+1} \delta_{n,k} + d_{i,j} \delta_{l,i} \delta_{m,j-1} \delta_{n,k} \\ & + e_{i,j} \delta_{l,i} \delta_{m,j} (\delta_{n,k+1} + \delta_{n,k-1}) \\ & - (f_{i,j} + \exp(\phi_{i,j,k}^*)) \delta_{l,i} \delta_{m,j} \delta_{n,k}, \end{aligned} \quad (3.16)$$

where the Kronecker $\delta_{m,j}$ equals one for $j = m$ and zero otherwise. For $i = n_r$ the expression for the ghost cell from eq. 3.14 must be substituted for $\phi_{n_r+1,j,k}$ in eq. 3.10, giving

$$\begin{aligned} A_{n_r,j,k;l,m,n} = & (b_{n_r} + a_{n_r} g_{j,k,1}) \delta_{l,n_r-1} \delta_{m,j} \delta_{n,k} \\ & + (c_{n_r,j} + a_{n_r} g_{j,k,3}) \delta_{l,n_r} \delta_{m,j+1} \delta_{n,k} + (d_{n_r,j} + a_{n_r} g_{j,k,2}) \delta_{l,n_r} \delta_{m,j-1} \delta_{n,k} \\ & + e_{n_r,j} \delta_{l,n_r} \delta_{m,j} (\delta_{n,k+1} + \delta_{n,k-1}) \\ & - (f_{n_r,j} + \exp(\phi_{n_r,j,k}^*) - a_{n_r} g_{j,k,5}) \delta_{l,n_r} \delta_{m,j} \delta_{n,k}. \end{aligned} \quad (3.17)$$

From these expressions the transpose matrix \mathbf{A}^T can be found using the property $(A^T)_{i,j,k;l,m,n} = A_{l,m,n;i,j,k}$, which gives

$$\begin{aligned} (A^T \phi)_{i,j,k} = & a_{i-1} \phi_{i-1,j,k} + b_{i+1} \phi_{i+1,j,k} + c_{i,j-1} \phi_{i,j-1,k} + d_{i,j+1} \phi_{i,j+1,k} \\ & + e_{i,j} \phi_{i,l} (\phi_{i,j,k-1} + \phi_{i,j,k+1}) - (f_{i,j} + \exp(\phi_{i,j,k}^*)) \phi_{i,j,k} \end{aligned} \quad (3.18)$$

for $i < n_r - 1$,

$$\begin{aligned}
(A^T \phi)_{n_r-1,j,k} = & a_{n_r-2} \phi_{n_r-2,j,k} + (b_{n_r} + a_{n_r,j,k} g_{j,k,1}) \phi_{n_r,j,k} \\
& + c_{n_r-1,j-1} \phi_{n_r-1,j-1,k} + d_{n_r-1,j+1} \phi_{n_r-1,j+1,k} \\
& + e_{n_r-1,j} \phi_{n_r-1,l} (\phi_{n_r-1,j,k-1} + \phi_{n_r-1,j,k+1}) \\
& - (f_{n_r-1,j} + \exp(\phi_{n_r-1,j,k}^*)) \phi_{n_r-1,j,k}
\end{aligned} \tag{3.19}$$

for $i = n_r - 1$, and

$$\begin{aligned}
(A^T \phi)_{n_r,j,k} = & a_{n_r-1} \phi_{n_r-1,j,k} \\
& + (c_{n_r,j-1} + a_{n_r} g_{j-1,k,3}) \phi_{n_r,j-1,k} + (d_{n_r,j+1} + a_{n_r} g_{j+1,k,2}) \phi_{n_r,j+1,k} \\
& + e_{n_r,j} \phi_{n_r,l} (\phi_{n_r,j,k-1} + \phi_{n_r,j,k+1}) \\
& - (f_{n_r,j} + \exp(\phi_{n_r,j,k}^*) - a_{n_r} g_{j,k,5}) \phi_{n_r,j,k}
\end{aligned} \tag{3.20}$$

for $i = n_r$. For arbitrary $g_{j,k,o}$ it is clear that \mathbf{A} is in general not symmetric, as can be seen for instance from the fact that $(A^T \phi)_{n_r-1,j,k}$ depends on $g_{j,k,1}$, while $(A \phi)_{n_r-1,j,k}$ does not.

For elements of $\mathbf{A} - \mathbf{A}^T$ that are unaffected by the boundary conditions, the difference is

$$\begin{aligned}
(A - A^T)_{i,j,k;l,m,n} = & (a_i \delta_{l,i+1} - a_l \delta_{i,l+1}) \delta_{m,j} \delta_{n,k} \\
& + (b_i \delta_{l,i-1} - b_l \delta_{i,l-1}) \delta_{m,j} \delta_{n,k} \\
& + \delta_{l,i} (c_{i,j} \delta_{m,j+1} - c_{l,m} \delta_{j,m+1}) \delta_{n,k} \\
& + \delta_{l,i} (d_{i,j} \delta_{m,j-1} - d_{l,m} \delta_{j,m-1}) \delta_{n,k},
\end{aligned} \tag{3.21}$$

where the terms involving the e and f coefficients cancel exactly and are thus not

present. This can be rewritten as

$$(A - A^T)_{i,j,k;l,m,n} = [(a_i - b_{i+1})\delta_{l,i+1} - (a_{i-1} - b_i)\delta_{l,i-1}] \delta_{m,j}\delta_{n,k} \\ + \delta_{l,i} [(c_{i,j} - d_{i,j+1})\delta_{m,j+1} - (c_{i,j-1} - d_{i,j})\delta_{m,j-1}] \delta_{n,k}, \quad (3.22)$$

where the coefficient differences evaluate to

$$a_i - b_{i+1} = \lambda_{De}^2 \frac{r_{i+1/2}^2}{\Delta r^2} \left(\frac{1}{r_i^2} - \frac{1}{r_{i+1}^2} \right), \quad (3.23)$$

$$a_{i-1} - b_i = \lambda_{De}^2 \frac{r_{i-1/2}^2}{\Delta r^2} \left(\frac{1}{r_{i-1}^2} - \frac{1}{r_i^2} \right), \quad (3.24)$$

$$c_{i,j} - d_{i,j+1} = \begin{cases} \lambda_{De}^2 \frac{\sin^2 \theta_{i+1/2}}{r_i^2 (\Delta \cos \theta)^2}, & j = 1, \\ 0, & 1 < j < n_\theta, \end{cases} \quad (3.25)$$

and

$$c_{i,j-1} - d_{i,j} = \begin{cases} 0, & 1 < j < n_\theta, \\ \lambda_{De}^2 \frac{\sin^2 \theta_{n_\theta-1/2}}{r_i^2 (\Delta \cos \theta)^2}, & j = n_\theta. \end{cases} \quad (3.26)$$

The asymmetry due to the differences $a_i - b_{i+1}$ and $a_{i-1} - b_i$ could in principle be eliminated by multiplying the discrete form of eq. 3.5 by r_i^2 before defining the coefficients, but this would not take care of the other asymmetries, and is not presently done in the modified Poisson solver.

3.2.3 Biconjugate Gradient Method

The biconjugate gradient method [32] is closely related to the minimum residual method, but does not require the matrix \mathbf{A} to be symmetric. It does however require the ability to multiply by \mathbf{A}^T , so implementing it requires using equations 3.18-3.20 to create a function for returning the product $\mathbf{A}^T \phi$.

SCEPTIC3D has been modified to use the (Jacobi) preconditioned¹ biconjugate

¹Jacobi preconditioning entails multiplying the matrix equation to be solved by the inverse of the diagonal entries of \mathbf{A} , and helps speed the convergence of iterative solution techniques.

gradient method, both for the serial and parallel versions of its Poisson solver. The code is based on the original minimum residual based solver, which was adapted for Fortran from a C++ routine in ref. [32]. As such, the solver uses single precision floating arithmetic throughout, and may be susceptible to breakdown or convergence issues for large systems due to rounding error. If this becomes an issue in the future, a possible strategy to overcome it is to switch to double precision for the calculations in the iterative procedure, but to then cast the potential to a floating point version to not compromise the speed of the particle moving step. Since the solution to the Poisson equation is a small fraction of the overall cost of running SCEPTIC3D, this approach should not have significant impact on the total run time (though storage and communication burdens do increase).

The convergence criterion used for the biconjugate gradient based solver is the same as that which was used with the minimum residual method: $\Delta\phi = 10^{-5}T_e/e$, where the change in ϕ is taken from one iteration of the biconjugate gradient method to the next. Provided the change from one iteration to the next is representative of the distance to the converged solution (which is not guaranteed for the biconjugate gradient method), that level of convergence should be sufficient for the particle moving done in SCEPTIC3D. For many cells the error on the potential due to particle noise will be greater than the convergence error, so provided it is not a systematic effect the convergence error is unlikely to be more important than the particle noise. Further, since the particle energies are typically much larger than the potential error, the overall effect on the particle dynamics is expected to be small.

The parallel version of the solver can be set to only check for convergence after taking 80% of the number of iterations required for convergence at the previous time-step, and then only at each fifth iteration thereafter. Doing so should give some speed-up over doing a reduce across nodes and checking for convergence at each iteration, but provided the Poisson solver takes up a small fraction of the overall computation time the gain may be minimal. In fact, there may be a net cost since a single time-step which for some reason requires many iterations for convergence will force subsequent time-steps to also use many iterations, regardless of whether they

are all required for convergence. The default mode of operation for the parallel solver is thus to check for convergence at every iteration.

3.2.4 Parallel Version of the Poisson Solver

As described in ref. [19] the particle moving step in SCEPTIC3D is parallelized by assigning a fixed number of computational ions to each node, without domain decomposition or other attempts at ensuring data-locality. This removes the need for load-balancing, passing particles, and other implementation complications associated with domain decomposition, but will ultimately limit the parallel scalability of SCEPTIC3D. However, for the problems presently considered (using <512 cores) large parts of the potential array typically fit in the available processor cache, limiting the gain that could be achieved from better data locality.

The parallelization of the Poisson solver is not described in ref. [19] beyond stating that the multiplication by the matrix \mathbf{A} is an easily parallelizable step. Some details are therefore given here to clarify what went into upgrading to the biconjugate gradient method for the parallel solver, as well as discussion of some limitations of the present approach.

The routines from ref. [32] which were the starting point for both the minimum residual and biconjugate gradient based solvers are serial routines. They solve the problem $\mathbf{Ax} = \mathbf{b}$ iteratively, with each iteration relying on a number of matrix–vector products and vector additions and inner products. Parallelizing the solver thus requires parallelizing each of those operations, which as alluded to in ref. [19] is not especially difficult.

A natural way to parallelize operations on vectors is to make each node responsible for certain elements of each vector. The grid on which the potential is computed is three dimensional, and the elements of the solution vector can couple directly to neighboring elements in each of the three dimensions, so to minimize the dependence on values held by other nodes the vectors should be partitioned according to those three dimensions such that the elements held by a node corresponds to a block of the actual 3D grid. Further, the partitioning should be chosen such that the blocks

have a small surface area to volume ratio (in terms of the number of elements). This partitioning is presently done heuristically in SCEPTIC3D, requiring at least two blocks in each dimension (for a minimum of eight blocks/nodes). For runs with fewer than eight nodes the serial solver should be used (particle moving is still parallelized when running the parallel version of SCEPTIC3D without the parallel solver `--sp` option). Also note that total number of nodes may not be conducive to a practical division of three separate dimension (e.g. if it is prime), so not all the particle moving nodes are necessarily used for the parallel solver.

With each node responsible for the elements of each vector corresponding to a block of the grid, vector additions are trivially parallelized by each node operating on its own elements of the vectors, and inner products can be performed separately for each block, with only the local sum having to be communicated from each node for a reduction sum to find the total inner product. A matrix–vector product could in principle have an element of the resulting vector \mathbf{Ar} depend on any element of a vector \mathbf{r} , but the particular structure of the matrix \mathbf{A} due to the finite volume stencil used in SCEPTIC3D only introduces a dependence on the adjacent elements of \mathbf{r} in each of the three dimensions. Thus, it suffices to communicate only the values immediately outside the surface of the block of the grid held by each node before each matrix–vector product is computed. Provided this is done, each node then has the values it needs to compute its elements of the vector resulting from the product, so the matrix–vector products are also parallelized with minimal communication.

Since the particle moving done by each node is not localized to the block of the potential grid on which it computed the potential, each node must obtain a copy of the entire potential through a broadcast after the solution has been found by the solver. This does not presently appear to be a significant communication cost, but could limit scaling to larger problems in the future.

3.2.5 Verification of the Upgraded Solver

To verify that the transpose matrix multiplication is calculated correctly in both the serial and parallel versions of the solver, and that the biconjugate gradient based

solver is converging to the right solution, new debugging outputs have been added to SCEPTIC3D. The idea is to store dense versions of the matrix \mathbf{A} and its transpose (for very coarse grids), as well as the right hand side \mathbf{y} and the solution vector ϕ , and then inspect the matrices and check the solution to $\mathbf{A}\phi = \mathbf{y}$ using MATLAB.

A dense version of the matrix \mathbf{A} is generated by successively setting each element of an otherwise zero vector \mathbf{r} to the value one, and storing the entire output vector \mathbf{Ar} as the corresponding column of \mathbf{A} . This process scales like $n_r^2 n_\theta^2 n_\psi^2$ both in storage and computation, and can therefore only be done for very coarse grids. It is activated by passing the `--savemat` option to SCEPTIC3D, but is only typically useful for verifying that the solver still works correctly if it has been modified.

The structure of the matrix \mathbf{A} for $n_r = n_\theta = n_\psi = 6$ is shown in fig. 3-6. The radial size of the domain is taken to be $r_d = 60 r_p$, and the electron Debye length to be $\lambda_{De} = 20 r_p$. Since problems with such a coarse grid have little physical relevance, and since the only purpose of this SCEPTIC3D run is to examine the functioning of the solver, only a few time-steps are taken. The charge-distribution is thus not consistent with a steady-state solution, but nonetheless provides a valid source term for the Poisson equation. Long Debye lengths and grids with large Δr are among the most challenging problems for the Poisson solver, so this represents one type of worst-case scenario for the solver.

Figure 3-6 shows explicitly the previously discussed fact that elements of the product \mathbf{Ar} only depend on the adjacent elements in each of the three dimensions. The asymmetry of \mathbf{A} only manifests itself here through a sign difference for one element of each row corresponding to $i = n_r$, but examining the actual values reveals asymmetries where expected based on the discussion in sec. 3.2.2. Note that as previously mentioned the elements $r_{1,j,k}$ are set to zero and not considered in the vector \mathbf{Ar} , so as can be seen in the figure the rows corresponding to $i = 1$ have all zero elements. Further, the elements in columns corresponding to $i = 1$ but rows corresponding to $i = 2$ always multiply zeros in the vector \mathbf{r} , and do therefore not really make \mathbf{A} asymmetric (though it may look that way in the figure).

The transpose matrix \mathbf{A}^T is generated and stored in the same way as \mathbf{A} , but

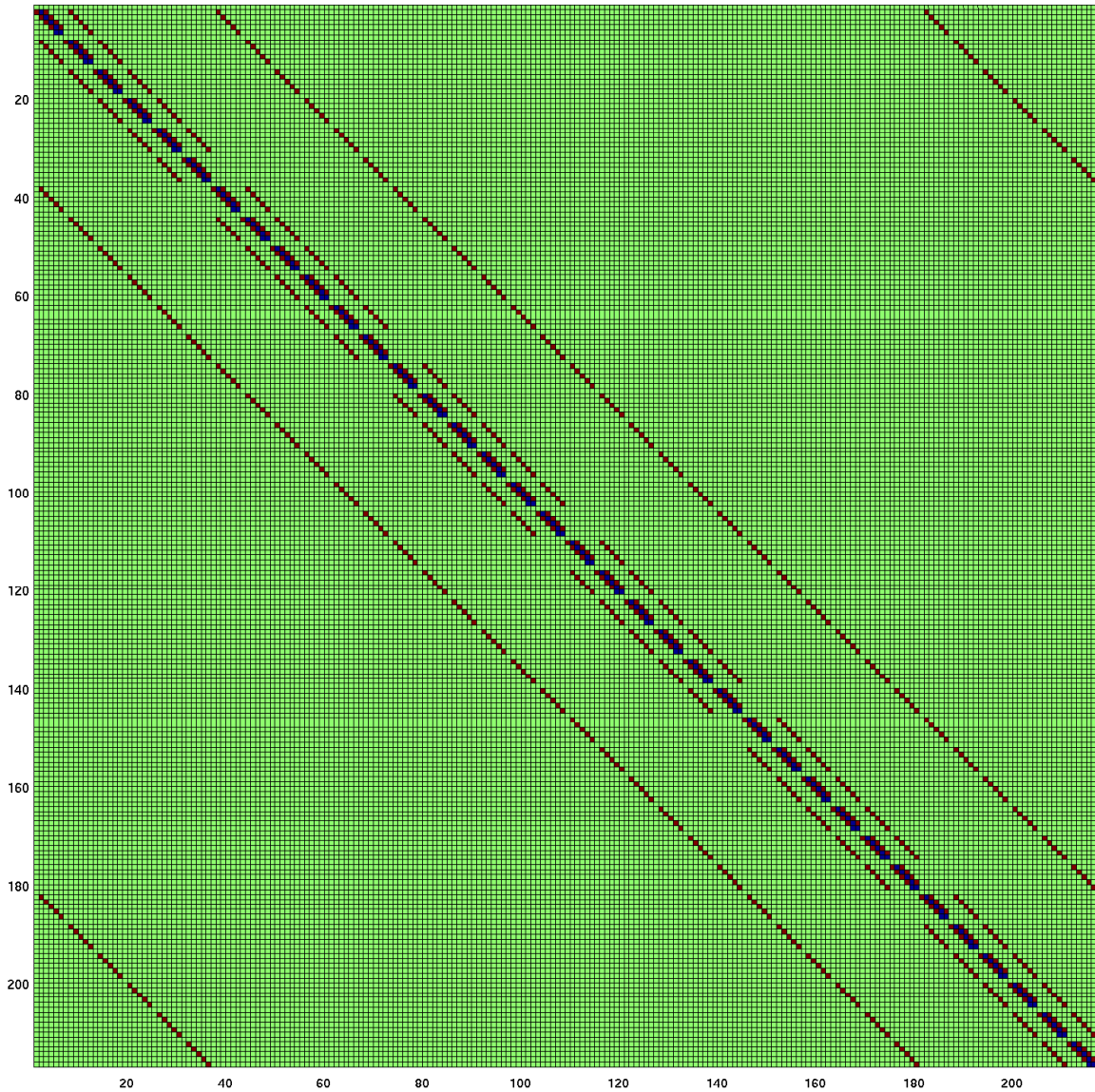


Figure 3-6: Structure of the matrix \mathbf{A} for $n_r = n_\theta = n_\psi = 6$, where negative elements are shown in blue, zero elements in green, and positive elements in red. The counter i varies most rapidly (i increases when going down and to the right in the figure), so the elements adjacent to the diagonal give the coupling in the r variable, while the next set of non-zero elements going away from the diagonal gives the θ coupling, and the final set the ψ coupling (including the periodicity through the elements in the bottom left and top right corners).

with the newly implemented transpose flag passed to the function that returns the matrix–vector product. That the transpose is computed correctly can then be verified by comparing the output \mathbf{A}^T with that computed by transposing \mathbf{A} in MATLAB. This has been done for both the serial and parallel versions of the matrix–vector multiplication routine, and both appear to compute the transpose matrix correctly. Storing the matrices in the parallel case does take some care to ensure that the communication is done correctly, but is done using the same machinery as the actual solution to ensure that any bugs there would also show up when examining the matrix.

Figure 3-7 shows the solution ϕ to the problem $\mathbf{A}\phi = \mathbf{y}$ as computed by the biconjugate gradient based solver in SCEPTIC3D, as well as the difference between it and the exact solution as computed by MATLAB. The solver in SCEPTIC3D appears to be computing a good approximation to the exact solution, with errors that for all elements are well below the convergence threshold of $10^{-5} T_e/e$. Note however that this is for a specific case, and does not guarantee that the solution is as accurate for instance when dealing with solutions that are not spherically symmetric, but does provide a good indication that the upgraded solver is working correctly. The solver took 19 iterations to reach convergence for the solution shown in the figure.

For comparison, the same problem was run using the old minimum residual based solver in SCEPTIC3D (accessible through the `--minres` option). The results are presented in fig. 3-8, and show that the old solver was only able to get to within $\sim 0.1 T_e/e$ of the exact solution, i.e. much worse than the convergence criterion. What happened in this case is that the solver reached the maximum number of iterations (216 for the given grid size), and therefore stopped iterating despite not having reached convergence. It should be pointed out that this problem was selected precisely to exaggerate the asymmetry of the matrix \mathbf{A} , and thus the weaknesses of the minimum residual method, so these results are not typical of the performance of the old solver (which appeared to work satisfactorily for most problems). It does however demonstrate that the upgraded solver is able to handle problems that the old solver could not, and the general impression is that the upgraded solver reaches convergence more quickly and is less susceptible to breakdown than the old solver.

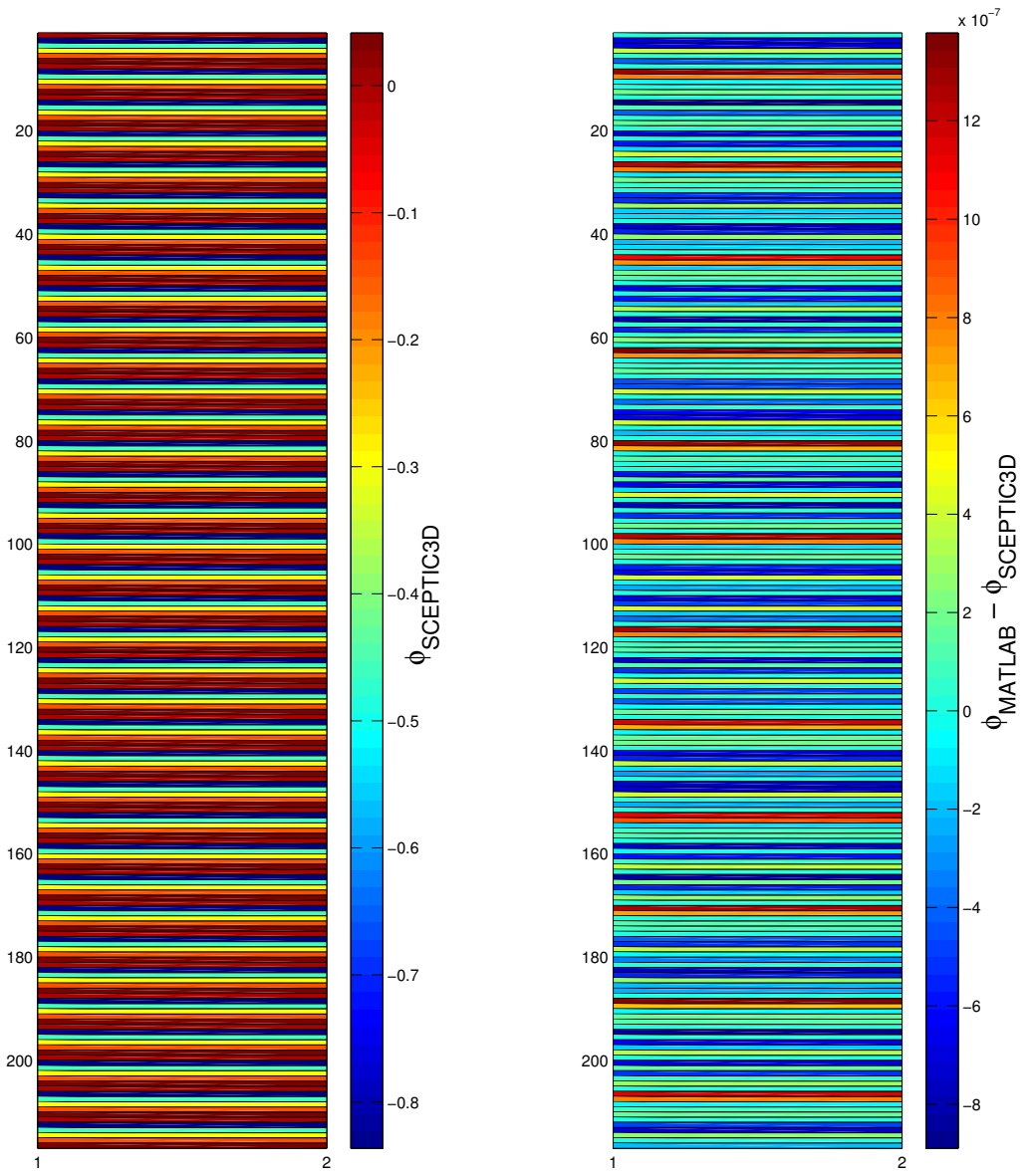


Figure 3-7: Solution to $\mathbf{A}\phi = \mathbf{y}$ from the biconjugate gradient based solver in SCEPTIC3D (left, in units of T_e/e), and the difference between that solution and the exact solution computed with MATLAB (right). Note that the elements $\phi_{1,j,k}$ are set to zero as previously discussed, since the values there are imposed by the Dirichlet boundary condition. The difference between the solution from SCEPTIC3D and that from MATLAB is $\sim 10^{-6} T_e/e$ or below for all elements.

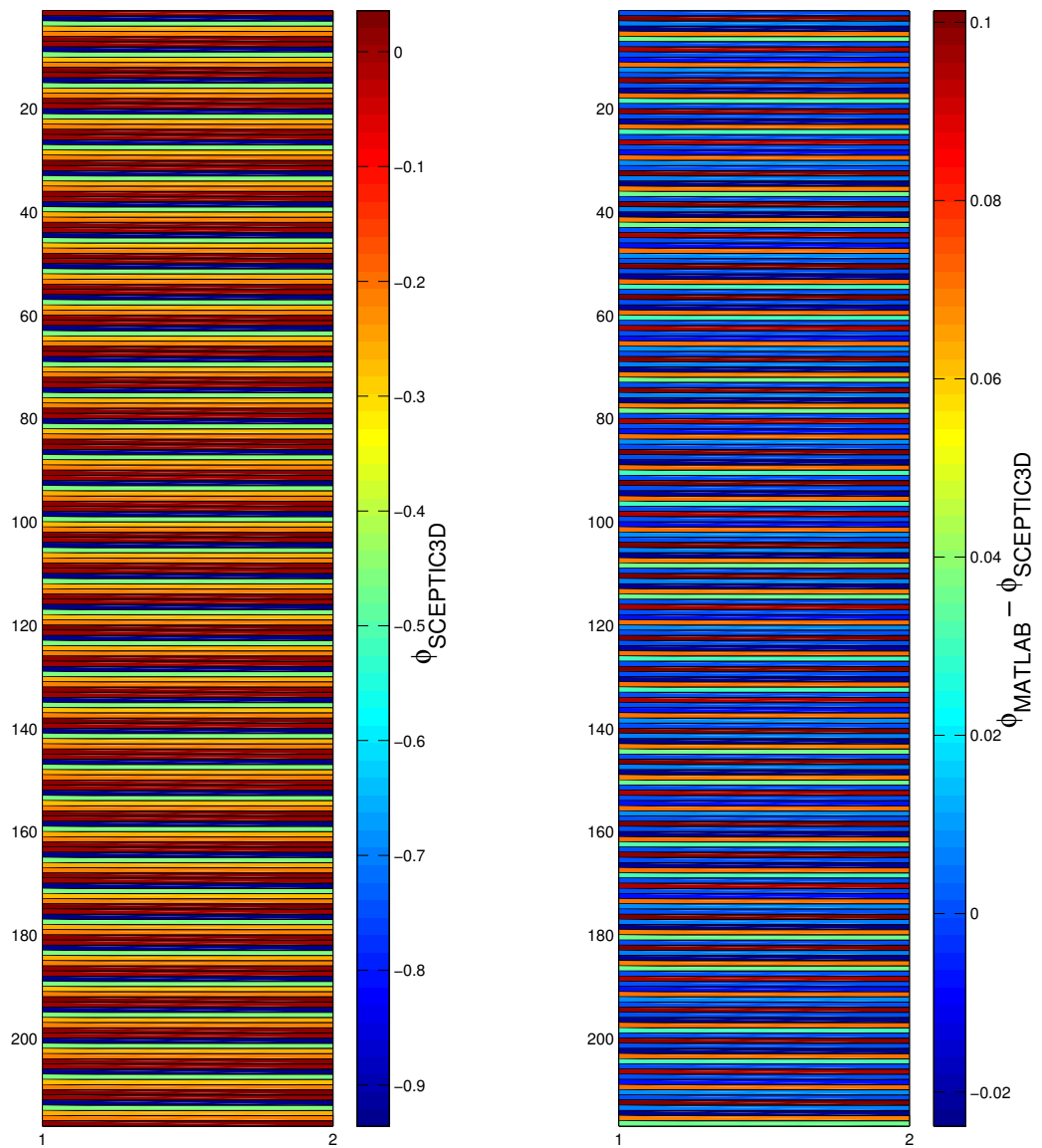


Figure 3-8: Same as fig. 3-7, but using the old minimum residual based solver in SCEPTIC3D. The difference between the solution from SCEPTIC3D and that from MATLAB is in this case as large as $\sim 10^{-1} T_e/e$ for some elements.

3.2.6 Nonlinear Solution to the Poisson Equation

The default approach to solving the Poisson equation in SCEPTIC3D is to assume that the potential varies little from one time-step to the next, such that the exponential dependence on the potential in the Boltzmann electron source term can be linearized around the potential at the previous step. This gives the linearized Poisson equation given in eq. 3.4, which can then be solved with the biconjugate gradient method. However, the PIC method is based on the assumption that the full Poisson equation is solved correctly at each time-step, so this approach is only really self-consistent in the limit where the potential does not change from one time-step to the next. Therefore, to enable verification that the use of the linear equation does not adversely affect the solution, an option to perform a nonlinear loop of biconjugate gradient solutions to the linear problem has been added.

Rather than require each linear solve to iterate until the $\Delta\phi = 10^{-5} T_e/e$ convergence criterion is reached, the convergence criterion for each linear step is tightened towards that limit as the nonlinear loop progresses. The nonlinear loop continues until the $\Delta\phi = 10^{-5} T_e/e$ criterion holds both when comparing the potentials of two different steps of the nonlinear loop, and when comparing the potentials of the two last iterations of the last linear solve.

No detailed comparison of SCEPTIC3D results using the linear and nonlinear solvers has been performed at present, but the initial impression is that the nonlinear solve does not require a much larger total number of linear iterations, nor does it appear to noticeably affect the overall results. This suggests that the approach of just using the linear solver at each time-step is probably adequate for the present applications, though that assertion may (if desired) be verified for specific problems in the future by running the problem both with and without the nonlinear solver activated.

3.3 HDF5 Output

The original output system of SCEPTIC3D is based on ASCII output of arrays to a single text file, coupled with a custom-written MATLAB script to parse and load the data from the output file. This approach requires simultaneous development of both the output routines and the MATLAB script, and generates large files even when storing low-precision data (an ASCII character is used for each digit of precision). Further, loading and parsing the data file becomes slow when large multidimensional arrays are included, so in order to allow quick access to only the smaller datasets they must be grouped at the beginning of the file. Doing so restricts the options for backwards-compatibility of the MATLAB script and data files, thus further complicating the maintenance of the output system and associated plotting scripts. For these reasons, the existing output system was deemed inappropriate for the data-intensive outputs associated with the various new diagnostics being added to SCEPTIC3D (e.g. those described in sections 2.3, 3.1, and 3.2.5), and so a new output system based on the Hierarchical Data Format² version 5 (HDF5) has been developed.

HDF5 is a versatile and powerful format for storing large and/or complex data sets, and the source code is freely available for download. It was chosen both because it does not share any of the discussed shortcomings of the ASCII output system, and because it offers advanced features, such as parallel I/O and complex datasets, that may be useful in future development of SCEPTIC3D.

The approach taken to the new output system is to store the contents of every common block to an HDF5 file at the end of the SCEPTIC3D program. HDF5 allows named groups of datasets in a file, so each Fortran common block has an associated identically named group in the HDF5 file, and then each variable and array in that common block is a dataset in the corresponding group. In addition, a few variables that are not members of a common block are stored in the group ‘noncommonblock’ in the HDF5 file.

The choice to store just about everything is made to maximize the ability to go

²<http://www.hdfgroup.org/>

back and study aspects of past SCEPTIC3D runs not initially intended or of interest, as well as to increase the ability to debug the code through inspecting the contents of all the common blocks using the capabilities of other software such as MATLAB. For this latter purpose the previous practice of exiting SCEPTIC3D if a problem is detected has been altered to jumping to the output stage, which allows much easier debugging of for instance errors that occur after many time-steps and are difficult to reproduce.

Though it would be convenient if the process of outputting the common block contents was automated, the present implementation requires the data set name, its rank (number of dimensions), and the size of each storage and data dimension to be passed to a custom wrapper function for the particular data type. The wrapper functions are used to simplify outputting standard Fortran arrays, since the large flexibility of HDF5 does leave it rather cumbersome to do even simple tasks. Further, the wrapper functions set the storage dimensions in the HDF5 file to be the same as the data dimensions, which avoids needlessly large output files. Thus, under the present implementation, a variable added to a common block in the code should also be added to the HDF5 output function, unless it is to intentionally be left out of the HDF5 output file.

Some very large arrays associated with the reinjection scheme are presently not output unless the `--fulloutput` option is passed to SCEPTIC3D. This is done to reduce the HDF5 file-size somewhat, since storing and moving very large files is inconveniently slow. That said, the cost of reading a dataset from an HDF5 file is mainly set by the size of the particular dataset, not the size of the file, so if storage space and transfers are not an issue the `--fulloutput` option can be used without reservation.

Several command-line tools are available that allow browsing and manipulating HDF5 files. For instance, `h5ls` allows the groups and datasets of an HDF5 file to be browsed much like folders and files on a Linux system, while `h5copy` allows groups and datasets to be copied to a different file, for instance for the purposes of storing or transferring subsets of the HDF5 file. Further, `h5dump` allows the datasets to be

inspected much as if they were in an ASCII file, but with greater flexibility and power of selection. The availability of these tools is another good argument for outputting as much data as possible, since scripts can easily be written to extract particular subsets of the data required for a specific application, leaving storage requirements as the only real argument against excessive output.

For parallel runs of SCEPTIC3D, only the master node presently outputs data, though in some cases after a reduction across all nodes of a quantity of interest. If desirable, it would be easy to enable each node to output its own HDF5 file, but an alternative approach would be to use the parallel I/O capabilities of HDF5 to write to a single output file from all the nodes. This has however not been explored at present, and would likely lead to very large storage requirements.

Many of the issues brought up with regard to the ASCII output could alternately have been resolved by switching to binary Fortran output. However, binary Fortran output is specific to a certain architecture, and lacks many of the features that make HDF5 so attractive as a storage format. For example, HDF5 captures not only the names of the variables (datasets) and their organization into common blocks (groups), but also the data type and precision in a platform-independent way. An HDF5 file generated on a 32 bit architecture can thus easily be processed on a 64 bit architecture and vice-versa. Further, the HDF5 file contains information about the storage dimensions etc. of its arrays, allowing them to be read into other programs such as MATLAB without additional external information. The capability to only read a specific part of the output file is also lacking for binary Fortran output, so ultimately it does not represent a viable alternative to the implemented HDF5 output.

The widespread support for HDF5 in mathematical and visualization software is another strength of the format. In addition to frequent analysis and plotting of SCEPTIC3D HDF5 data using MATLAB, work is also underway to use VisIt to visualize data from the HDF5 output files. This requires specifying additional information about the data in and relationship between the arrays through an XML document, as well as generating some custom coordinate arrays, but should in principle offer a means to study the 3D outputs of SCEPTIC3D with a powerful visualization software.

Chapter 4

Collisional Ion Collection by a Conducting Sphere

4.1 Perturbation by a Collecting Object

Introducing a collecting object into the model plasma described in sec. 2.1 perturbs it. For most cases, simple analytic models like those described in sec. 1.1 are not adequate, and so computational approaches like using SCEPTIC3D are required to model and understand the system.

Before delving into specific results obtained with the upgraded SCEPTIC3D, is useful to go over some of the model assumptions and approximations implicitly and explicitly made in the code. This will inform the choice of which problems to tackle with SCEPTIC3D, as well as flesh out some caveats that come with the results.

4.1.1 Collecting Object

An ideal collecting object is considered in SCEPTIC3D. It is taken to absorb any ions and electrons that strike it, while at the same time not emitting any charged particles. The object can be either insulating or conducting, and in the latter case can have either a floating or fixed potential.

For insulating or floating potential objects, a steady-state solution requires that

the electron and ion currents to the object are equal. For an insulating object this must be true locally everywhere on its surface, while for a conducting floating potential object it need only hold in an integral sense. If the ion and electron currents to the conducting object do not balance locally, there will be currents passing between points on its surface, which must be considered for instance for force calculations in the presence of a magnetic field.

In true steady state an insulating or floating potential object must emit a neutral from its surface for each ion it absorbs. However, since the number of plasma ions impacting an object typically is negligible compared to the number of atoms it comprises, a quasi-steady solution could very well involve ions being absorbed without emitting a neutral, or each ion impact ejecting more than one neutral from the surface on average.

SCEPTIC3D does not model or track neutrals being ejected from the object surface, and is thus limited to regimes where these are not important. In terms of whether charge-exchange collisions are affected this is probably not a large restriction, since the neutral density for plasmas where charge-exchange collisions are important typically is much greater than the ion density, and any emitted neutrals thus represent a negligible perturbation to the neutral density. However, in systems where the ionization mean free path is comparable to the extent of the perturbation by the object, emitted neutrals could be ionized in locations where they significantly affect the ion density and/or populate trapped or depleted orbits. In that case the emission of neutrals could affect ion collection in a way not presently captured by SCEPTIC3D.

Another consideration is the force on the object associated with emitted neutrals. This is an issue that for instance comes up in the context of the rocket-force on dust grains in tokamak edge plasmas. Presently SCEPTIC3D does not estimate this force, but since it is not something that needs to be included self-consistently in the PIC calculation, it could in principle be estimated based on the local ion currents to the object, though it may be a very problem-dependent quantity.

4.1.2 Boltzmann Relation

A key assumption in the hybrid-PIC approach used in SCEPTIC3D is that the electrons can be adequately modeled by a Boltzmann relation. This is essential in avoiding the hundred-fold increase in computational cost associated with also moving electrons in a PIC manner, but does mean that one has to be careful when applying SCEPTIC3D to problems where Boltzmann electrons may not be a good approximation.

There are several ways to derive and/or think about the Boltzmann relation: One is to consider a fluid model where momentum balance requires that a pressure gradient (or density gradient at the constant T_e assumed in SCEPTIC3D) balance the potential gradient; another is that a kinetic solution with a Maxwellian distribution of electrons at one point on a potential gradient is Maxwellian with the same temperature at every other point on that gradient, but with the electron density varying according to the Boltzmann relation:

$$n_e = n_{e\infty} \exp(e\phi/T_e), \quad (4.1)$$

where e is the electron charge, ϕ is the potential, and $n_{e\infty}$ is the electron density at the point of zero potential.

In an unperturbed system with uniform density, there could in principle be a uniform background electric field $\mathbf{E}_d = E_d \mathbf{e}_z$ driving electron and ion drifts, balanced by various drags on the two species (e.g. neutral drag). One can imagine such a situation being arranged by means of an induced electromotive force (e.g. in a tokamak), or an externally imposed uniformly varying potential (e.g. by flowing a current through a cylindrical resistor surrounding the plasma). In such a situation, it seems plausible to exclude the contribution of the uniform electric field from the potential used in the Boltzmann relation, such that the constant-density solution is recovered at infinity. If the total potential (including the contribution from \mathbf{E}_d) is ϕ' , then the modified Boltzmann relation is

$$n_e = n_{e\infty} \exp(e[\phi' + zE_d]/T_e), \quad (4.2)$$

where the total potential satisfies the boundary condition $\phi'_{\infty} = -E_d z$ at infinity. This is equivalent to regarding the force on the ions as being given by $\mathbf{F} = -e\nabla\phi + e\mathbf{E}_d$, where $\phi = \phi' + zE_d$ is the potential without the contribution from \mathbf{E}_d . One can then consider $e\mathbf{E}_d$ to be simply an external force driving the drift, while the electron density is given by the traditional Boltzmann relation in eq. 4.1; this is the approach taken to external electric fields in SCEPTIC3D (which are not restricted to be in the \mathbf{e}_z direction as in the above example).

Though the modified Boltzmann relation was conveniently defined for an unperturbed plasma, and then camouflaged by defining ϕ , it is important to consider the implicit assumptions involved in then applying that relation to a perturbed potential, as well as the impact of those assumptions on the validity of using the modified Boltzmann relation in applications to specific problems. A discussion of this issue in the context of more specific situations is presented sec. 4.1.3, and it is something that should be kept in mind when applying SCEPTIC3D to a new type of problem.

4.1.3 External Electric Field

An external electric field, whether in the absence of or perpendicular or parallel to a magnetic field, is the source of several subtleties which should be discussed, both in terms of the boundary condition for the potential on the object's surface, and the implications for the assumption of Boltzmann electrons.

A conducting object shields electric fields in a vacuum, since the potential at its surface must be constant (whether floating or fixed) in its rest frame. In the presence of a plasma the potential at the object surface must still be constant, but the shielding of the field is affected by the presence of the plasma, and must thus be solved for self-consistently. As previously mentioned the approach taken in SCEPTIC3D is to not include the external electric field in the outer boundary condition for the potential (ϕ), so rather the shielding of the external electric field must be included in the boundary condition at the object surface. Combined with adding the constant acceleration due to the external electric field to the ions this allows for a self-consistent solution of the ion motion and potential.

Insulating objects do not shield electric fields in a vacuum, but in a plasma the external electric field affects the ion motion, and thus the charging of the object surface required to locally balance the electron and ion currents. The electron currents are assumed to depend only on ϕ to be consistent with the use of a Boltzmann factor in ϕ for the density, and are calculated as described in ref. [33]. Thus, no special treatment of the inner boundary condition on the potential is required for insulating objects, but the solution is nonetheless different than in the absence of the electric field.

Perpendicular Electric Field

In the case of an external electric field perpendicular to a magnetic field, the way the external field is treated in SCEPTIC3D is equivalent to solving the problem in the frame moving at the $\mathbf{E} \times \mathbf{B}$ velocity. Transforming to the drifting frame makes the electric field vanish in the unperturbed region, and leaves the collecting object moving with velocity equal and opposite to the drift velocity.

Since the $\mathbf{E} \times \mathbf{B}$ drift speed typically is much smaller than the electron thermal speed, the electrons in the unperturbed region remain Maxwellian. Thus, in the moving frame the problem from the viewpoint of the electrons is essentially one without an electric field, i.e. only with an external magnetic field. Along each magnetic field line the arguments used to derive the Boltzmann relation still hold, so in the moving frame Boltzmann electrons is an appropriate assumption provided the appropriate boundary condition for the potential is used at the object surface.

If the object is an insulator, charge will build up on its surface until the ion and electron currents to each point on the surface are balanced. The magnetic field and motion of the object will affect ion collection, and thus lead to a varying potential on the surface of the object.

If the object is a conductor, its charges will feel a $\mathbf{v} \times \mathbf{B}$ force from the object's motion through the magnetic field in the moving frame, and a uniform electric field will arise inside the conductor to balance that force. Thus, in the moving frame the potential at the surface of the conductor is not a constant, and there is a (shielded)

dipole electric field in the vicinity of the object.

Since the potential at the surface of the conductor is not constant in the moving frame, neither is the electron density. Transforming back to the stationary frame, the situation is thus that there is a varying electron density around the equipotential conductor surface. Similarly, since the electron density near an insulating object is set based on the potential ϕ in the moving frame, the density will not correspond to a Boltzmann factor based on the total potential ϕ' in the stationary frame.

That a varying electron density at the surface of an equipotential is the right answer in the stationary frame may seem strange, but it is not an unreasonable answer. Consider for instance a conducting sphere in a strongly magnetized plasma. In that case the drift can be neglected for an external perpendicular electric field, and ion and electron motion is restricted to the magnetic field lines. At the probe surface, the potential is a constant, while at the outer surface the potential varies to give rise to the electric field. If the density in the unperturbed region is taken to be constant, then the electron density at the probe will vary since the potential drop along different magnetic field lines intersecting the surface is different.

No matter how strong the magnetic field is, a conductor should be able to shield the external electric field in steady state, since doing so only requires a static charge which can build up over a time much longer than the simulation time. In the case of a very strong magnetic field, it is possible that currents in the object could lead to the Hall effect being important in setting the charge distribution on the surface of the object. However, for realistic operating parameters and conductors this effect is probably negligible in SCEPTIC3D, though the force due to internal currents crossing a magnetic field should be considered when examining the forces on the object [3].

Parallel Electric Field

Though the modified Boltzmann relation appears to hold up well in the case of a perpendicular electric field, its validity in the case of an external electric field parallel to, or in the absence of a magnetic field, is much more questionable.

A parallel electric field cannot be transformed away, so maintaining Boltzmann

electrons in the unperturbed case requires balancing the electric force with an average drag force. To prevent distortions of the distribution function, the average drift velocity must be much smaller than the electron thermal speed, and there should not be a population of super-thermal (e.g. runaway) electrons, since they would practically ignore any potential variations and thus clearly not be Boltzmann. Further, if the distribution function is allowed to be noticeably asymmetric, the response to a left or right sloping potential perturbation will be different, which is in clear contradiction to the Boltzmann relation. The distribution function thus really does need to be quite close to Maxwellian to justify using the Boltzmann relation.

A large enough drag on the electrons to prevent significant distortions of the distribution function seems difficult to reconcile in a physical system where the ions are not highly collisional. Further, such a strong drag may imply strong coupling to another species, which may also lead to a different electron behavior than that expected from the Boltzmann relation.

Another issue is that if the object is conducting, it will shield the external field, which will probably make maintaining a balance between drag and the partially shielded external field a problem. Maintaining such a balance would require the drag to be proportional to the electric force, which seems an unlikely situation.

All this said, however, it may be that using Boltzmann electrons does not lead to large errors in many cases despite it being a bad assumption. The reason for this is that the electron density near electron-repelling objects such as those considered in SCEPTIC3D is small, so the potential is mainly affected by the ion density. Thus, it is possible that the results from SCEPTIC3D are more realistic for cases with a parallel electric field than what one might think based on the discussion in this section. One caveat to this though is that the electron current to the object is important for floating potential objects, so the Boltzmann-like assumptions presently used to calculate the electron currents in SCEPTIC3D could lead to incorrect floating potential and thus potential structure.

Boltzmann electrons is a common assumption in simulation and theory [34, 35, 21, 36, 37, 38]. However, what sets the present use of Boltzmann electrons aside

from most other applications is the possible presence of a significant electron drift due to an electric field. A Boltzmann treatment for non-Maxwellian distributions has been applied for instance by using a separate Boltzmann relation for each of two components of a bi-Maxwellian approximation to the non-Maxwellian distribution [38, 39], but neither of those components were drifting.

Since even the assumption of a uniform parallel electric field may not be a great approximation to a given physical system, results from SCEPTIC3D for problems with a parallel electric field are likely to be less quantitatively correct than those for problems where its underlying assumptions are on more solid footing. Thus, even if the Boltzmann electron assumption does affect the results noticeably in an unphysical way, its effects may not be much worse than those of the other assumptions made in SCEPTIC3D. Thus, provided the caveats listed in this section are kept in mind, SCEPTIC3D is probably adequate also for a wide range of studies of parallel drifts driven by an electric field, especially if one is mainly after qualitative changes and general trends.

4.2 Ion Collection with a Background Neutral Drift

As discussed in sec. 4.1.3, there is question as to the validity of the Boltzmann electron treatment in SCEPTIC3D for unmagnetized problems where the ion drift is driven by a background electric field. Ion drift driven by a background neutral flow on the other hand, or equivalently by motion of the object through the neutrals/plasma, should be well modeled by SCEPTIC3D. A preliminary examination of how ion collection is affected by a background drift and neutral collisions has thus been conducted with the newly upgraded SCEPTIC3D, and is the focus of this section.

SCEPTIC3D was run for a grid of charge-exchange collision frequency ν_c and background neutral drift speed v_d . A conducting floating potential object was considered, with $\lambda_{De} = 20 r_p$ and $T_i = 0.1 T_e$. These parameters were chosen to be representative of for example a dust grain in a dusty-plasma experiment, though there may be other physical systems for which these parameters are relevant.

The ion density near the object is shown in fig. 4-1 for a representative sample of the runs. The ion density is examined to shed light on how collisions and drifts affect ion collection, such as to better understand the dependence of the collected ion current on the charge-exchange collisionality and neutral drift speed, which is shown in fig. 4-2. A more detailed investigation could be carried out to investigate things like the distribution of current to the object surface etc., but has not been done for this initial application of SCEPTIC3D, which is intended mainly to showcase its new capabilities and discuss some of its limitations.

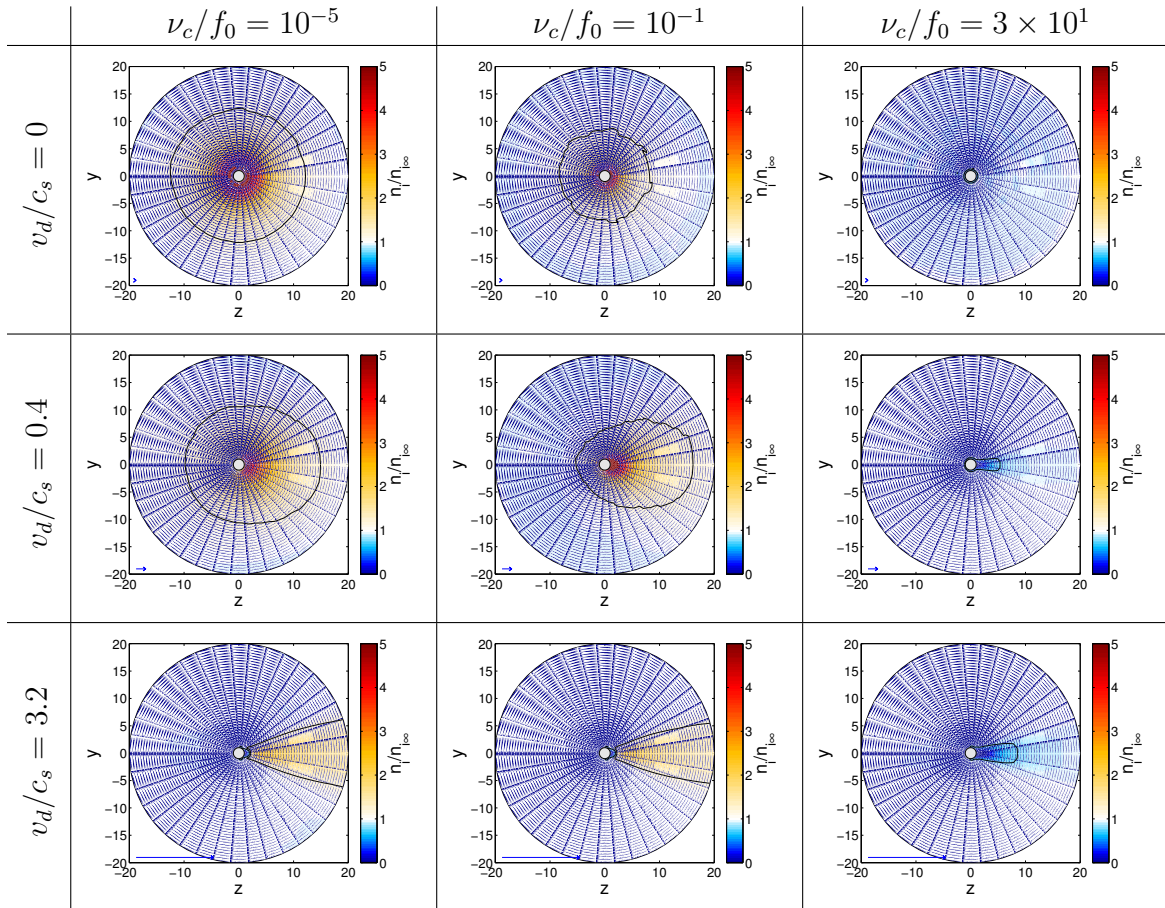


Figure 4-1: Ion density near the object for representative neutral drift speeds (v_d increasing downwards) and collisionalities (ν_c increasing to the right, with $f_0 = c_s/r_p$ being the unit of frequency in SCEPTIC3D). Contours show where the ion density n_i is enhanced or reduced by 20% compared to the unperturbed ion density $n_{i\infty}$, and a blue arrow in the lower left corner of each plot shows the direction and relative strength of the drift.

Moderate levels of charge-exchange collisionality ‘destroy’ angular momentum by

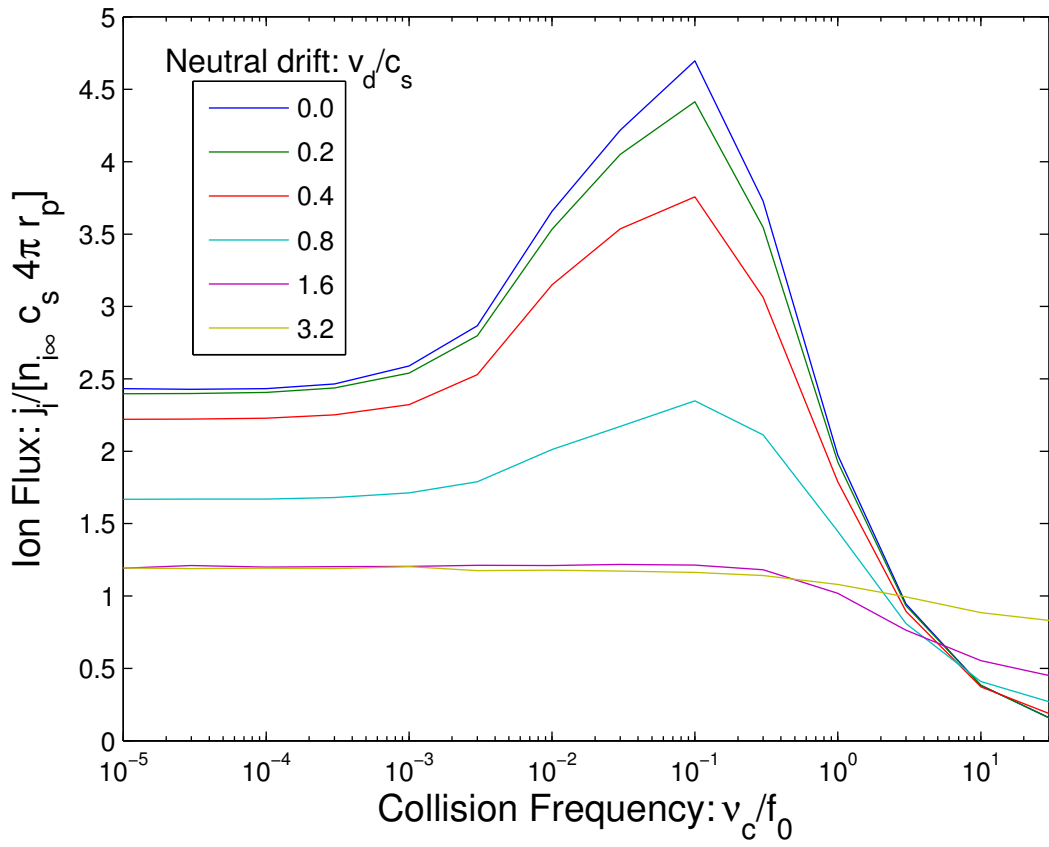


Figure 4-2: Collected ion flux against collisionality in an unmagnetized plasma, for several neutral drift speeds (the legend order matches that of the curves at their peaks). Here $f_0 = c_s/r_p$ is the unit of frequency in SCEPTIC3D, and j_i is the ion current to the sphere. Moderate collisionality is seen to enhance ion collection for sub-sonic drifts, while large collisionality reduces collection.

randomizing the ion velocities. Since angular momentum in the collisionless case prevents some ions from approaching the object, this ‘destruction’ of angular momentum acts to shrink the region of enhanced ion density near or trailing the object. This is seen when comparing the first and second columns of fig. 4-1.

Another consequence of the ‘destruction’ of angular momentum is that the ion current to the object is enhanced for moderate charge-exchange collisionalities, as is seen in fig. 4-2. This is only true for sub-sonic drifts, since most of the ions collected by an object sweeping through the plasma at supersonic speeds are relatively unperturbed before being absorbed, and therefore are largely unaffected by charge-exchange collisions. Thus, as is seen in fig. 4-2, the enhancement of ion collection at moderate collisionalities seen for the stationary case is weakened as the drift speed increases from the ion thermal speed to the ion sound speed, above which no enhancement is seen.

As charge-exchange collisionality is increased beyond the level where it gives rise to a large ion current enhancement by ‘destroying’ angular momentum, it also starts ‘destroying’ radial momentum. This introduces an effective drag on the ions, which in turn reduces ion collection, causing the turnover and subsequent decrease of the collected current with collisionality seen in fig. 4-2.

At high levels of charge-exchange collisionality the ions become tightly coupled to the neutrals, and the moving object ends up sweeping out a region depleted of ions both at super- and sub-sonic drift speeds, as is seen in the last column of fig. 4-1. The sound speed is no longer important here since the ions are tightly coupled to the neutrals, which are taken to be unaffected by the motion of the object. Ignoring any perturbation of the neutrals by the object may not be a good approximation in the large-collisionality limit, but the PIC code SCEPTIC3D isn’t really designed to treat this more Monte-Carlo relevant regime anyways, so a breakdown of the assumptions there is not of great concern.

The dependence of ion collection on charge-exchange collisionality has previously been studied for the stationary case [26] using SCEPTIC, and comparison of stationary runs of SCEPTIC3D with the equivalent runs of SCEPTIC reveals agreement to

better than 1%, providing a good benchmark for the collision treatment in SCEPTIC3D. In principle SCEPTIC3D and SCEPTIC could also be compared for runs with neutral drift, but this has not been done at present since the implementation of neutral drifts in SCEPTIC was only recently completed (see sec. 2.3.2).

4.3 Ion Collection with a Background Magnetic Field

Charge-exchange collisions enable transport of ions across magnetic field lines, offering a means to repopulate the magnetic shadow associated with collecting objects in a magnetic field. A preliminary examination of how ion collection is affected by a background magnetic field and charge-exchange collisions has thus been conducted with the newly upgraded SCEPTIC3D, and is the focus of this section.

SCEPTIC3D was run for a grid of charge-exchange collision frequency ν_c and background magnetic field strength B . A conducting floating potential object was considered, with $\lambda_{De} = 20 r_p$ and $T_i = 0.1 T_e$. These parameters were chosen to be representative of for example a dust grain in a dusty-plasma experiment, though there may be other physical systems for which these parameters are relevant.

The ion density near the object is shown in fig. 4-3 for a representative sample of the runs. The ion density is examined to shed light on how collisions and a magnetic field affect ion collection, such as to better understand the dependence of the collected ion current on the charge-exchange collisionality and magnetic field strength, which is shown in fig. 4-4.

In the unmagnetized collisionless case, angular momentum conservation limits the ion current to the object. Adding a magnetic field restricts the perpendicular ion motion, resulting in increased collection from regions along the field from the object, and decreased collections from elsewhere. The result is a magnetic shadow of depleted ion density extending from the object in the direction of the magnetic field. This is seen in the first column of fig. 4-3, where the collisionality is low enough for the runs

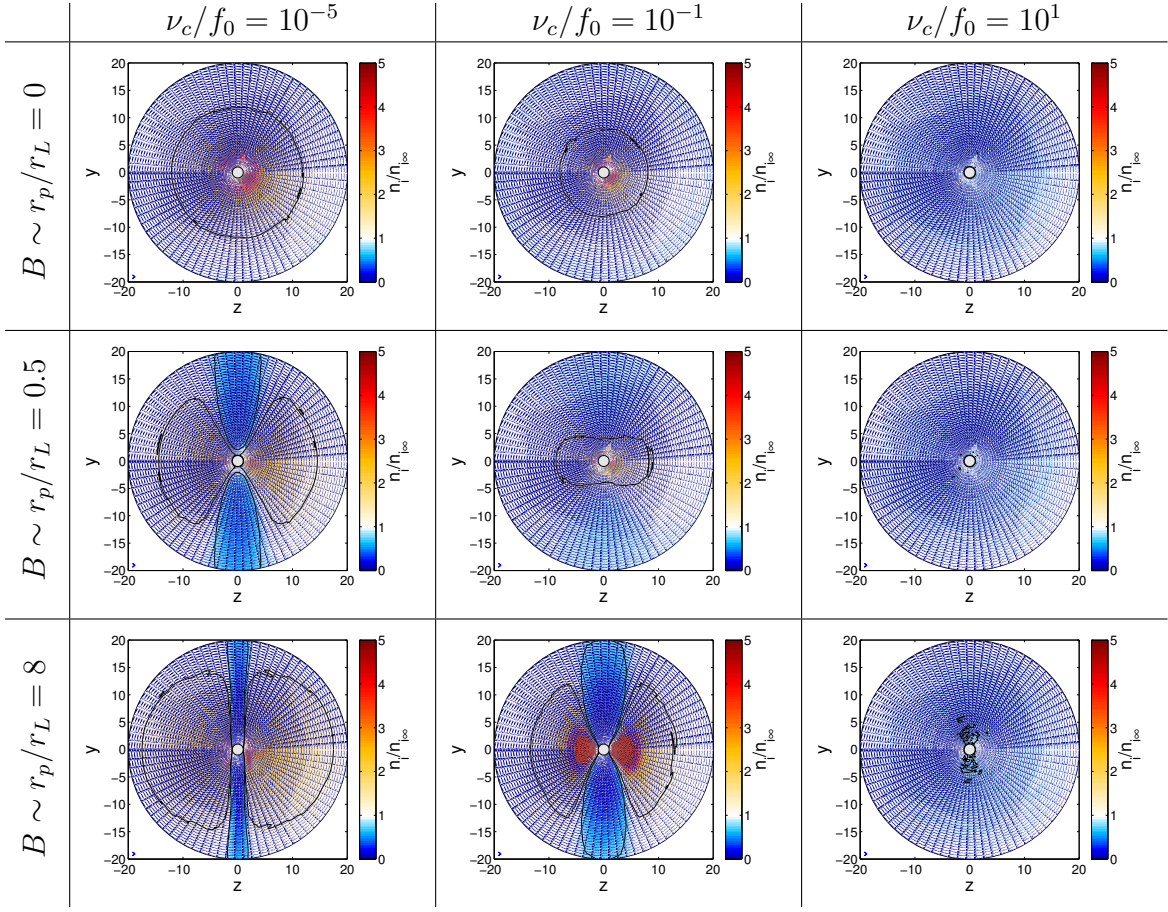


Figure 4-3: Ion density near the object for representative magnetizations (B increasing downwards, corresponding to $f_{ci}/f_0 = 0$, 0.2, and 3.2, respectively, and with r_L being the ion Larmor radius) and collisionalities (ν_c increasing to the right, with $f_0 = c_s/r_p$ being the unit of frequency in SCEPTIC3D). Contours show where the ion density n_i is enhanced or reduced by 20% compared to the unperturbed ion density $n_{i\infty}$. The magnetic field is in the \mathbf{e}_y direction, and there is no background ion or neutral drift.

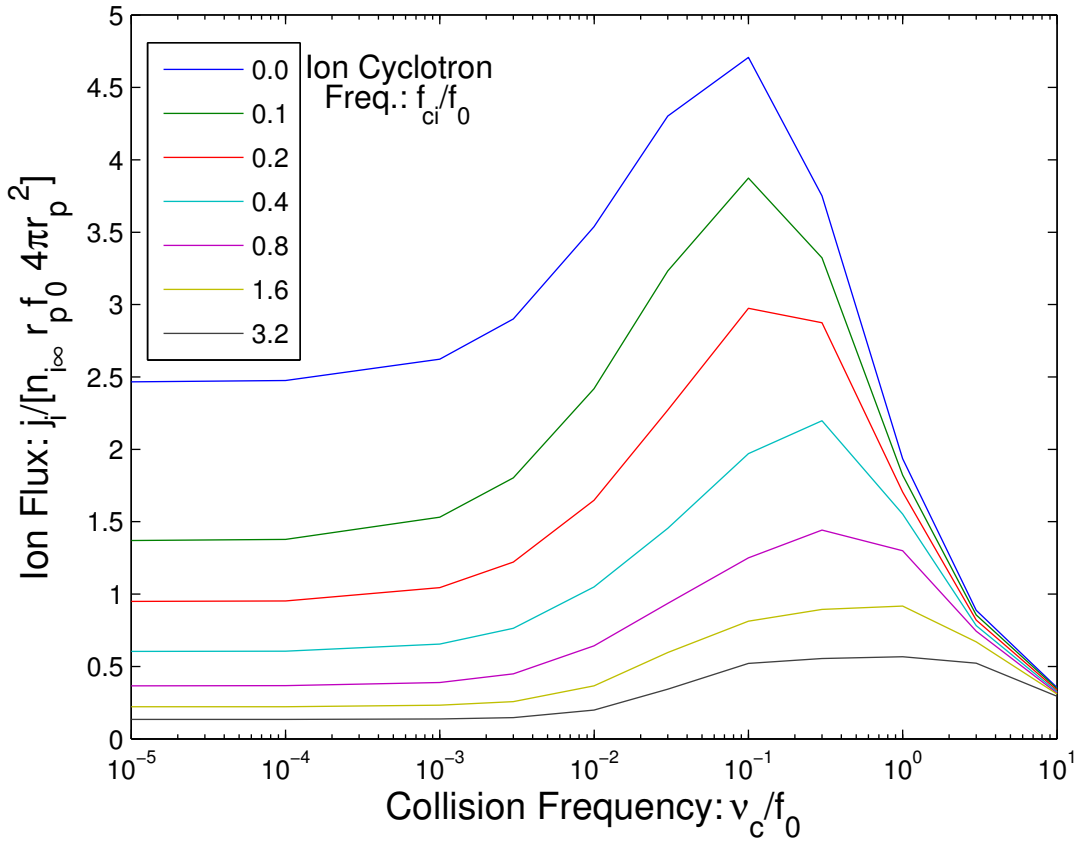


Figure 4-4: Collected ion flux against collisionality, for several magnetic field strengths (the legend order matches that of the curves at their peaks). Here $f_0 = c_s/r_p$ is the unit of frequency in SCEPTIC3D, and j_i is the ion current to the sphere. Moderate collisionality is seen to enhance ion collection for all magnetic field strengths considered.

to be effectively collisionless.

For the magnetic shadow to be finite in extent, there must be a mechanism by which the depleted regions are repopulated, which requires cross-field transport. Charge-exchange collisions can produce such transport, since the new velocities drawn randomly from the neutral distribution have no memory of the gyro-motion of the ion being replaced. This is seen when comparing columns one and two of fig. 4-3, where charge-exchange collisions are seen to gradually diffuse and repopulate the magnetic shadow. Column three shows that for $\nu_c \gg f_{ci}$ (the ion cyclotron frequency) the gyro-motion is disrupted, rendering the magnetic field unimportant.

Though the mechanism is different for the unmagnetized and highly magnetized cases, moderate charge-exchange collisionality is seen in fig. 4-4 to enhance the collected ion current for all magnetizations considered. In fact, the ratio of the maximum current to the collisionless current increases from ~ 2 for the unmagnetized case to ~ 4 for the strongly magnetized case. However, there are caveats to this observation, as elaborated upon below.

The SCEPTIC3D domain is spherical, while the magnetic shadow for strongly magnetized cases is essentially a rod extending from the object. This causes some difficulty, as the boundary conditions and re-injection scheme are not designed to have the perturbation due to the object extend to the boundary. In the stationary collisionless case there is no mechanism for repopulating the magnetic shadow, so it extending to the boundary is inevitable. Even for moderate magnetizations at low collisionalities the required size of the computational domain becomes very large, and this is difficult to handle since the volume of plasma tracked scales with the cube of the radius of the outer boundary, while the surface area of (and thus current collected by) the object stays unchanged.

The results for cases where the magnetic shadow extends to the outer boundary should be treated with caution: Since particles are injected at that intersection as if the plasma was unperturbed, a larger flux of ions is likely injected into the magnetic shadow than is realistic. This may lead to an incorrect ion current to, and thus floating potential of, the object, and thus also an incorrect potential profile near the

object.

Chapter 5

Discussion and Conclusions

5.1 New Capabilities of SCEPTIC3D

Several new capabilities have been added to SCEPTIC3D:

- Charge-exchange collisions are now included, allowing one to specify the charge-exchange collision frequency through the `-k` option.
- The magnitude of a background neutral drift can be set with the `-vn` option, and its direction specified through the `-cnd` ($\cos(\theta_{vn})$) and `-psind` (ψ_{vn}) inputs.
- The `-v` and `-cd` options now specify the electric field driven drift relative to the neutral drift for non-zero collision frequency, but the actual ion drift may be more complicated (see sec. 2.1.4).
- A new Monte Carlo reinjection scheme has been added to handle reinjection for the more complicated distribution functions that arise in the presence of charge-exchange collisions, neutral drifts, and parallel electric fields. It can in principle handle any statistically represented distribution function, and thus enables future studies of the sensitivity of the solution to the injected distribution, as well as benchmarking against analytic models that inject a simplified ion distribution.

- The three 1D distribution functions in each Cartesian coordinate can now be stored on a 3D grid, allowing detailed examination of the ion distribution function, and enabling future code–experiment comparisons with (e.g.) the VINETA experiment.
- The Poisson solver has been modified to make it more robust, enabling stable runs for grids and parameters that were previously inaccessible.
- A `--nonlin` option has been added, which leads SCEPTIC3D to solve the full Poisson equation at each time-step, rather than linearizing the electron response around the potential at the previous time-step.
- A new HDF5 output system has been added to allow binary output of large data-structures, easing post-processing and analysis, as well as debugging of certain parts of the code.

A version of SCEPTIC3D including some of these improvements is currently available for download¹, and a version including all these upgrades will be made available in the future.

5.2 Collisional Ion Collection

The upgraded SCEPTIC3D has been applied to the problem of collisional ion collection by a conducting sphere in a drifting or magnetized plasma. The preliminary results presented in chap. 4 showcase the new capabilities of SCEPTIC3D, and provide a starting point for a more detailed analysis to be conducted in the future. A discussion of the applicability of SCEPTIC3D to various problems is also given in that chapter, and the following are the main points of that discussion and the presented results:

- The assumption of Boltzmann electrons made in SCEPTIC3D is expected to be adequate for problems with neutral drifts, magnetic fields, and perpendicular

¹<http://silas.psfc.mit.edu/sceptic/>

electric fields, but may be a less good approximation for problems with an electric field not perpendicular to a magnetic field.

- The enhancement of the collected current at moderate collisionalities in the stationary plasma case is also seen for sub-sonic neutral drift speeds ($< c_s$), though it weakens with increasing drift speed and is not present for super-sonic speeds.
- For low to moderate collisionalities the ion density near the object and in its wake are enhanced, since angular momentum prevents collection of many ions orbiting near the object, and ion focusing into the wake enhances the density there.
- For high collisionalities the object sweeps out a region of depleted ion density, since the tight coupling to the neutrals prevents ions from immediately repopulating the region behind the object.
- When considering a magnetic field rather than a neutral drift, the relative enhancement of ion collection at moderate collisionalities is seen to increase with magnetic field strength. The results for low collisionalities may not be quantitatively correct because the magnetic shadow extended to the domain edge, but the general observation about the collisional enhancement is expected to hold.
- Charge-exchange collisions repopulate the magnetic shadow of the object by providing cross-field transport, thereby increasing ion collection. In the limit of high collisionality the gyro-motion is disrupted, so the magnetic field becomes unimportant.

5.3 Future Work

A number of things could be investigated in the future:

- The difference in charging of conducting and insulating spheres in a magnetized plasma is something that may shortly be examined experimentally by a group

in Kiel, and might therefore be interesting to investigate with SCEPTIC3D.

- It would be useful to expand the preliminary results presented in this thesis on drifting or magnetizing plasmas, to develop a more thorough understanding of how charge-exchange collisions affect ion collection in those settings.
- More complicated scenarios that take advantage of the full 3D capabilities of SCEPTIC3D with charge-exchange collisions should be pursued.
- The sensitivity of the solution and ion collection to the injected ion distribution could be examined, both to investigate the impact of the simplifying assumptions made for the unperturbed plasma, as well as the sensitivity of probes and dust grain charging to the background ion distribution.

Bibliography

- [1] Leonardo Patacchini and Ian H Hutchinson. Spherical probes at ion saturation in E x B fields. *Plasma Physics and Controlled Fusion*, 52(3):035005, March 2010.
- [2] Leonardo Patacchini and Ian H Hutchinson. Spherical conducting probes in finite Debye length plasmas and E x B fields. *Plasma Physics and Controlled Fusion*, 53(2):025005, February 2011.
- [3] Leonardo Patacchini and Ian H Hutchinson. Forces on a spherical conducting particle in E x B fields. *Plasma Physics and Controlled Fusion*, 53(6):065023, June 2011.
- [4] H M Mott-Smith and I Langmuir. The Theory of Collectors in Gaseous Discharges. *Phys. Rev.*, 28:727–763, 1926.
- [5] J E Allen, R L F Boyd, and P Reynolds. The Collection of Positive Ions by a Probe Immersed in a Plasma. *Proceedings of the Physical Society. Section B*, 70(3):297–304, March 1957.
- [6] J E Allen. Probe theory - the orbital motion approach. *Physica Scripta*, 45(5):497–503, May 1992.
- [7] L Patacchini. Collisionless Ion Collection by a Sphere in a Weakly Magnetized Plasma. Master's thesis, Massachusetts Institute of Technology, Nuclear Science and Engineering Department, May 2007.
- [8] D. Bohm, E H S Burhop, and H S W Massey. No Title. In A Guthrie and R K Wakerling, editors, *The Characteristics of Electrical Discharges in Magnetic Fields*, chapter 2. McGraw-Hill Co., New York, 1949.
- [9] Lewi Tonks and Irving Langmuir. A General Theory of the Plasma of an Arc. *Physical Review*, 34(6):876 LP – 922, September 1929.
- [10] H Thomas, G E Morfill, V Demmel, J Goree, B Feuerbacher, and D Mohlmann. Plasma Crystal: Coulomb Crystallization in a Dusty Plasma. *Physical Review Letters*, 73(5):652 LP – 655, August 1994.

- [11] A. Yu. Pigarov, S. I. Krasheninnikov, T. K. Soboleva, and T. D. Rognlien. Dust-particle transport in tokamak edge plasmas. *Physics of Plasmas*, 12(12):122508, December 2005.
- [12] P. K. Shukla. A survey of dusty plasma physics. *Physics of Plasmas*, 8(5):1791, 2001.
- [13] Christian M. Franck, Olaf Grulke, and Thomas Klinger. Transition from unbounded to bounded plasma whistler wave dispersion. *Physics of Plasmas*, 9(8):3254, July 2002.
- [14] J. S. Halekas, V. Angelopoulos, D. G. Sibeck, K. K. Khurana, C. T. Russell, G. T. Delory, W. M. Farrell, J. P. McFadden, J. W. Bonnell, D. Larson, R. E. Ergun, F. Plaschke, and K. H. Glassmeier. First Results from ARTEMIS, a New Two-Spacecraft Lunar Mission: Counter-Streaming Plasma Populations in the Lunar Wake. *Space Science Reviews*, pages 1–15–15, January 2011.
- [15] S. Wiehle, F. Plaschke, U. Motschmann, K.-H. Glassmeier, H.U. Auster, V. Angelopoulos, J. Mueller, H. Kriegel, E. Georgescu, J. Halekas, D.G. Sibeck, and J.P. McFadden. First lunar wake passage of ARTEMIS: Discrimination of wake effects and solar wind fluctuations by 3D hybrid simulations. *Planetary and Space Science*, 59(8):661–671, June 2011.
- [16] I H Hutchinson. Ion collection by a sphere in a flowing plasma: I. Quasineutral. *Plasma Physics and Controlled Fusion*, 44(9):1953–1977, September 2002.
- [17] I H Hutchinson. Ion collection by a sphere in a flowing plasma: 2. non-zero Debye length. *Plasma Physics and Controlled Fusion*, 45(8):1477–1500, August 2003.
- [18] I H Hutchinson. Ion collection by a sphere in a flowing plasma: 3. Floating potential and drag force. *Plasma Physics and Controlled Fusion*, 47(1):71–87, January 2005.
- [19] L Patacchini. *Collisionless ion collection by non-emitting spherical bodies in ExB fields*. Thesis (ph. d.), Massachusetts Institute of Technology, Cambridge, 2010.
- [20] C K Birdsall and A B Langdon. *Plasma Physics Via Computer Simulation*. Taylor & Francis, Institute of Physics, Series in Plasma Physics, NY, 1985.
- [21] Roger W. Hockney and James W. Eastwood. *Computer simulation using particles*. Institute of Physics, 1992.
- [22] J P Verboncoeur. Particle simulation of plasmas: review and advances. *Plasma Physics and Controlled Fusion*, 47(5A):A231–A260, May 2005.
- [23] A. V. Phelps. The application of scattering cross sections to ion flux models in discharge sheaths. *Journal of Applied Physics*, 76(2):747, 1994.

- [24] S. A. Maiorov. Ion drift in a gas in an external electric field. *Plasma Physics Reports*, 35(9):802–812, October 2009.
- [25] S. A. Maiorov. Calculation of resonant charge exchange cross-sections of ions Rubidium, Cesium, Mercury and noble gases. In *34th EPS Conference on Plasma Phys., ECA Vol. 31*, pages P–2.115, Warsaw, 2007.
- [26] I H Hutchinson and L Patacchini. Computation of the effect of neutral collisions on ion current to a floating sphere in a stationary plasma. *Physics of Plasmas*, 14(1):013505, 2007.
- [27] Leonardo Patacchini and Ian Hutchinson. Fully Self-Consistent Ion-Drag-Force Calculations for Dust in Collisional Plasmas with an External Electric Field. *Physical Review Letters*, 101(2):1–4, July 2008.
- [28] Martin Lampe, Valeriy Gavrishchaka, Gurudas Ganguli, and Glenn Joyce. Effect of Trapped Ions on Shielding of a Charged Spherical Object in a Plasma. *Physical Review Letters*, 86(23):5278 LP – 5281, June 2001.
- [29] Martin Lampe, Rajiv Goswami, Zoltan Sternovsky, Scott Robertson, Valeriy Gavrishchaka, Gurudas Ganguli, and Glenn Joyce. Trapped ion effect on shielding, current flow, and charging of a small object in a plasma. *Physics of Plasmas*, 10(5):1500, April 2003.
- [30] Z. Sternovsky, M. Lampe, and S. Robertson. Orbiting Ions in the Debye Shielding Cloud Around Dust Particles in Weakly Collisional Plasmas. *IEEE Transactions on Plasma Science*, 32(2):632–636, April 2004.
- [31] Hansjorg Fahr and Karl Gerhard Muller. Ionenbewegung unter dem Einfluss von Umladungsstossen. *Zeitschrift fur Physik*, 200(4):343–365, August 1967.
- [32] W H Press, S A Teukolsky, W T Vetterling, and B P Flannery. *Numerical Recipes (3rd edition)*. Cambridge University Press, NY, 2007.
- [33] L. Patacchini, I H Hutchinson, and G. Lapenta. Electron collection by a negatively charged sphere in a collisionless magnetoplasma. *Physics of Plasmas*, 14(6):062111, 2007.
- [34] Francis F. Chen. *Introduction to Plasma Physics and Controlled Fusion: Plasma physics*. Springer, 1984.
- [35] G. A. Emmert and M. A. Henry. Numerical simulation of plasma sheath expansion, with applications to plasma-source ion implantation. *Journal of Applied Physics*, 71(1):113, 1992.
- [36] Ian H. Hutchinson. *Principles of plasma diagnostics*. Cambridge University Press, 2002.

- [37] Michael A. Lieberman and Allan J. Lichtenberg. *Principles of plasma discharges and materials processing*. John Wiley and Sons, 2005.
- [38] D Kwok. A hybrid Boltzmann electrons and PIC ions model for simulating transient state of partially ionized plasma. *Journal of Computational Physics*, 227(11):5758–5777, May 2008.
- [39] V.A. Godyak, V.P. Meylisis, and H.R. Strauss. Tonks-Langmuir problem for a bi-Maxwellian plasma. *IEEE Transactions on Plasma Science*, 23(4):728–734, 1995.